Achieving a large density of hydroxyl radicals for cold collisions

by

Hao Wu

B.A., Harbin Institute of Technology, 2009

M.S., Harbin Institute of Technology, 2011

A thesis submitted to the

Faculty of the Graduate School of the

University of Colorado in partial fulfillment

of the requirements for the degree of

Doctor of Philosophy

Department of Physics

2019

This thesis entitled:
Achieving a large density of hydroxyl radicals for cold collisions
written by Hao Wu
has been approved for the Department of Physics

_____

Prof. Jun Ye

_____

Prof. Carl Lineberger

Date _____

The final copy of this thesis has been examined by the signatories, and we find that both the content and the form meet acceptable presentation standards of scholarly work in the above mentioned discipline.

Wu, Hao (Ph.D., Physics)

Achieving a large density of hydroxyl radicals for cold collisions

Thesis directed by Prof. Jun Ye

Molecular physics has experienced groundbreaking progress in the fields of precision spectroscopy, chemical reaction kinetics, quantum state engineering and many-body physics. In order to better observe these phenomena, there is an insatiable pursuit of larger trapped molecular densities and longer lifetime. In this thesis, several key milestones that we have recently achieved towards these goals for hydroxyl radicals (OH) are reported. First, we discovered an enhanced spin-flip behavior of dipolar molecules due to the existence of dual (electric and magnetic) dipole moments and obtained a better understanding of complex spin-dynamics for both Hund's case (a) and (b) molecules in mixed electric and magnetic fields. Second, we demonstrated that the skimmer cooling technique can be applied to radicals and the production of OH can be enhanced by factor of 30 due to both clogging mitigation and more favorable skimmer-valve distance. Finally, we showed some preliminary results that it is possible to use a newly built Stark decelerator to study electric field controlled sub-kelvin collisions in an intra-beam.

Dedication

To Chenchen.

Acknowledgements

First and foremost, I want to thank my advisor Prof. Jun Ye, for accepting me into his group. His guidance throughout this journey, not only helped me in all the time of research, but also brought me a new perspective of how to solve problems like a physicist. The generous financial support, all kinds of resources and continuous encouragement he provided are essential to help me to search for new physics.

At my early age of joining in OH experiment, I have greatly benefited from both Dr. Matthew Hummon and Dr. Benjamin Stuhl, who lead me to the world of polar molecules and taught me experimental skills. Especially, I want to thank my great lab partner, David Reens, who has worked with me for the past seven years. Dave is an excellent physicist with engineering proficiency. The stimulating discussions with him always bring me new ideas and better understanding of physics. During my graduate career, Dr. Tim Langen and Dr. Piotr Wcislo join in our project as postdocs and I appreciate them for introducing me to different fields of physics. Thanks undergraduates who are involved in our project, Noppadol Punsuebsay and Anna McAuliffe for their hard work to help building the 3rd-generation stark decelerator. Recently, we have a new graduate student Alexander Aeppli. I am sure he will lead the OH experiment to a new level. Moreover, my thanks also go out to Dr. Mark Yeo, Dr. Alejandra Collopy, Yewei Wu, Dr. Shiqian Ding and Dr. Ian Finneran for their feedback and sharing laser techniques.

I also genuinely appreciate the illuminating discussions with Dr. Yuval Shagam, Dr. Thinh Bui, Dr. Yomay Shyur and Dr. Travis Briles. The ideas sparkled during discussions expanded my horizon and stimulated more interesting thoughts. It is also my honor to collaborate with

many brilliant theorists. Thanks Prof. Timur Tscherbul and Dr. Goulven Quéméner for their calculations, which helped to promote the progress of the experiment.

The progress of our experiment would not have been possible without the support from JILA technical staff. I want to thank Terry Brown for his support on electronics and high voltages. I would like to express my gratitude to Hans Green, Todd Asnicar from the machine shop for their generosity to teach me machining skills as well as their kindness of expediting our requested jobs.

Beyond JILA, I want to thank my friends in Boulder– Chunfeng Xu and Yuanqi Cao, who treat me as a younger brother. Next, I want to thank my parents and parents in-law for showing faith in me and giving all the support to allow me to focus on my graduate school career. Last, but not the least, I want to thank my lovely wife Chenchen for her love, caring and always being there with me. The trips we took together, the laughter we shared in daily life, the time we spent together in study room at late nights helped me go through the ups and downs along this journey.

Contents

Chapter

1 Introduction **1**

1.1 Why Polar Molecules? 1

1.1.1 Discovery of the Natural Properties of Particles 1

1.1.2 Quantum Engineering 3

1.2 Different Methods of Molecular Cooling 3

1.2.1 Direct Cooling Methods 4

1.2.2 Indirect Cooling Methods 5

2 Hydroxyl Radical Spectroscopy in a Magnetic Trap **6**

2.1 Hund's Cases 6

2.1.1 Case (a) 7

2.1.2 Case (b) 7

2.2 Zeeman Shift of OH States 9

2.2.1 Zeeman Shift of OH Ground State $X^2\Pi_{3/2}, f$ 9

2.2.2 Zeeman shift of Intermediate Case 10

2.2.3 How Does the Modified g_J Affect Our Previous Results? 11

2.2.4 Zeeman Shift of OH Excited States 12

2.3 Optical Depletion Spectroscopy in a Magnetic Trap 14

2.3.1 Experimental Sequence 14

2.3.2 Results and Analysis 16
2.4 Conclusion 19

3 Spin-flip Loss for Doubly Dipolar Molecules **20**
3.1 Hund's Case (a) Molecules 20
3.1.1 OH Stark-Zeeman Energy Structure 21
3.1.2 Enhanced Spin-flip Loss in a Magnetic Trap 21
3.2 Hund's Case (b) Molecules 27
3.2.1 YO Stark Shift and Zeeman Shift 27
3.2.2 YO Stark-Zeeman Shift and Spin-flip Loss 31
3.2.3 Properties of the Magic State 32

4 OH Density Calibration of Free Flight by H_2 Raman scattering **40**
4.1 Motivation 40
4.2 Derivation of Formulas for OH Density Calibration Calculation 41
4.2.1 A Theoretical Model for OH LIF 41
4.2.2 A Theoretical Model for H_2 Raman Scattering 42
4.3 Schematic of Experimental Setup 43
4.4 LIF Measurement of OH 46
4.4.1 Relation between Laser Energy and OH LIF 46
4.4.2 Uniformity of OH Density within the Detection Region 46
4.4.3 Homogeneity of OH within the Detection Volume 49
4.4.4 Pulse Duration and Linewidth of 282 nm laser 53
4.4.5 Translation of OH during Photon Collection 53
4.4.6 Experiment and Simulation of the Rate Equation 56
4.5 Raman Scattering with H_2 59
4.5.1 Angular Dependence of Differential Cross Section of H_2 Raman scattering . 59
4.5.2 Raman Scattering Measurement 61

4.6 Final Calibrated OH Density at the Decelerator Exit . . . 61
4.7 Density Calibration along the Stark Decelerator . . . 61

5 Enhancing Radical Molecular Beams by Skimmer Cooling 64

5.1 Motivation . . . 64
5.2 Characterization of Even-Lavie Valve . . . 65
5.2.1 Pre-experimental Test of Even-Lavie Valve . . . 65
5.2.2 A Comparison between Even-Lavie Valve and PZT Valve . . . 66
5.2.3 Repair of Even-Lavie Valve . . . 68
5.3 Experimental Apparatus of Skimmer Cooling . . . 71
5.4 Characterization of the Cryogenic Skimmer . . . 72
5.4.1 Neon . . . 72
5.4.2 Metastable Neon . . . 74
5.4.3 Shockwave and Diffusive Clogging . . . 76
5.4.4 OH Density . . . 81
5.5 A Cryogenic Hexapole . . . 82
5.6 Outlook . . . 84

6 A Third-generation Stark Decelerator 85

6.1 Motivation . . . 85
6.1.1 Degradation of Electrodes of the Second-generation Decelerator . . . 85
6.1.2 Surface Flashover of Macor . . . 86
6.1.3 Aiming for a Larger Slowing Signal . . . 89
6.2 Design and Construction of a Third-generation Stark Decelerator . . . 89
6.2.1 General Information . . . 89
6.2.2 Different Methods of Polishing . . . 90
6.2.3 Insulator . . . 91
6.2.4 Gas Conditioning . . . 91

6.3 Characterization of the Stark Decelerator 94
6.3.1 A New Mode of DC Guiding 94
6.3.2 The OH ToF of an Optimized Stark Decelerator 96

7 Cold Collisions between OH and Neon in an Intra-Beam 98

7.1 Motivation 98
7.2 Experimental Setup 100
7.3 Experimental Results and Analysis 105
7.3.1 Thermal Energy and Collisional Energy between OH and Ne 105
7.3.2 Collisional Energy between OH and Neon 108
7.3.3 Electric Field Dependent Loss Rate 109
7.4 Puzzles and Outlook 111

Bibliography 114

Tables

Table

3.1 Spin-flip loss rates (γ) of OH with different applied fields. 25

3.2 A comparison of effective trap gradient between YO and Rb. 36

4.1 Quantities involved in OH LIF 56

4.2 Quantities involved in Raman scattering 61

4.3 OH density along the decelerator 63

5.1 A comparison between Even-Lavie valve and PZT valve 68

6.1 The prebreakdown current of different gas conditioning at $\pm$ 15 kV 93

7.1 The Summary of OH and Neon speed. 109

Figures

Figure

2.1 Coupling diagram for Hund's case (a) molecules. The orbital angular momentum L is coupled to the internuclear axis by Coulombic interaction with a projected quantum number Λ. The spin of electron S is also projected onto the internuclear axis by spin-orbit coupling with a quantum number Σ. Σ and λ couple together and form Ω, which is the projection of total angular momentum J=R+Ω. 8

2.2 Coupling diagram for Hund's case (b) molecules. Due to the a stronger spin-rotation coupling, spin of electron (S) is coupled to the vector N=R+L to form total angular momentum J. 8

2.3 The excited states used for optical depletion spectroscopy. (a) Optical transition diagram. Both Q21 and Q1 can be used for optical depletion. (b) The Zeeman shift of excited state ($A^2\Sigma, \nu = 0, N = 1$). 13

2.4 Experimental sequence. The main experiment sequence is same as shown in Ref. [49]. The only difference is that we replace RF spectroscopy with an optical depletion spectroscopy. 15

2.5 The differential Zeeman shift between $^2\Pi_{3/2}, m_J = 3/2$ and $^2\Sigma, J = 3/2$. The blue line corresponds to π transition—from $^2\pi_{3/2}, m_J = 3/2$ to $^2\Sigma, J = 3/2, m_J = 3/2$. The red line corresponds to σ^- transition—from $^2\pi_{3/2}, m_J = 3/2$ to $^2\Sigma, J = 3/2, m_J = 1/2$. 16

2.6 Optical depletion spectroscopy of Q1 transition. The solid line is the best fit curve with a sum of two Boltzmann distribution from π and σ^- transitions. The fit temperature is 59 ± 4 mK. The dash line represents the distribution from σ^- transition. The dot line represents the distribution from π transition. The area underneath the Boltzmann curve is proportional to the depletion population. The starting point of the fit Boltzmann distribution labeled with an arrow corresponds to the transition line of Q1, which is 973.5624 ± 0.0001 THz. 18

2.7 The differential Zeeman shift between $^2\Pi_{3/2}, m_J = 3/2$ and $^2\Sigma, J = 1/2, m_J = 1/2$. 18

2.8 Optical depletion spectroscopy of Q21 transition. The circles are experimental data. The solid line is the best fit curve. The fit temperature is 60 ± 4 mK. The frequency of Q21 transition is labeled by an arrow corresponding to 973.5532 ± 0.0001 THz. . 19

3.1 (a) A slice of magnetic field contour of the 3D quadrupole magnetic trap. The trap is formed by a pair of ring magnets. The magnetic field is represented by black arrows. A nearly uniform electric field (3 kV/cm) is generated by applying different polarities of voltages on the front and rear magnets, which are represented by the black rectangles. The electric field is represented by red arrows. (b) The Stark-Zeeman energy of OH's doubly stretched states of $X^2\Pi_{3/2}$ as $\vec{E} \parallel \vec{B}$. The state we are interested in is colored blue. (c) The Stark-Zeeman energy of OH's doubly stretched states of $X^2\Pi_{3/2}$ as $\vec{E} \perp \vec{B}$. 22

3.2 (a) A cartoon to describe the orientation of low-field-seeking state of OH with respect to magnetic field. The dumbbell structure respresents OH molecule. If the red ball side of molecule (angular momentum orientation) points to a similar direction of magnetic field, it means that OH is in low-field-seeking state. (b) The orientation of OH inside a magnetic trap as molecule travels along Z-axis without electric field applied. If the Larmor frequency is large enough, OH can adiabatically follow the variation of magnetic field colored by purple and remain in low-field-seeking state. The magnets are grounded to avoid any stray electric field. (c) The orientation of OH inside a magnetic trap as molecule travels along Z-axis with (3 kV/cm) electric field applied. According to Hund's case (x), OH will precess along the new combined quantization axis ($d\vec{E} + \mu\vec{B}$). Once OH crosses the Z=0 mm plane, the combined quantization axis which is colored by green and the magnetic field start to point to opposite directions. Thus, OH swaps to a high-field-seeking state relative to the magnetic field and gets lost from the trap. (d) The orientation of OH inside a magnetic trap as molecule travels along X-axis with (3 kV/cm) electric field applied. The combined quantization axis varies in a similar manner as magnetic field does, which keeps OH in low-field-seeking state relative to magnetic field. The purple arrow represents the magnetic field (b-d). The black dash-dot line represents OH propagating direction (b-d). The green arrow represents the combined quantization axis (c-d). 24

3.3 A comparison between experiment and simulation on electric-field-enhanced spin-flip loss. The circular dots represent experimental data. The solid line is from Monte Carlo simulation with only one free parameter for amplitude scaling. The grey color means there is no electric field applied. The red color means 3 kV/cm electric field is applied at 50 ms after loading. The reasonably good fit suggests most of the electric-field-enhanced loss can be explained by the spin-flip loss. However, we do notice that the experimental decays are in general slower than the spin-flip loss predictions at the beginning, which suggests some two-body effects left. 26

3.4 The Zeeman shift of $X^2\Sigma$, $G = 1$, $N = 1$ states of YO. Zero energy corresponds to the relevant $N = 1$ energy which is higher than the absolute ground state by $2B$, where B is the rotational constant. There is no electric field applied. 29

3.5 The Stark shift of $X^2\Sigma$, $G = 1$, $N = 1$ states of YO. Zero energy corresponds to the relevant $N = 1$ energy which is higher than the absolute ground state by $2 \cdot B$, where B is the rotational constant. There is no magnetic field applied. 30

3.6 The effective dipole moment of $X^2\Sigma$,$G = 1$,$N = 1$ states of YO. 30

3.7 The Stark-Zeeman shift of YO at different θ_{EB} (the angle between electric and magnetic fields). The strength of applied electric field is 1 kV/cm. Panels (a-c) correspond to θ_{EB} of 0°, 45° and 90°, respectively. 33

3.8 The stark-zeeman shift of YO at different θ_{EB}. The applied electric field is 1 kV/cm. Panels (a-c) correspond to θ_{EB} of 0°, 45° and 90°, respectively. 33

3.9 The Stark-Zeeman shift with different Hamiltonian terms excluded. For all the panels, all the Hamiltonian terms are contained except for optional spin-rotation coupling and dipolar interaction. The left panels include both spin-rotation coupling and dipolar interaction. The middle panel includes only dipolar interaction; the right panel includes only spin-rotation coupling. 1 kV/cm electric field is applied for all the panels with $\theta_{EB} = 0°$. Different number represents different quantum state: (1) $m_G = 1$, $m_N = 0$; (2) $m_G = 0$, $m_N = 0$; (3) $m_G = -1$, $m_N = 0$; (4) $m_G = 1$, $m_N = -1$; (5) $m_G = 1$, $m_N = 1$; (6) $m_G = 0$, $m_N = \pm 1$; (7) $m_G = -1$, $m_N = -1$; (8) $m_G = -1$, $m_N = 1$; 35

3.10 The first sequence of loading YO into the magic state after AC MOT. First sweep the electric field up to 1 kV/cm without any bias magnetic field as shown in the left panel. Then, turn on the quadrupole magnetic field with a uniform 1 kV/cm electric field at 0° θ_{EB} as shown in the right panel. The molecules with initial state $F = 2$, $m_F = 0$ can be loaded into the magic state. The adiabatic dynamics are identical for all other θ_{EB}. 37

3.11 The second sequence of loading molecules into the magic state after AC MOT. First sweep the uniform magnetic field up to 1 Gauss without any bias electric field as shown in the left panel. Then, turn on a uniform electric field of 1 kV/cm at 0° θ_{EB} as shown in the middle panel. Lastly, switch the uniform magnetic field to a 3D quadrupole magnetic field with a uniform 1 kV/cm electric field applied as shown in the right panel. The molecules with initial state $F = 1$, $m_F = 0$ can be loaded into the magic state. The adiabatic dynamics are identical for all other θ_{EB}. 38

4.1 Schematics of OH density calibration by H_2 Raman scattering. (a) The diagram of the laser arrangement. (1) half waveplate, (2) polarization beam splitter (GLB10-UV), (3) 90/10 beam splitter, (4) science chamber filled with OH/H_2, (5) a powermeter, (6) a fast photodiode (DET10A). (b) The photon collection system. (i) the illuminated object, (ii) UV lens (f=30 mm, diameter=25 mm), (iii) a color filter (UG11), (iv) an interference filter (Omega 313BP10), (v) a PMT (Hamamatsu R3788), (vi) an adjustable optical slit 45

4.2 Transmission spectrum of the filter array of the collection system as shown in Fig. 4.1 (b). 45

4.3 Saturation energy measurement of OH. The blue dots are experimental data. The red solid line is theoretical fitting with the formula $A\frac{\frac{I}{I_0}}{1+\frac{I}{I_0}}$. The fitted saturation energy is 38 μJ. 8 μJ is chosen as the incident laser energy so as to maintain the linear relation between laser energy and OH LIF. 47

4.4 Measurement of FOV (field of view) and DOF (depth of field) of the photon collection system. The photon collection system is as same as shown in Fig. 4.1 (b). (a) schematic diagram. DOF (FOV) is defined as FWHM of position-dependent collection effciency (b-d). (b) DOF of the collection system along the X-axis with a 20 mm FWHM. (c) FOV of the collection system along Y-axis with a 2.5 mm FWHM. (d) FOV of the collection system along Z-axis with a 6 mm FWHM. Different FOV between Y-axis and Z-axis is due to different length of the PMT area in these two dimensions. 48

4.5 Measurement of laser beam size. By translating a razor blade orthogonally across the laser beam in front of the power meter, the laser beam size can be measured. The blue dot is experimental data. The blue solid line is a theoretical error function fit (a*erf((x-b)/c)+d). The FWHM of the measured beam size is 0.78 mm. 50

4.6 The relation between LIF and slit width. The slit width is set to 0.75 mm to maintain a uniform density along X-axis. The dashed line is a guide to the eye. 51

4.7 A relation between LIF and measured laser energy in the constrained detection region. The detection region is constrained by the crossing volume between the 0.78 mm diameter laser beam and the 0.75 mm wide slit in the imaging plane. The laser energy is tuned by translating a second razor blade across the laser beam. The razor blade is placed between the beamsplitter and the PBS. The linear relation confirms homogeneity of density along this dimension. The measured OH LIF signal is 13.4 pVs within the constrained detection volume. 52

4.8 The temporal profile of the pulsed laser. The black dashed line is a Gaussian fit. The red solid line is experimental data. The fitted FWHM of the pulse laser is 8.5 ns. 54

4.9 OH absorption spectroscopy in the vicinity of 282 nm. There are two transition lines which are attributed to Q_{21} and Q_1. The spectrum can be fit by double Gaussian distributions and the laser linewidth is around 12 GHz. 54

4.10 The relation between FOV and the detectable portion of illuminated population. Once the FOV is larger than 2.5 mm, more than 95% of total fluorescence can be collected. 55

4.11 A comparison of OH saturation spectrum between experiment and simulation. The circle dots represents experimental data. The blue solid line represents results from simulation. All the parameters used in the simulation are from the previous measurements. There is only one free parameter for amplitude scaling. 57

4.12 Time-evolution of populations in both ground and excited states. The solid line represents population in the excited state. The dot-dash line represents population in the ground state. The dash line represents appearance of laser pulse. About 2% population is excited. 58

4.13 scattering vs angle 60

4.14 Raman scattering signal at different H_2 filling pressures. The blue dots are experimental data. The blue solid line is a linear fit. The slope of the linear fitting correspond to the scattering signal and is 1.2±0.1 pVs/Torr. 62

5.1 Details of Even-Lavie valve. The figures are gotten from a manual of Even-Lavie valve. 69

5.2 A comparison between used and new gasket (2-04-100) under 50X microscope. The diameter of the center hole is 200 μs. 70

5.3 A comparison between unpolished and polished plunger under 10X microscope. . . 70

5.4 Schematic diagram, not to scale. (1) Even-Lavie valve. (2) 70 K radiation shield, of which two side panels are not shown. (3) 2nd stage of Cryomech PT807 10 K cryostat. (4) home-built conical copper skimmer. (5) Lakeshore DT-670 silicon temperature diode used for measuring the skimmer temperature. (6) 282 nm pulsed UV laser. (7) LIF collection lens. (8) Fast ion gauge (FIG). (9) Micro-channel plates (MCP). r_{vs} is the distance between the valve and the skimmer. r_{sf} is the distance between the skimmer and the FIG. r_{sl} is the distance between the skimmer and the laser. r_{sm} is the distance between the skimmer and the MCP. 73

5.5 (a) Neon throughput for varying values of the conical skimmer temperature. The stagnation pressure is 400 psi for panel (a) and $r_{vs} = 3\ cm$ for panels (a-b). The transmitted Neon is measured at $r_{sf} = 36\ cm$ for panels (a-c). (b) Peak Neon signal before and after the skimmer at various stagnation pressures between 250-800 psi. The black solid line is a linear fit through the origin. A data point taken at 35 K (orange diamond) is included for comparison. (c) Peak Neon signal at different r_{vs} with stagnation pressure 200 psi. A data point taken at 35 K (orange star) is shown for comparison. 75

5.6 (a) Metastable Neon (Ne*) peak signal vs conical skimmer temperature. The stagnation pressure is 200 psi. $r_{vs} = 1.8\ cm$ for panels (a-c). The discharge delay is fixed at 83 μs. Each shot of experiment is reflected as a point in the plot. (b) Transmitted Ne* population vs. the discharge delay under two different temperatures. Ne* is seeded in the beam via dielectric barrier discharge (DBD) and detected at $r_{sm} = 160\ cm$. The DBD is composed of 17 cycles at 800 kHz. The stagnation pressure is 350 psi for panels (b-c). The delays here are measured relative to the valve firing for panels (b-c). (c) Neon pulses measured by FIG at $r_{sf} = 36\ cm$ with the discharge on or off at 8 K. The discharge has an 83 μs delay relative to the valve firing, starred in panel (b). This optimum Ne* discharge timing occurs at the center of the neon beam, as evidenced by the clear depletion right at the peak position. . . 77

5.7 (a) The beam shape of Ne* vs conical skimmer temperature. Beam shape ξ is defined as how close the time of flight profile at a certain temperature is to the unclogged and nearly Gaussian profile observed at 8 K. The inset panel shows transmitted Ne* beams at different skimmer temperatures. The double peak structure is related to minority species generated during the discharge, see the main text. (b) The Ne* peak signal vs ξ. From the bottom left to the top right, the temperature varies from 35 K to 8 K. The stagnation pressure is 200 psi and r_{vs}= 1.8 cm for panels (a-b). Each shot of experiment is reflected as a point in the plot. 79

5.8 A direct comparison between a 300 K commercial skimmer and an 8 K home-made skimmer for use with a hydroxyl radical (OH) beam. The OH density is measured at a fixed position behind the skimmer ($r_{sl} = 6.6\ cm$) suitable for a molecular guide. The blue circle data is taken with an 8 K skimmer and a valve-laser distance of 8.4 cm and the orange diamond data is taken with a 300 K skimmer (Beam Dynamics model: 50.8) and a valve-laser distance of 20.9 cm. The solid lines are Gaussian fits for extracting the relative beam widths. The arbitrary scales for the left and right axes are in the same units. The speed ratio of OH radicals for the two skimmers is identical as expected. Time is recorded relative to valve firing and OH is generated with the same discharge time delay (83 μs) used for Ne*. 83

6.1 The pictures of the exit side of the malfunctioned second-generation stark decelerator. 86

6.2 A picture of current surface flashover of an insulation mount made of Macor. The blue light is caused by the surface flashover. (+) means the electrode is connected to a positive polarity; (−) means the electrode is connected to a negative polarity; (⊥) means the electrode is grounded. Triple junction occurs where vacuum, metal and insulator meet with each other. 88

6.3 A simulated electric field distribution near a triple junction. The figure is taken from Ref.[84] 88

6.4 Different views of the third-generation stark decelerator. (1) The body frame made of aluminum. (2) The clamps made of 316 SS. (3) The decelerator rods made of 316 SS. (4) The high voltage insulator made of Pyrex glass. (5) The decelerator pins made of 316 stainless steel (SS). 90

6.5 Surface quality of decelerator pins under different ways of polishing. Panel (a-d) share the identical scale. Each picture shown here is selected from a bunch of pictures taken at different locations of the same pin and roughly represents the averaged surface quality. All the pictures are taken under 50X microscope. (a) The surface quality of a decelerator pin after grinding without any extra treatment. There are three grinded pins ready for three other treatment. (b) The surface quality of a decelerator pin after three-minutes electro-polishing. (c) The surface quality of a decelerator pin after several-minutes 4000 grit sandpaper. (d) The surface quality of a decelerator pin after after several-hours tumbling. 92

6.6 The comparisons between two different DC guiding modes. The left column shows the voltage configuration at different guiding modes. The right column shows the effective 2D trap experienced by OH in the X-Y plane. The effective 2D trap is acquired by averaging the Stark energy over one full period of the decelerator along Z-axis at each X-Y position. The energy contour is separated by 10 mK. 95

6.7 Experimental data of ToF at different guiding mode. The decelerator runs at $\pm$ 6 kV.The red circles represent the OH ToF signal at $++--$ guiding mode. The blue square represent the OH ToF signal at $+-+-$ guiding mode. 96

6.8 The OH ToF of an optimized stark decelerator for different final velocities. The dots represent the experimental data and the solid line represent the results from simulation. 97

7.1 Inelastic cross section between $|f, m_j = 3/2\rangle$ state of OH and neon at different electric field strength. Different color represents different collisional energy. 101

7.2 The electric field distribution experienced by OH along the decelerator when the decelerator operates in $++--$ configuration ($\pm$ 1 kV). The distribution is calculated by running a Monte Carlo simulation and counting how much percentage of time spent on each electric field during propagation. The total area underneath the curve is normalized to 1. There is a pronounced peak corresponding to the dominant electric field contribution, which is 5.5 kV/cm for $\pm$ 1 kV applied voltages. 103

7.3 Experimental setup for OH-Neon intra-beam collisions. The stark decelerator operates at $++--$ configuration as introduced in Chapter 6. There are two sets of LIF collection system installed at the 40th stage and 333rd stage of the decelerator, respectively. A RGA (SRS 300) is installed at the exit of the decelerator. The first 40 stages of the decelerator are used to do state preparation. The stages from 40 to 333 are used as a collisional region. A cryogenic skimmer is installed between the valve and the decelerator so as to increase the neon throughput for collisions. 105

7.4 The measurement of mean velocity and velocity spread for both OH and neon. By accurately translating the valve to different skimmer-valve distances along the Z-axis, a series of ToF can be recorded so that both the peak arrival time and velocity spread can be extracted by fitting the ToF with a Gaussian function. (a)The measurement of OH. The linear fit shows the speed of OH is 803$\pm$1 m/s. The FWHM of the OH ToF at the exit of decelerator is 80 μs, corresponding to 10.7 m/s velocity spread. (b) The measurement of neon. Due to appearance of skimmer clogging, the global fit does not represent the authentic velocity. The neon velocities are also calculated by nearby two points and labeled in the plot. The FWHM of the neon ToF at the exit of decelerator is 147 μs, corresponding to 16.3 m/s velocity spread. 107

7.5 The summary of data analysis procedure at ± 6 kV. (a) OH ToF measured at 40th and 333rd stage of the decelerator with certain neon density. The dots represent experimental data. The solid line represent a Gaussian fit. The OH population is calculated by integrating the area underneath the fit. (b) Neon ToF at different valve conditions, corresponding to different neon densities. (c) The relation between normalized OH population and neon density. The normalized OH signal is calculated by dividing the total OH population measured at 333rd stage with the total OH population measured at 40th stage [103]. The data can be fitted by exponential function: $Ae^{-\beta n_{Ne}}$, of which β is the loss rate. 110

7.6 Summary of OH loss rate at different applied voltage. The black circle represents the data is taken with a cryogenic skimmer. The red square represents the data taken with a commercial skimmer. 112

Chapter 1

Introduction

1.1 Why Polar Molecules?

Since the development of cold atoms for the past 30 years has laid a strong foundation for the growth of cold molecules, it comes as no surprise for us to witness much unprecedented progress in cold molecules during the recent decade. Compared with cold atoms, polar molecules have more complex internal energy levels and interact with each other via a long-range anisotropic dipolar force [1]. These distinctions attract more and more experiments to extend from cold-atom side to cold-molecule side, such as transitions from searching permanent electric dipole moment (EDM) by utilizing high-Z atoms (e.g. Ti) [2] to using heavy dipolar molecules [3]; from laser cooling of atomic species [4] to pursuing 3D magneto-optical trap (MOT) of dipolar molecules [5]; from studying magnetically tunable isotropic short-range interaction [6] to investigating anisotropic and electric-field controllable long-range interaction [7]. For molecular physics, the experiments of interest can be roughly divided into two categories: discovery of the natural properties of particles and quantum control engineering. In this section, I am going to describe some of the major progress on these two categories.

1.1.1 Discovery of the Natural Properties of Particles

According to the Standard Model, the fact that weak interactions do not preserve charge-parity symmetry leads to nonuniform charge distribution over the particles. In other words, particles have permanent EDM. It is very important to clarify the existence of EDM so as to check the

correctness of Supersymmetry or others. Scientists have been using heavy atoms [2] to search for the EDM for years till recently it is proposed that the large internal electric field of polar molecules (tens of GV/cm, which is much larger than hundreds of kV/cm electric field realized in lab) are able to enhance the detection sensitivity of EDM measurements. The measurements based on heavy polar molecules such as YbF [8], ThO [9] and HfF^+ [10, 11], have already set a decent upper bound of the electron-EDM and help eliminate some of the supersymmetric theories. It will be exciting to witness the discovery of EDM in order to have a better understanding of the fundamental symmetry of the universe.

Another application of polar molecules is to measure the time evolution of the fundamental constants [12]. The values of α (fine structure constant) and $\mu = m_p/m_e$ (proton-to-electron mass ratio) determine numerous details of the present universe. Any slight shift of these constants will lead to completely distinctive cosmos. Thus, it is very important to know whether the fundamental constants are certainly time independently invariant, which can help us explain some mysteries, such as why today's world is made of matter instead of antimatter, and so on. Since the fine structure splitting and vibration splitting of polar molecules exhibit different dependence on fundamental constants, by choosing two nearly degenerate states with different electronic and rovibrational quantum numbers, the detection sensitivity can be enhanced by several orders compared with utilizing atoms [13].

Cold and ultracold quantum chemistry has become more and more popular [14, 15]. In the field of astrophysics, molecular collision in near-cold regime ($1<T<50$ K) is the main mechanism for many relevant astrophysical phenomena, such as the formation of cold molecular clouds [16]. For computational chemistry, the accurate measurement of the cross section between dipolar interactions, such as OH against ND_3 [17] and CH_3F against ND_3 [18], can be used to validate the ab initio calculations of potential energy surface (PES) of the intermolecular interactions. More details related to quantum chemistry will be discussed in Chapter 7.

1.1.2 Quantum Engineering

Compared with atomic interaction, the dipolar interaction is long-range and anisotropic, which enables more symmetry breaking and prompts the appearance of new quantum phases. These unique properties of polar molecules offer attractive solutions to engineer complex systems.

It is predicted that with polar molecules fixed in a 2D plane [19] and polarized along the normal of the plane, the bosonic sample can have crystalline phase, which cannot be realized by atomic species with only short-range isotropic peudopotential. If the polar molecules are arranged in 2D optical lattice, more exotic phases, such as fractional Chern insulator, can be realized [20], depending on the relative angle between 2D plane and molecular polarization.

The polar molecules can also work as a medium for quantum information. The rotational states of polar molecular ions can be used as quantum storage qubits. The dipole-dipole interaction induced by microwave [21] can entangle nearby polar molecular ions and enable quantum gate operation. Since the entanglement does not rely on thermal motion, this technique works as a promising solution to the scalable and heating problems in atomic ions.

For the neutral polar molecules, such as ultracold NaK, long coherence time up to 1 second [22] has been demonstrated and it opens the door of realizing quantum memory by utilizing neutral molecules.

1.2 Different Methods of Molecular Cooling

Since the room-temperature molecules move at several hundred meters per second, the thermal motion can dramatically weaken the quantum effects (kelvin or below) we are interested in. Moreover, the occupancy of numerous rovibrational states can also wash out the quantum-state dependent effects. Thus, in order to observe majority of the phenomena mentioned above, it is very important to keep the thermal energy lower than the energy scale we care about while maintaining the molecules in single rovibrational state. There are many different ways of cooling molecules, which can be roughly divided into two categories—direct and indirect cooling methods.

1.2.1 Direct Cooling Methods

The most common direct cooling method is called buffer gas cooling [23], which is suitable for almost all the species. By mixing the interested species with cryogenic cooled noble gas (e.g. helium/neon), both the thermal energy and internal energy of interested species can be dissipated via elastic collisions. With helium as a buffer gas, most of molecules can be cooled to rovibrational ground states and their kinetic energy is controlled within kelvin regime. Buffer gas cooling has already become a prerequisite method for many other cooling techniques, such as laser cooling of molecules [24–26], centrifuge deceleration [27], and so on.

Another general "cooling" method relies on a phase-space-conservative deceleration, such as Stark/Zeeman decelerator [28–31]. By periodically converting the kinetic energy into potential energy, the pulsed molecular beam can be slowed down close to rest. Stark decelerator can work for most of the polar diatomic molecules following Hund's case (a) rule and Zeeman decelerator works for the molecules with a favorable magnetic dipole moment and mass ratio. Recently, another way of decelerator—centrifuge decelerator [27] is demonstrated, which can work for a continuous beam and open more research possibilities. These decelerators have been widely used in crossed beam experiment [32], quantum state selection, and so on.

Laser cooling acts as a more efficient method, but also with more limitations. It is applicable for the molecules whose electronic structure is largely decoupled from the vibration modes, in other words, large Franck-Condon coefficients. With reasonable number of laser, the cooling transitions can be largely cycled. Within this decade there have been enormous achievements in laser cooling of polar molecules, from transverse laser cooling [33, 34], to molecular beam slowing [35–37], to 3D MOT [24, 25], to cooling below-Doppler limit[26], to cooling close to recoil limit [38, 39]. So far, CaF has been cooled to 5 μK and loaded into an array of optical tweezers [40], which paves the way for quantum computing and engineering many-body physics.

1.2.2 Indirect Cooling Methods

Hitherto, the most successful indirect cooling method is based on magneto-association. By first cooling two atomic species to ultracold regime, then weakly-bound molecules are generated by sweeping magnetic field through Feshbach resonance. A technique called stimulated Raman adiabatic passage (STIRAP) is used to bring excited molecules to rovibrational ground state. Recently, KRb [41] becomes the first quantum degenerate dipolar molecule with temperature below 0.3 times of its Fermi temperature. There are also many other species under investigation, such as RbCs [42], NaK [43], NaLi [44], NaRb [45], and so on. Lately, optical tweezers plus photo-association turns into another way of generating ultracold polar molecules, e.g. the formation of NaCs [46].

In general, there is more progress on the Hund's case (b) molecules than Hund's case (a) molecules. This thesis is going to introduce several progress achieved for hydroxyl radical (OH)—one of the most popular Hund's case (a) molecules.

Chapter 2

Hydroxyl Radical Spectroscopy in a Magnetic Trap

Atomic and molecular spectroscopy serves as a cornerstone for most branches of Atomic, Molecular and Optical Physics (AMO) studies, such as molecular cooling [5], precision measurement [47], quantum information [21], and so on. Thanks to my brilliant predecessors' hard work, our group have already built a solid understanding of the molecular structures of several polar molecules and had a particular interest in hydroxyl radical (OH) in the past decade. The goal of this chapter is to add more pieces of information related to OH level structures, which should be helpful for future studies.

2.1 Hund's Cases

In a diatomic molecule, there are several various components of angular momentum, including spin of electrons (S), orbital angular momentum (L), rotation of nuclear frame (R). In order to account for all the angular coupling possibilities with respect to the presence of electrostatic interaction, five different schemes, named Hund's cases (a-e), are proposed. The appropriate scheme (Hund's case) means the full Hamiltonian of the molecule under the relevant basis has the smallest number of off-diagonal components.[1] Except significantly heavy dipolar molecules, such as ThO, or highly excited Rydberg molecules, most of the common dipolar molecules follow either Hund's case (a) or (b). Thus, this section will only focus on Hund's case (a) and (b).

[1] In principle, you can express a molecule in any basis. However, the more diagonal, the easier to analyze.

2.1.1 Case (a)

Hund's case (a) (Fig. 2.1) represents molecules whose spin-orbit coupling is much weaker than electrostatic interaction, but much stronger than spin-rotation coupling. Due to the strong Coulombic interaction, the orbital angular momentum (L) of the electron is pinned to the internuclear axis with a projection Λ. Due to the strong spin-orbit coupling, electron spin (S) is also projected along the internuclear axis with a quantum number Σ. Thus, the magnetic dipole moment of the molecule is represented by the quantum number along the internuclear axis—Ω, which is sum of Λ and Σ. Magnetic and electric dipole moments are strongly coupled with each other as a result of them being aligned along the internuclear axis. The strongly coupled dual dipole moments will make Hund's case (a) molecules experience enhanced spin-flip loss inside a magnetic trap as a uniform electric field is applied. The details will be discussed in Chapter 3.

2.1.2 Case (b)

If the spin-orbit coupling is much weaker than spin-rotation coupling or even zero (L=0), the molecules can be generally categorized into Hund case (b) (Fig. 2.2). The electron spin (S) is coupled to the rotation of nuclear frame ($R = N$), instead of the internuclear axis. If the applied external field is large enough to break spin-rotation coupling, the electric and magnetic dipole moments can be decoupled from each other. So far, most of ground states of laser-coolable molecules are classified as Case (b).

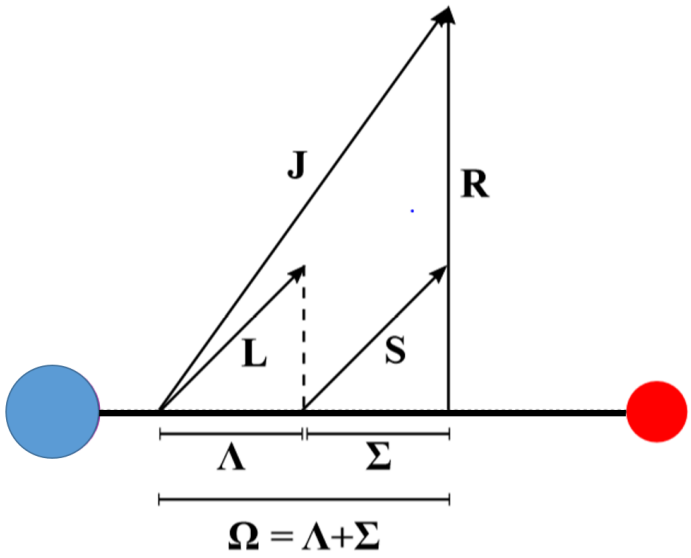

Figure 2.1: Coupling diagram for Hund's case (a) molecules. The orbital angular momentum L is coupled to the internuclear axis by Coulombic interaction with a projected quantum number Λ. The spin of electron S is also projected onto the internuclear axis by spin-orbit coupling with a quantum number Σ. Σ and λ couple together and form Ω, which is the projection of total angular momentum J=R+Ω.

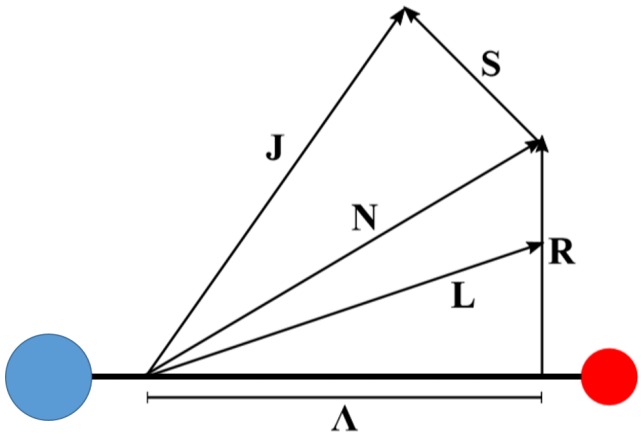

Figure 2.2: Coupling diagram for Hund's case (b) molecules. Due to the a stronger spin-rotation coupling, spin of electron (S) is coupled to the vector N=R+L to form total angular momentum J.

2.2 Zeeman Shift of OH States

2.2.1 Zeeman Shift of OH Ground State $X^2\Pi_{3/2}, f$

2.2.1.1 Zeeman Shift of a Pure Hund's Case (a) Molecule

After ignoring the hyperfine interaction, the molecular g-factor of a linear Zeeman effect can be represented by g_J. Then, the Zeeman energy of a molecular state can be expressed as:

$$E_z = g_J m_J \mu_B B \tag{2.1}$$

For a pure Hund's case (a) molecule with magnetic field along Z-axis of space-fixed coordinates, the magnetic moment of the Zeeman Hamiltonian can be expressed as:

$$\mu = g_L \mu_B T^1_{p=0}(L) + g_S \mu_B T^1_{p=0}(S) \tag{2.2}$$

, where p index refers to space-fixed coordinates, and p=0 means the component along Z-axis. [48]

To evaluate the first term in Eq. 2.2, we need to transform from space-fixed coordinates to molecule-fixed coordinates as shown in page 605 of Ref. [48]. As a result, the Zeeman Hamiltonian from orbit angular momentum contribution can be written as:

$$H_L = \langle \Lambda; S, \Sigma; J, \Omega, m_J | \, g_L \mu_B B_Z \sum_q D^{(1)}_{0q}(\omega) T^1_q(L) \left| \Lambda'; S, \Sigma; J', \Omega', m_J \right\rangle \tag{2.3}$$

, where $D^{(1)}_{0q}(\omega)$ is the rotation matrix that transforms from space-fixed coordinates to molecule-fixed coordinates; ω is the Euler angle between space-fixed coordinates and molecule-fixed coordinates; q index refers to molecule-fixed coordinates.

If the applied magnetic field is the dominant quantization axis, only q=0 term will survive. Eq.2.3 can be simplified to:

$$H_L = g_L \mu_B B_Z \langle \Lambda | \, T^1_0(L) \left| \Lambda' \right\rangle ((2J+1)(2J'+1))^{1/2} \begin{pmatrix} J & 1 & J' \\ -m_J & 0 & m_J \end{pmatrix} \begin{pmatrix} J & 1 & J' \\ -\Omega & 0 & \Omega' \end{pmatrix} \tag{2.4}$$

The familiar equation is derived after using parity eigenstates of good Hund's case (a) to evaluate Eq. 2.4:

$$H_L = g_L \mu_B B_Z \Lambda \Omega m_J / (J(J+1)) \tag{2.5}$$

The S component of Eq. 2.2 can be evaluated in a similar manner. The sum of S and L components in Eq. 2.5 yields the total expression:

$$E_z = \frac{(g_L \Lambda + g_S \Sigma)\Omega}{J(J+1)} m_J \mu_B B_Z \tag{2.6}$$

Then, g_J can be identified as:

$$\begin{aligned} g_J &= \frac{(g_L \Lambda + g_S \Sigma)\Omega}{J(J+1)} \\ &= \frac{(\Lambda + 2\Sigma)\Omega}{J(J+1)} \end{aligned} \tag{2.7}$$

Assuming OH ground state $X^2\Pi_{3/2}$ is a good Hund's case (a) molecule, g_J of ground state $J = 3/2$ state equals to $4/5$, corresponding to a magnetic moment $\mu = (4/5)(m_J = 3/2)\mu_B = 1.2\mu_B$. This is the magnetic dipole moment of OH which have been used in all Zeeman level calculations and temperature derivation. [49]

2.2.2 Zeeman shift of Intermediate Case

However, since the ratio ($\lambda \equiv A/B$) between spin-orbit coupling parameter $A = -139$ cm^{-1} of OH ground state and its rotational constant $B = 18.5$ cm^{-1} is close to order unity (-7.5), the ground state of OH is contaminated by the mixture of Case (b) and does not perfectly follow a pure Hund's case (a) rule anymore. Therefore, it is essential to evaluate the Zeeman Hamiltonian with the correct eigenstates (i.e. not simply Hund's case (a) states) to calculate the Zeeman shift of OH. The expression that describes g_J in this intermediate coupling regime is as follows [50]:

$$g_J = \frac{1}{J(J+1)} \left(3/2 + \frac{2Y^2 - \frac{3}{2}\lambda + 3}{X} \right) \tag{2.8}$$

, where $Y \equiv ((J+3/2)(J-1/2))^{1/2}$, and $X \equiv (4(J+1/2)^2 + \lambda(\lambda-4))^{1/2}$.

For a pure Hund's case (a) molecule, as we take $\lambda \to -\infty$, $g_J = 4/5$. For a good Hund's case (b) molecule, $g_J = 1$ is recovered as we take $\lambda \to 0$. The different g-factor between two Cases can

be explained in a simple physical picture. In Hund's case (a), the electron spin and orbit angular momentum are both tightly coupled to the internuclear axis, forming the magnetic dipole moment. However, the rotation of molecular frame can average the dipole moment in the space-fixed frame somehow and result in a reduced g_J. In Hund's case (b), since the electron spin is decoupled from the internuclear axis, J is a good quantum number in space-fixed frame, which makes the g_J equal to 1.

With the experimental value $\lambda = -7.5$, the calculated value of g_J equals to 0.934, which is similar to the experimentally observed value of $g_J = 0.936$ [50]. This intermediate value of g_J reflects the intermediate decoupling of the spin from the internuclear axis. Thus, the magnetic moment that should be used for OH is not 1.2 μ_B, but rather 1.4 μ_B with a correction of 17%. Our calculation is also confirmed later by Ref.[51].

2.2.3 How Does the Modified g_J Affect Our Previous Results?

As discussed in Ref. [49], the temperature of OH is extracted from a Zeeman depletion spectrum so that the modified g_J will have an impact on the interpretation of temperature.

2.2.3.1 RF Spectroscopy and Temperature Fits

Since the differential g-factor between $f, m_J = 3/2$ and $e, m_J = 3/2$ does not change with the g-factor modification, the conversion from RF frequency to magnetic field used for RF spectroscopy is not affected and the depletion spectra plots of population versus magnetic field remain unchanged.[49] However, the temperature fits to these plots require a correction. The depletion spectra is fit by the formula: $n(B) \propto B^2 \exp[-\mu B/kT]$. To keep the fits from changing, if μ increases by 17% then T must also increase by 17% to maintain an identical exponent. Thus, temperatures from RF spectra must be revised upwards by 17%. The unevaporated temperature increases from 45 K to 54 K.

2.2.3.2 Avoided Crossings

During evaporation, we rely on the avoided crossings between f and e states to remove the populations transferred into e-state. The modified g_J will shift the position of avoided crossings between f and e states. The larger g-factor means the levels converge more quickly. Then, the lowest avoided crossing shifts from 496 Gauss down to 427 Gauss. The new location of avoided crossing does affect our explanation of the spectroscopy below 500 Gauss evaporation and also lead us to explore a new explanation for the strange spectrum shape under 500 Gauss.[49, 52]

2.2.4 Zeeman Shift of OH Excited States

The first excited state of OH is $A^2\Sigma$ and can be well described by Hund's case (b). Since the ground state $X^2\Pi_{3/2}, f$ has a positive parity, in order to drive optical transitions, the excited state should have a negative parity. Then, the rotational quantum number N of excited state should equal to 1. Fig. 2.3 (a) shows the possible optical transitions between ground state $X^2\Pi_{3/2}, f$ and excited state $A^2\Sigma, \nu = 0, N = 1$ used for optical depletion spectroscopy. Optical depletion spectroscopy relies on non-zero differential Zeeman shift between ground and excited states in optical frequency domain.

There are two transitions available for optical depletion spectroscopy—Q1 and Q21, which correspond to the excited states J=3/2 and J=1/2, respectively. The energy split between J=3/2 and J=1/2 is due to spin-rotation coupling.

In order to plot relative Zeeman shift of the excited state, we only need consider contributions from the spin-rotation term and Zeeman shift terms. Then, the Hamiltonian can be expressed as $H = H_{SN} + H_{B_z}$.

The spin-rotation term (H_{SN}) is expressed as:

$$\begin{aligned} H_{SN} =& \langle A; N, J, m_J | \, \lambda T_0^1(N) T_0^1(S) \, | A; N, J', m'_J \rangle \\ =& \lambda (-1)^{J+N+S} \begin{Bmatrix} S & N & J \\ N & S & 1 \end{Bmatrix} \\ & \sqrt{S(S+1)(2S+1)N(N+1)(2N+1)} \end{aligned} \tag{2.9}$$

, where for OH excited state $A^2\Sigma, \nu = 0, N = 1$, $\lambda = 0.226\ cm^{-1}$.

The Zeeman shift term from electron spin S can be expressed as:

$$\begin{aligned} H_{B_z} =& \langle A; N, J, m_J | \, T_0^1(L) \, | A; N, J', m'_J \rangle \\ =& g_s \mu_B B_Z (-1)^{J-m_J+J+N+S+1} \begin{pmatrix} J & 1 & J' \\ -m_J & 0 & m'_J \end{pmatrix} \begin{Bmatrix} S & J' & N \\ J & S & 1 \end{Bmatrix} \\ & \sqrt{S(S+1)(2S+1)(2J'+1)(2J+1)} \end{aligned} \tag{2.10}$$

where g_s is g-factor of electron spin; μ_B is Bohr magneton; B_Z is the magnetic field applied.

After diagonalizing the Hamiltonian, the Zeeman shift of excited state $A^2\Sigma, \nu = 0, N = 1$ is shown in Fig. 2.3 (b).

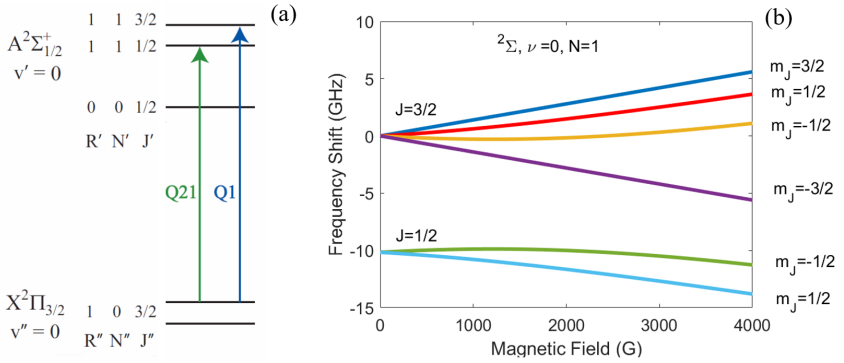

Figure 2.3: The excited states used for optical depletion spectroscopy. (a) Optical transition diagram. Both Q21 and Q1 can be used for optical depletion. (b) The Zeeman shift of excited state ($A^2\Sigma, \nu = 0, N = 1$).

2.3 Optical Depletion Spectroscopy in a Magnetic Trap

2.3.1 Experimental Sequence

Fig. 2.4 shows the main experiment sequence, which is almost as same as shown in Ref. [49]. The only difference is that we replace the RF spectroscopy with an optical depletion spectroscopy. The details of the experiment is briefly mentioned below. More information can be found in [49].

OH is generated by DC discharging of water vapor. After a supersonic expansion with krypton as a carrier gas, OH can be cooled to rovibrational ground state with a forward velocity of 440 m/s. With a 140-stages stark decelerator, OH molecules can be slowed down from 440 m/s to 35 m/s. At the end of the stark decelerator, a pair of permanent magnets is installed and forms a quadrupole magnetic trap. By applying high voltage on the magnet, the last electrical potential hill is formed between two magnets and is able to stop the molecules to rest near the trap center. Once the electric field is removed, we can acquire a 55 mK trapping sample. [49, 52]According to LIFbase,[53], the wavelength of both Q21 and Q1 transitions is around 308 nm. Thus, a 308 nm CW laser is prepared to drive transitions from the ground state $\left|X^2\Pi_{3/2}, \nu = 0, J = 3/2\right\rangle$ to the excited electronic state $\left|A^2\Sigma, \nu = 0, N = 1\right\rangle$ to do the optical depletion. The laser system consists of a tunable dye laser (616 nm) with a linewidth of 10 MHz and a doubling cavity, which converts the wavelength from 616 nm to 308 nm. The dye laser is locked to an external cavity and wavelength is monitored by a wavemeter with a resolution up to 50 MHz, which is comparable to the Doppler broadening from 50 mK sample. After frequency doubling, we have 0.4 mW output power at 308 nm with a linear polarization. With the exposure time of depletion laser last for 12 ms, about 25% of the total population can be depleted with the laser frequency matching the Q21/Q1 transitions. After the optical depletion, a 282 nm pulsed laser is used to drive the transition from the ground state $\left|X^2\Pi_{3/2}, \nu = 0, J = 3/2\right\rangle$ to the excited electronic state $\left|A^2\Sigma, \nu = 1, N = 1\right\rangle$ to check the population remaining after the optical depletion.

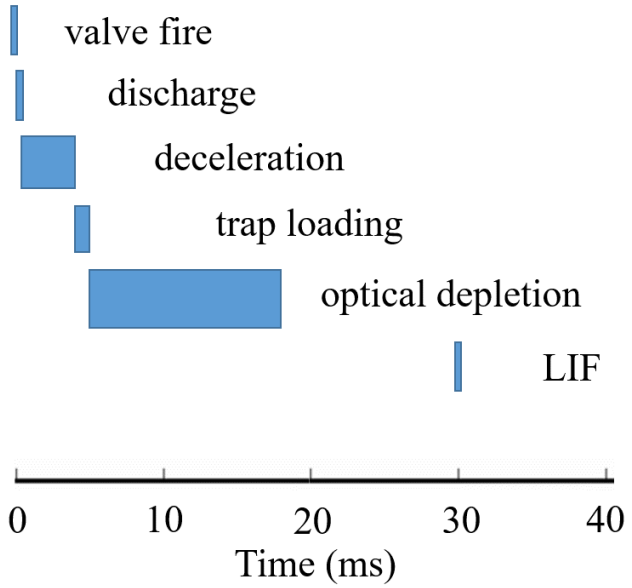

Figure 2.4: Experimental sequence. The main experiment sequence is same as shown in Ref. [49]. The only difference is that we replace RF spectroscopy with an optical depletion spectroscopy.

2.3.2 Results and Analysis

2.3.2.1 Optical Depletion Spectroscopy of Q1 Transition

Since selection rules only allow electric dipole transition with Δm_J=±1 and 0, for the ground state with m_J=3/2, there are two excited states can be driven to. One excited state is $^2\Sigma, J = 3/2, m_J = 3/2$, which corresponds to π transition. The other is $^2\Sigma, J = 3/2, m_J = 1/2$, which corresponds to σ^- transition. Fig. 2.5 shows the differential Zeeman shift for these two transitions.

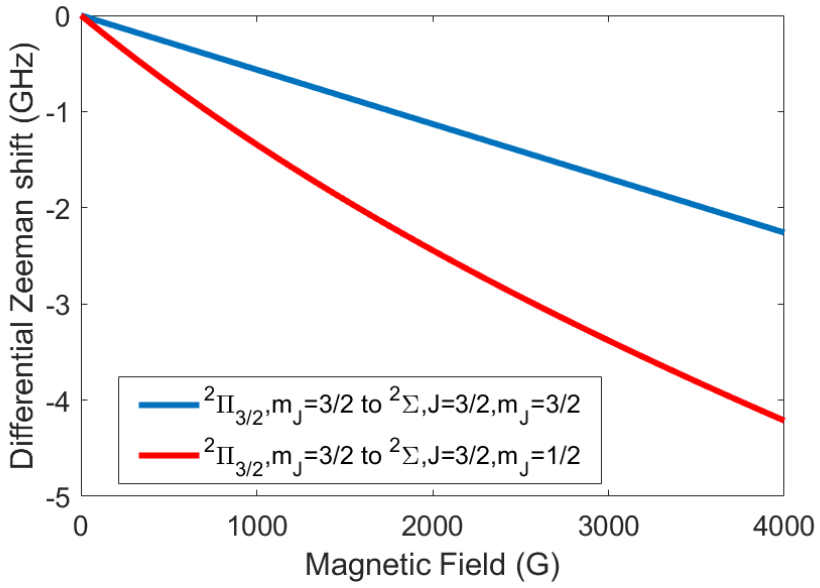

Figure 2.5: The differential Zeeman shift between $^2\Pi_{3/2}, m_J = 3/2$ and $^2\Sigma, J = 3/2$. The blue line corresponds to π transition—from $^2\pi_{3/2}, m_J = 3/2$ to $^2\Sigma, J = 3/2, m_J = 3/2$. The red line corresponds to σ^- transition—from $^2\pi_{3/2}, m_J = 3/2$ to $^2\Sigma, J = 3/2, m_J = 1/2$.

According to LIFbase [53], the Q1 transition line is around 307.933 nm (973.56 THz). With the frequency of depletion laser fixed at 973.5634 THz, we are able to check the relation between laser power and fractional depletion for a 12 ms exposure time. It is confirmed 0.4 mW is low enough and sits in a linear depletion regime. By tuning the laser frequency with a step 200 MHz, we are able to measure the optical depletion spectrum for Q1 line. The circles in Fig. 2.6 represent the experimental data.

Due to the fact that the relative angle between magnetic field and laser polarization varies over the whole magnetic trap, there are two possible transitions—π and σ^- [54]. In order to fit the data, we need figure out the ratio of contributions between π and σ^- transitions. The branching ratio between π and σ^- equals to the square of the Wigner3j ratio: between $\begin{pmatrix} 3/2 & 1 & 3/2 \\ -3/2 & 0 & 3/2 \end{pmatrix}$ and $\begin{pmatrix} 3/2 & 1 & 3/2 \\ -1/2 & -1 & 3/2 \end{pmatrix}^2$, which equals to 1.5. For the π transition, all the power of linear polarized light contributes to the optical depletion. However, for the σ^- transition, only half of the incident power can contribute to optical depletion due to the fact that the linear polarized light is superimposed of σ^- and σ^+. Thus, in total, the population depletion ratio between π and σ^- transition is factor three.

For each of the transitions, a thermalized Boltzmann distribution in a quadrupole magnetic trap can be expressed by equation: $n(\nu) \propto B^2(\nu) dB/d\nu \exp[-\mu B(\nu)/kT]$, of which $B(\nu)$ is derived from Fig. 2.5. The experimental data can be fit by a joint function, which sums up the contributions from both π and σ^- transitions with a ratio 3 to 1. The ratio of population depletion is reflected by the area ratio underneath two separate Boltzmann curves. The fit temperature is 59 ± 4 mK, which is consistent with the value from RF spectroscopy. The consistency also confirms the accuracy of differential Zeeman shift. The starting point of the fit Boltzmann distribution labeled with an arrow corresponds to the transition line of Q1. Compared with LIFbase, we are able to assign more accurate transition frequency—973.5624 ± 0.0001 THz.

2.3.2.2 Optical Depletion Spectroscopy of Q21 Transition

Compared with Q1 transition, Q21 transition has only one possible transition—σ^- from ${}^2\Pi_{3/2}, m_J = 3/2$ to ${}^2\Sigma, J = 1/2, m_J = 1/2$. Fig. 2.7 shows the differential Zeeman shift of Q21 line.

According to LIFbase, the Q21 transition line is around 307.933 nm (973.56 THz). Fig. 2.8

[2] see Eq. 2.45 and 2.46 in Ref. [55]

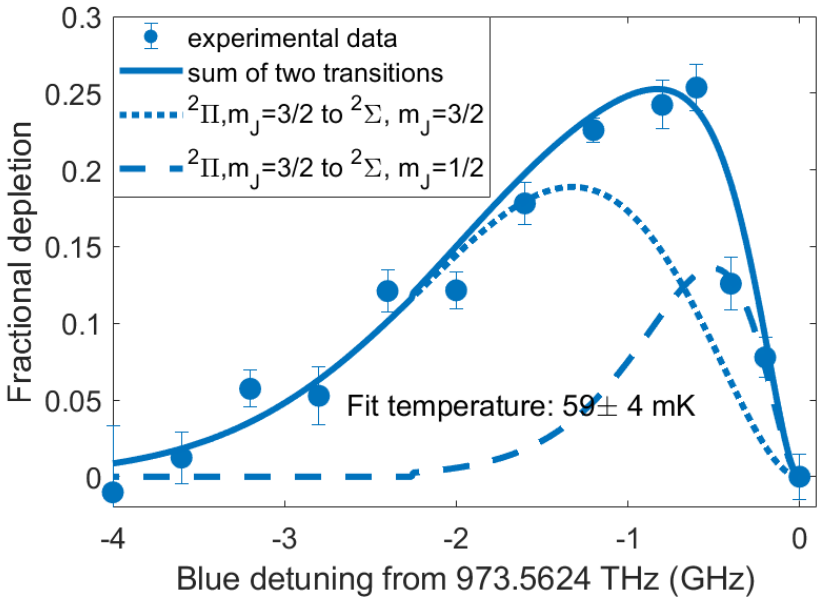

Figure 2.6: Optical depletion spectroscopy of Q1 transition. The solid line is the best fit curve with a sum of two Boltzmann distribution from π and σ^- transitions. The fit temperature is 59 ± 4 mK. The dash line represents the distribution from σ^- transition. The dot line represents the distribution from π transition. The area underneath the Boltzmann curve is proportional to the depletion population. The starting point of the fit Boltzmann distribution labeled with an arrow corresponds to the transition line of Q1, which is 973.5624 ± 0.0001 THz.

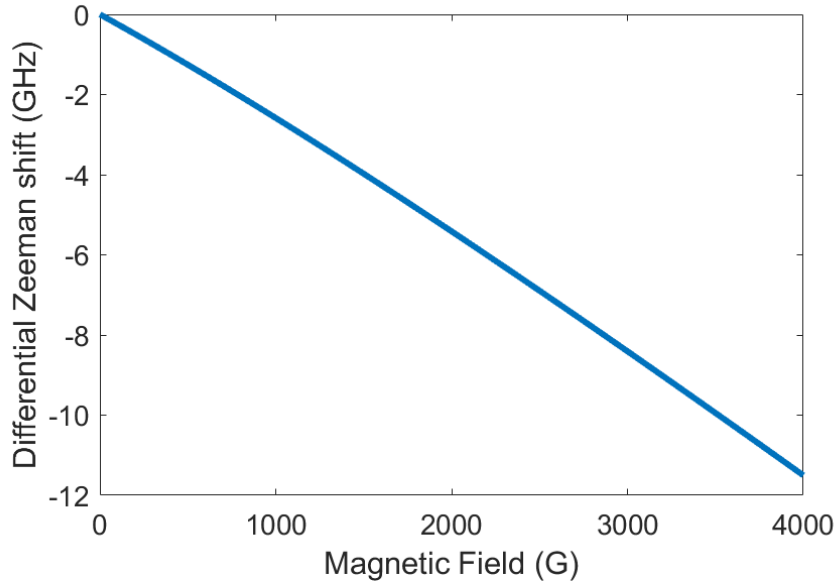

Figure 2.7: The differential Zeeman shift between $^2\Pi_{3/2}, m_J = 3/2$ and $^2\Sigma, J = 1/2, m_J = 1/2$.

shows the optical depletion spectrum of Q21 transition. Based on the differential Zeeman shift in Fig. 2.7, the experimental data can be fit by a Boltzmann distribution. The fit temperature is $60 \pm 4\ mK$, which shows a good agreement with all previous measurements. The frequency of Q21 transition is 973.5532 ± 0.0001 THz.

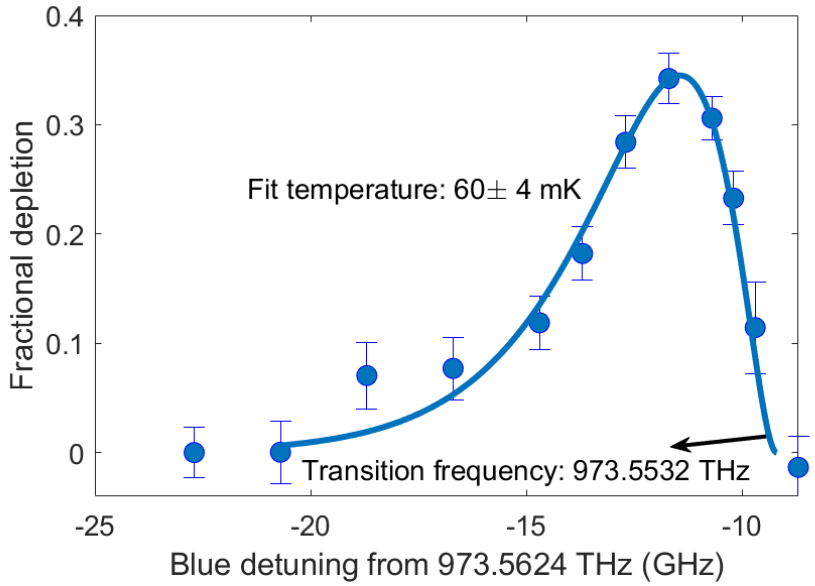

Figure 2.8: Optical depletion spectroscopy of Q21 transition. The circles are experimental data. The solid line is the best fit curve. The fit temperature is 60 ± 4 mK. The frequency of Q21 transition is labeled by an arrow corresponding to 973.5532 ± 0.0001 THz.

2.4 Conclusion

The optical depletion spectroscopy works well to measure the thermal temperature. Compared with RF spectroscopy, it has the advantage that it does not require an external electric field to remove the transferred population and this can avoid the enhanced spin-flip loss, which will be discussed in Chapter 3. In future, with an even larger laser power and a capability of detuning laser by 10 GHz within seconds, we may even use optical depletion to do evaporation.

Chapter 3

Spin-flip Loss for Doubly Dipolar Molecules

For magnetically trapped atomic species, spin-flip loss (Majorana loss) turns out to be an important loss mechanism as the Larmor frequency of atoms becomes comparable to the trapping frequency. Since the "small" precession frequency cannot guarantee atoms to adiabatically follow the alteration of quantization axis during oscillation, there is a probability that the atomic internal state swaps from a low-field-seeking state to a high-field-seeking state in the lab frame, leading to loss. The spin-flip loss imposed a major obstacle to prevent the atomic species from reaching quantum degeneracy until a time-orbiting potential trap was proposed and implemented [56]. For doubly dipolar molecules, the spin dynamics are even more complex in mixed electric and magnetic fields. In this chapter, we will talk about the electric-field-enhanced spin-flip loss mechanisms for both Hund's case (a) and (b) molecules, with application to OH and YO respectively.

3.1 Hund's Case (a) Molecules

As mentioned in Chapter 2, Hund's case (a) describes the kind of dipolar molecules whose spin-orbit coupling is much weaker than their electrostatic interaction, but much stronger than the spin-rotation coupling. For doubly dipolar Hund's case (a) molecules, both electric and magnetic dipole moments are coupled to the internuclear axis. In this section, we are going to use OH ($X^2\Pi_{3/2}$) as a representative of Hund's case (a) molecules to describe the electric-field-enhanced spin-flip loss in a quadrupole magnetic trap.

3.1.1 OH Stark-Zeeman Energy Structure

Once we have a 60 mK trapped OH sample as discussed in Chapter 2, the first thing which comes to our mind is to apply an external electric field to polarize the molecules and study dipolar interaction between OH. Thus, it is very important to know all the field distribution beforehand. Fig. 3.1 (a) shows the magnetic and electric field distribution inside our quadrupole magnetic trap. A nearly uniform electric field (3 kV/cm) is generated by applying a voltage difference across the front and rear magnets. The angle θ_{EB} between electric and magnetic fields varies over the whole trap.

After solving the 8-state non-hyperfine ground-state Hamiltonian of OH (see Ref. [57]), the Stark-Zeeman energy of OH's doubly stretched states (m_j=$\pm$3/2) of $X^2\Pi_{3/2}$ are shown in Fig. 3.1 (b-c). The OH Stark-Zeeman structures show clear θ_{EB} dependence. As $\vec{E} \parallel \vec{B}$, the Stark shift only displaces the Zeeman structure without disturbing the linear Zeeman behavior. However, as $\vec{E} \perp \vec{B}$, the Zeeman shift becomes quadratic and two states nearly degenerate with each other for a much wider distance. The quadratic behavior can be understood from an intuitive picture. Once $\vec{E} \perp \vec{B}$, the total Stark-Zeeman energy can be expressed as a vector sum of all the contributions from both Stark and Zeeman components—$\sqrt{(\mu_E E)^2 + (\mu_B B)^2}$. Near the trap center, since Stark energy is much larger than Zeeman energy, the total energy can be simplified as $\mu_E E + \frac{(\mu_B B)^2}{2\mu_E E}$ after Taylor expansion, which is consistent with the quadratic behavior.

3.1.2 Enhanced Spin-flip Loss in a Magnetic Trap

Ref. [58] shows clear experimental evidence of electric-field-enhanced loss. An analytical form calculated from Landau-Zener formula is also given to estimate a fraction of the loss that can be attributed to electric-field-enhanced spin-flip mechanism. At the beginning of this section, we are going to give a more intuitive picture to explain how the spin-flip loss is enhanced for doubly dipolar molecules with mixed magnetic and electric fields applied.

Fig. 3.2(a) is used to describe the orientation of low-field-seeking state of OH with respect to

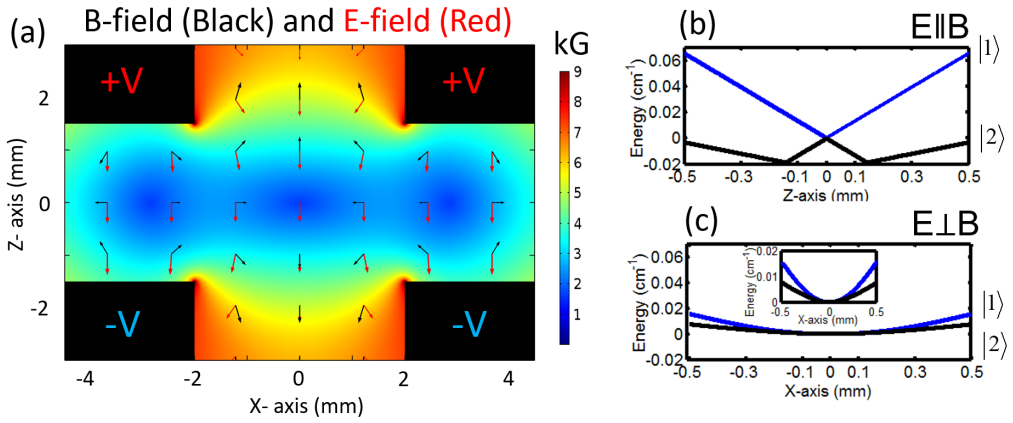

Figure 3.1: (a) A slice of magnetic field contour of the 3D quadrupole magnetic trap. The trap is formed by a pair of ring magnets. The magnetic field is represented by black arrows. A nearly uniform electric field (3 kV/cm) is generated by applying different polarities of voltages on the front and rear magnets, which are represented by the black rectangles. The electric field is represented by red arrows. (b) The Stark-Zeeman energy of OH's doubly stretched states of $X^2\Pi_{3/2}$ as $\vec{E} \parallel \vec{B}$. The state we are interested in is colored blue. (c) The Stark-Zeeman energy of OH's doubly stretched states of $X^2\Pi_{3/2}$ as $\vec{E} \perp \vec{B}$.

magnetic field. The dumbbell structure represents OH molecule. Once the red side of the molecule points to similar direction of the magnetic field, it means that OH is in low-field-seeking state.

Fig. 3.2(b) shows the orientation of OH inside a magnetic trap as molecule adiabatically propagates along Z-axis without electric field applied. Once the Larmor frequency is large enough, OH can adiabatically follow the variation of magnetic field which is colored by purple and stay in the low-field-seeking state, even though the magnetic field completely swaps the orientation through Z=0 mm plane.

However, once nearly uniform 3 kV/cm electric field is applied (see Fig. 3.2(c)), the fact that OH has dual dipole moment will cause OH to adiabatically follow a new quantization axis, instead of magnetic field. According to Hund's case (x) [59], the direction of the new quantization axis is determined by the vector sum of both electric and magnetic field contributions—$d\vec{E} + \mu\vec{B}$, which is colored by green. Since the new combined quantization axis and magnetic field start to point to opposite direction once OH passes through the Z=0 mm plane, relative to the reversely oriented magnetic field, OH flips to a high-field-seeking state and becomes anti-trapped.

Fig. 3.2(d) shows the orientation of OH inside a magnetic trap as molecule travels along X-axis with (3 kV/cm) electric field applied. With the presence of electric field, OH still adiabatically follow the variation of the combined quantization axis. However, since the orientation of the combined quantization axis experienced by OH varies in a very similar manner as magnetic field does along X-axis, OH still behave low-field-seeking with respect to magnetic field as molecule crosses X=0 mm plane. Then, there will be no electric-field-enhanced loss as OH travels along X-axis. Overall, the spin-flip loss is only enhanced by the electric field as molecule propagates through the plane where electric and magnetic field are orthogonal to each other.

The spin-flip loss estimation calculated in Ref. [58] cannot explain our observed loss rate. However, after more careful derivation, we realize the formula in [58] underestimates the loss by factor of three. Since the loss plane happens at Z=0 mm, a more accurate formula can be derived in cylindrical coordinates where only the velocity component along the Z-axis is taken into account.

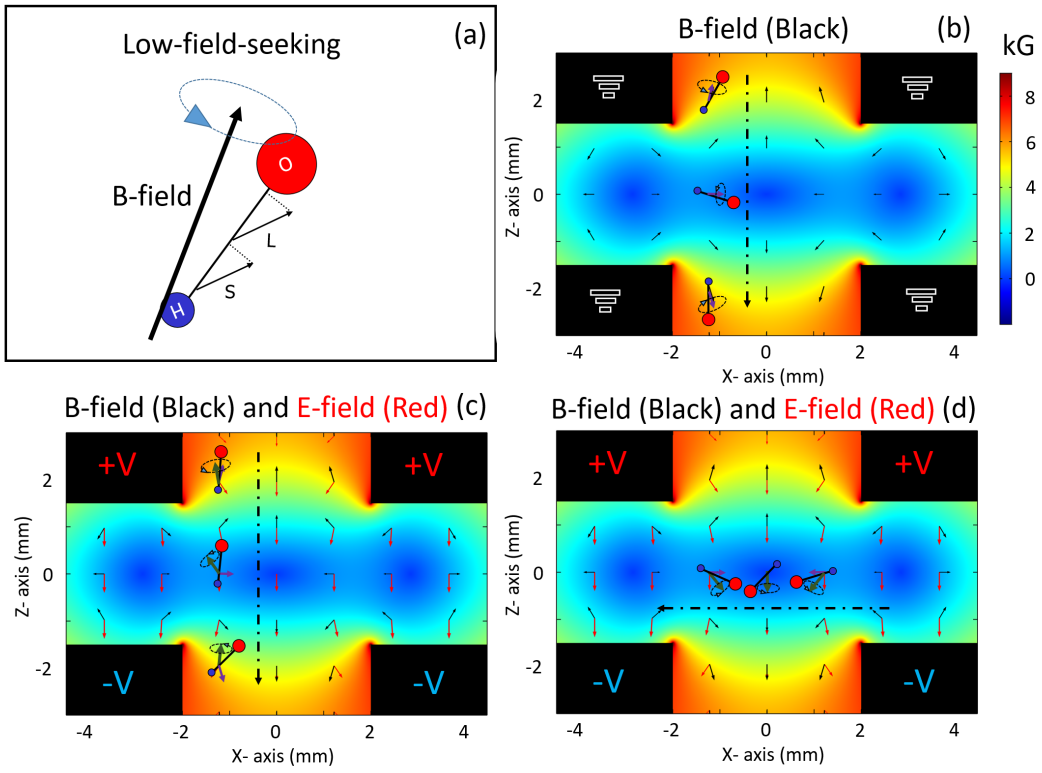

Figure 3.2: (a) A cartoon to describe the orientation of low-field-seeking state of OH with respect to magnetic field. The dumbbell structure respresents OH molecule. If the red ball side of molecule (angular momentum orientation) points to a similar direction of magnetic field, it means that OH is in low-field-seeking state. (b) The orientation of OH inside a magnetic trap as molecule travels along Z-axis without electric field applied. If the Larmor frequency is large enough, OH can adiabatically follow the variation of magnetic field colored by purple and remain in low-field-seeking state. The magnets are grounded to avoid any stray electric field. (c) The orientation of OH inside a magnetic trap as molecule travels along Z-axis with (3 kV/cm) electric field applied. According to Hund's case (x), OH will precess along the new combined quantization axis ($d\vec{E} + \mu\vec{B}$). Once OH crosses the Z=0 mm plane, the combined quantization axis which is colored by green and the magnetic field start to point to opposite directions. Thus, OH swaps to a high-field-seeking state relative to the magnetic field and gets lost from the trap. (d) The orientation of OH inside a magnetic trap as molecule travels along X-axis with (3 kV/cm) electric field applied. The combined quantization axis varies in a similar manner as magnetic field does, which keeps OH in low-field-seeking state relative to magnetic field. The purple arrow represents the magnetic field (b-d). The black dash-dot line represents OH propagating direction (b-d). The green arrow represents the combined quantization axis (c-d).

Then, the analytical formula used to calculate spin-flip loss rate can be expressed as:

$$\gamma = \int_0^\infty 2\pi r\, n(r) dr \int_0^\infty n(v_z) dv_z \left(v_z P_{\mathrm{LZ}}(r, v_z)\right), \tag{3.1}$$

where $P_{\mathrm{LZ}} = e^{-2\pi \frac{(\delta/2)^2}{\hbar dG/dz \cdot v_z}}$, v_z is the speed of OH along Z-axis, dG/dz is the derivative of the energy difference between two closest states (note that for this case, i.e., movement along the Z-axis, E is parallel to B), δ is the smallest energy gap between the two closest states, $n(r)$ is the Boltzmann distribution of population, and $n(v_z)$ is the Boltzmann distribution of velocity.

Electric field is required to open avoided crossings during evaporation and spectroscopy or to polarize the molecules during collision studies [49, 58]. For this reason we list loss rates relevant to applied electric fields of various magnitudes in Table 3.1. The calculation suggests the electric-field-enhanced loss can become very significant once the sample is cooled down to 5 mK. It is very important to be able to suppress the loss completely for further evaporation progress.

Table 3.1: Spin-flip loss rates (γ) of OH with different applied fields.

E (V/cm)	$\gamma\,(s^{-1})$ (55 mK)	$\gamma\,(s^{-1})$ (5 mK)	purpose
0	0.02	1.3	Zero Field
300	0.1	11	Evaporation
550	0.3	50	Spectroscopy
3000	19	2000	Polarizing

We can also incorporate the spin-flip loss into a Monte Carlo simulation, which is built from Direct Simulation Monte Carlo (DSMC) method [60] developed by G. A. Bird. Fig. 3.3 shows the comparison between experimental data on electric-field-enhanced loss and simulation including spin-flip loss. The reasonably good fit suggests most of the electric-field-enhanced loss can be explained by the spin-flip loss. However, the discrepancies between experiment and simulation may be attributed to two-body effects and left to be figured out in future.

In order to overcome the electric-field-enhanced spin-flip loss, we developed a new hybrid trap, which incorporates a pair of 2D quadrupole traps, one magnetic and the other electric. By adding a uniform magnetic field along the centerline of the 2D magnetic quadrupole, the zero

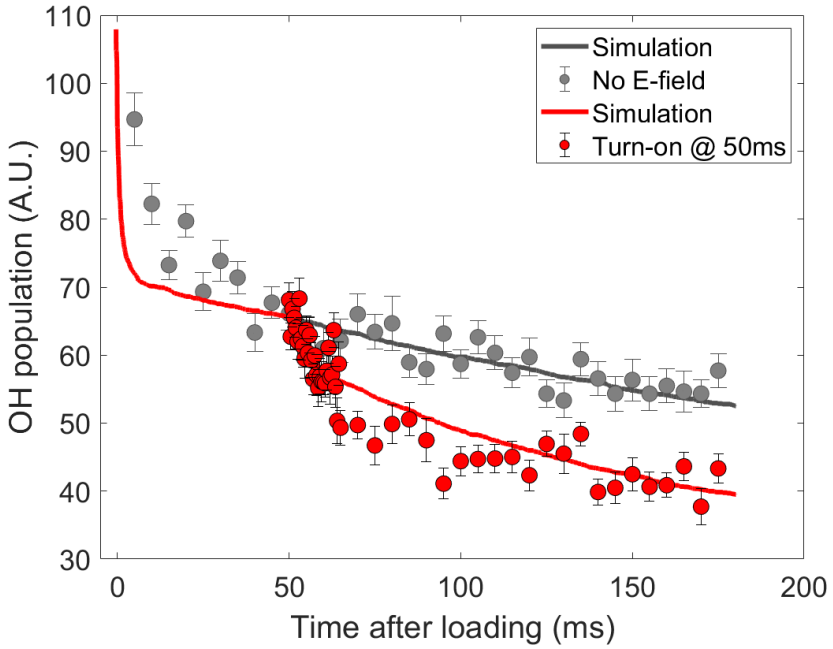

Figure 3.3: A comparison between experiment and simulation on electric-field-enhanced spin-flip loss. The circular dots represent experimental data. The solid line is from Monte Carlo simulation with only one free parameter for amplitude scaling. The grey color means there is no electric field applied. The red color means 3 kV/cm electric field is applied at 50 ms after loading. The reasonably good fit suggests most of the electric-field-enhanced loss can be explained by the spin-flip loss. However, we do notice that the experimental decays are in general slower than the spin-flip loss predictions at the beginning, which suggests some two-body effects left.

magnetic field region can be completely removed so as to suppress the spin-flip loss. More details of the hybrid trap can be found in Ref. [52].

3.2 Hund's Case (b) Molecules

Unlike Hund's case (a), only molecules whose spin-rotation coupling is much stronger than the spin-orbit coupling are considered as Hund's case (b) molecules. So far most of the ground electronic state of laser-cooled molecules belong to Hund's case (b). Moreover, all of these laser-cooled molecules have both electric and magnetic dipole moments. Thus, it is very important to understand the spin-flip loss mechanism for Hund's case (b) molecules. In the rest of this section, we are going to take $X^2\Sigma$, $G = 1$, $N = 1$ states of YO as an example to study its spin-dynamic behavior in mixed electric and magnetic fields.

3.2.1 YO Stark Shift and Zeeman Shift

All the relevant quantum numbers are defined here as a reference:

N, Nuclear rotational angular momentum.

S, Total spin of electrons.

I, Total spin of nucleus.

G, Vector sum of I and S.

F, Total angular momentum—vector sum of N and G.

m_A, Projection of some angular momentum (A) along the quantization axis.

The Zeeman structure of the $X^2\Sigma$, $G = 1$, $N = 1$ states of YO are shown in Fig. 3.4. The details of the YO structures can be found in Mark Yeo's thesis [55], chapter 2. As the magnetic field increases from 0 to 10 Gauss, there is a clear Paschen-Back effect due to the decoupling of spin and rotation. This makes sense given that the spin-rotation constant is only 10 MHz, corresponding

to 7 Gauss. Accordingly, the quantum basis switches from $|(N(SIG)Fm_F\rangle$ to $|(N(SIG)m_Nm_G\rangle$. The quantum-basis-transition is the key to understanding the electric-field-enhanced spin-flip loss for Hund's case (b) molecules.

The Stark shift of the $X^2\Sigma$, $G = 1$, $N = 1$ states of YO are shown in Fig. 3.5. In a similar way to the quantum-basis-transition within magnetic field, once the Stark energy is comparable to the energy of the spin-rotation coupling constant, F and m_F are not good quantum numbers anymore. Then, the Stark structures split into two branches, which correspond to states $m_N = 0$ and states $m_N = \pm 1$.

It is important to understand how the effective dipole moment of YO varies according to the strength of applied DC electric field in the lab frame, see Fig. 3.6. For the $m_N = \pm 1$ states, the effective dipole moment keeps increasing monotonically up to 2 Debye with a positive sign. Since $m_N = \pm 1$ states can only be coupled to the excited rotational states by DC electric field, they behave as high-field-seeking states in accordance with the positive sign of the effective dipole moment. For $m_N = 0$ states, since they can be coupled to both upper ($N = 2$) and lower ($N = 0$) states, the orientation of the YO dipole in the lab frame becomes highly electric-field dependent. As the Stark shift energy becomes smaller than the energy of the rotational constant, $m_N = 0$ states behave as low-field-seeking states since $N = 1$, $m_N = 0$ states are more strongly coupled to lower N=0, $m_N = 0$ states. Once the Stark shift energy is comparable to the energy of the rotational constant, the coupling strength between $N = 1$, $m_N = 0$ states and upper rotational states $N = 2$, $m_N = 0$ starts to become significant. Then, the strength of the effective dipole moment in the lab frame begins to decrease and the molecule reorients itself with respect to the direction of DC electric field. With a large enough electric field, the N=1, m_N=0 states evolve to high-field-seeking states. With 10 kV/cm electric field applied, which is easy to realize in the laboratory, the effective dipole moment reaches 1 Debye and the molecules are still in low-field-seeking states with respect to electric field. Thus, 10 kV/cm electric field can be used to study the long range dipole-dipole interaction.

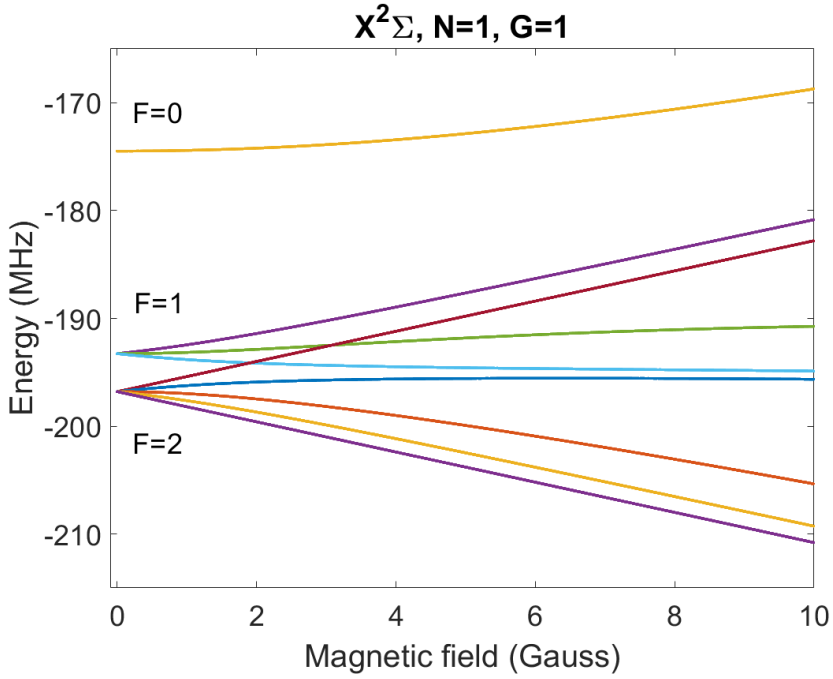

Figure 3.4: The Zeeman shift of $X^2\Sigma$, $G = 1$, $N = 1$ states of YO. Zero energy corresponds to the relevant $N = 1$ energy which is higher than the absolute ground state by $2B$, where B is the rotational constant. There is no electric field applied.

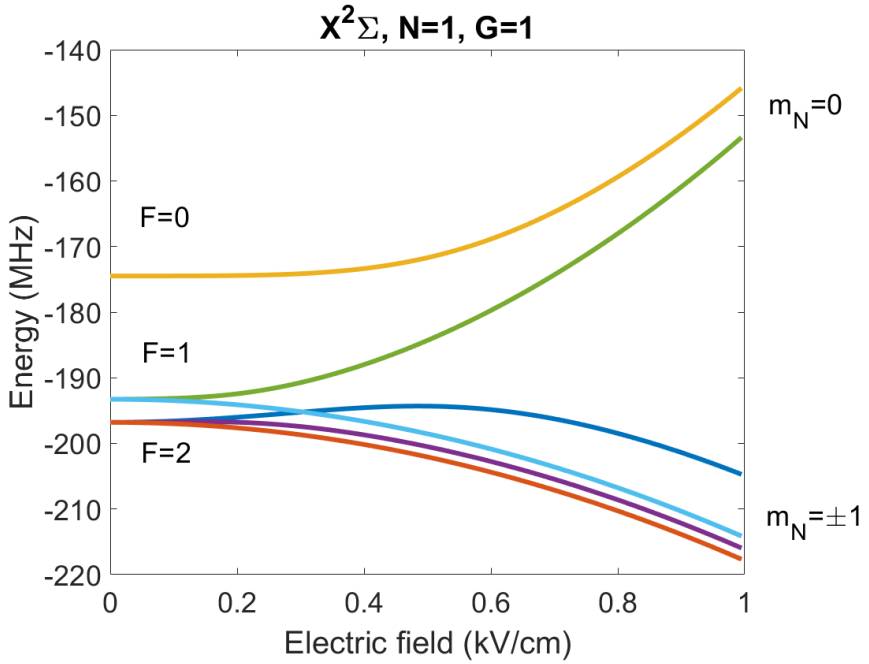

Figure 3.5: The Stark shift of $X^2\Sigma$, $G = 1$, $N = 1$ states of YO. Zero energy corresponds to the relevant $N = 1$ energy which is higher than the absolute ground state by $2 \cdot B$, where B is the rotational constant. There is no magnetic field applied.

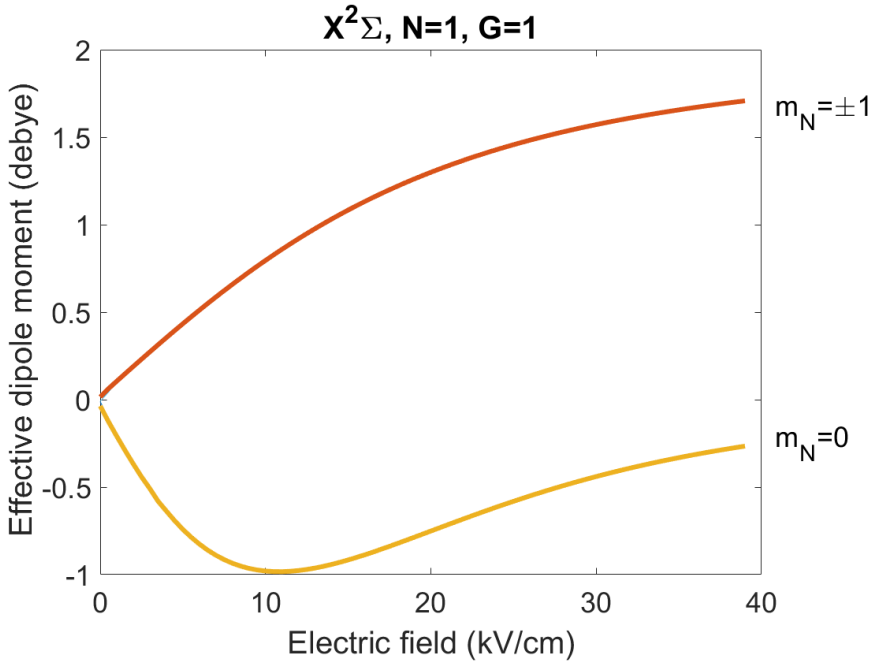

Figure 3.6: The effective dipole moment of $X^2\Sigma$,$G = 1$,$N = 1$ states of YO.

3.2.2 YO Stark-Zeeman Shift and Spin-flip Loss

In order to study the dipole-dipole interaction and even explore the possibility of evaporative cooling [61], it is very important to load the dipolar molecules into a trap and polarize them with either a DC electric field or MW (microwave). It has been demonstrated that laser-cooled molecules can be loaded into an optical dipole trap [62]. For atoms, the optical dipole trap has become a common tool to address the spin-flip loss problem. However, the optical trap has its own problems of not only heating the samples but also dissipating molecules. Thus, the magnetic quadrupole trap, which offers a long lifetime and no extra heating, can still be crucial to exploiting properties of ultracold molecules. Moreover, the internal states of molecules can be better controlled in a magnetic trap for collision study of selected quantum-state. In the next part we are going to study the spin dynamic behavior of YO with both magnetic and electric fields (such as 1 kV/cm) applied.

Fig. 3.7 shows the Stark-Zeeman shift of YO at different θ_{EB} (the angle between electric and magnetic fields). The range of magnetic field is chosen from 0 Gauss to 300 Gauss, the relevant energy scale for the 4 mK (65 Gauss) temperature of trapped YO so far obtained in a MOT [25]. Unlike the angle dependent Stark-Zeeman structure of OH, there is almost no θ_{EB} dependence. The different θ_{EB} dependence behaviors of Stark-Zeeman structure between OH and YO can be attributed to different coupling mechanisms for the different Hund's cases.

For Hund's case (b) molecules such as YO, since they do not have an orbital angular momentum, their magnetic dipole moment is fully determined by the spin of electron S. Meanwhile, the effective electric dipole moment in the lab frame is determined by rotation of the nuclear frame N. Once the magnetic field is strong enough to break the spin-rotation coupling, the quantum basis switches from $|(N(SIG)Fm_F\rangle$ to $|(N(SIG)m_N m_G\rangle$ [1] . Thereafter, the magnetic and electric dipole moments are decoupled and can align with their respective fields without conflict. Thus, there will be no electric-field-enhanced spin-flip loss for YO in the mK temperature regime.

However, if the trapped YO sample becomes so cold that the trapping magnetic field is not

[1] The magnetic fields under consideration in this section are not strong enough to break the $\approx$ 700 MHz Fermi-contact interaction so that G is still a good quantum number.

large enough to break the spin-rotation coupling anymore, the two dipole moments can still couple to each other, leading to a θ_{EB} dependent Stark-Zeeman shift. The angle dependent Stark-Zeeman shift is the key feature of electric-field-enhanced spin-flip loss as explained in the previous section.

Fig. 3.8 shows Stark-Zeeman structures of YO from 0 Gauss to 10 Gauss at three different θ_{EB}. The magnetic field range is chosen in order to match YO's Doppler cooling limit (hundreds of μK). Most of the states don't have a complete confinement in 3D except for one state colored by blue. We call the useful state for trapping "magic state". The magic state does not have any avoided crossing within 10 Gauss magnetic field range, which can greatly suppress the diabatic dynamics of magnetically trapped molecules observed for the OH e-state [54]. Moreover, since the magic state is not degenerate with any other states at zero magnetic field, there is not only no enhanced spin-flip loss, but the traditional spin-flip loss is also suppressed without the necessity of building any fancy trap. Because the magic state is at least 10 MHz (500 μK) away from any other nearby states at zero magnetic field, it is possible that inelastic collisions are also significantly suppressed in this state. Thus, the magic state may be another candidate state for further elastic collision study or even evaporation cooling.

3.2.3 Properties of the Magic State

Here we discuss several further aspects of the magic state that has just been introduced.

3.2.3.1 Reasons for Existence of the Magic State

The quadratic Zeeman shift feature of the magic state near zero Gauss suggests the existence of the magic state is due to the initiation of an avoided crossing when DC electric field causes the quantum basis transition from $|(N(SIG)Fm_F\rangle$ to $|(N(SIG)m_N m_G\rangle$. There are two important terms—spin-rotation coupling and the dipolar hyperfine interaction [2] , which can couple different states and open the avoided crossing. In order to confirm our suspicions, these terms can be removed artificially one by one in the Hamiltonian calculation. As shown in Fig. 3.9, all the terms

[2] The dipolar hyperfine interaction is the magnetic dipolar interaction between the nuclear spin and electron spin.

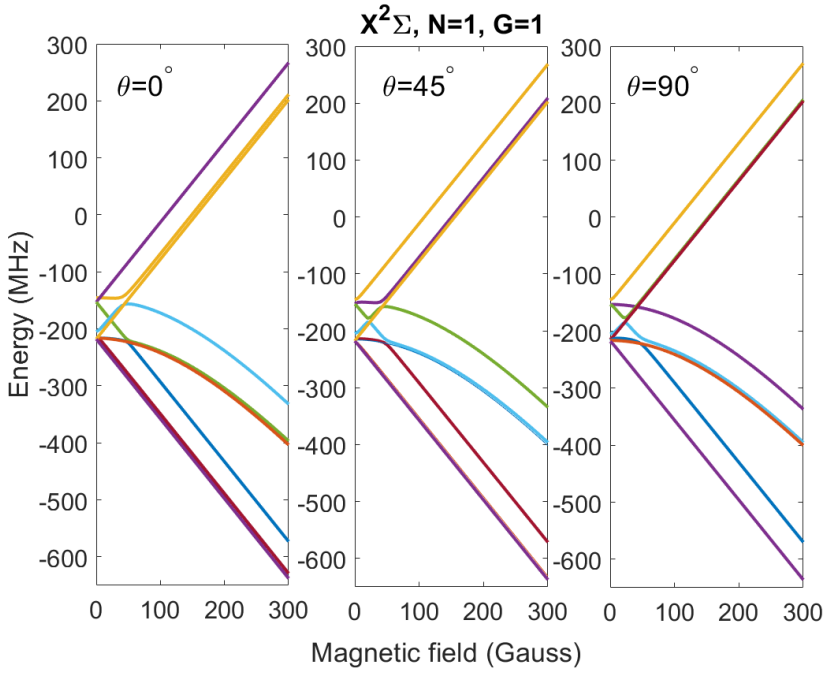

Figure 3.7: The Stark-Zeeman shift of YO at different θ_{EB} (the angle between electric and magnetic fields). The strength of applied electric field is 1 kV/cm. Panels (a-c) correspond to θ_{EB} of 0°, 45° and 90°, respectively.

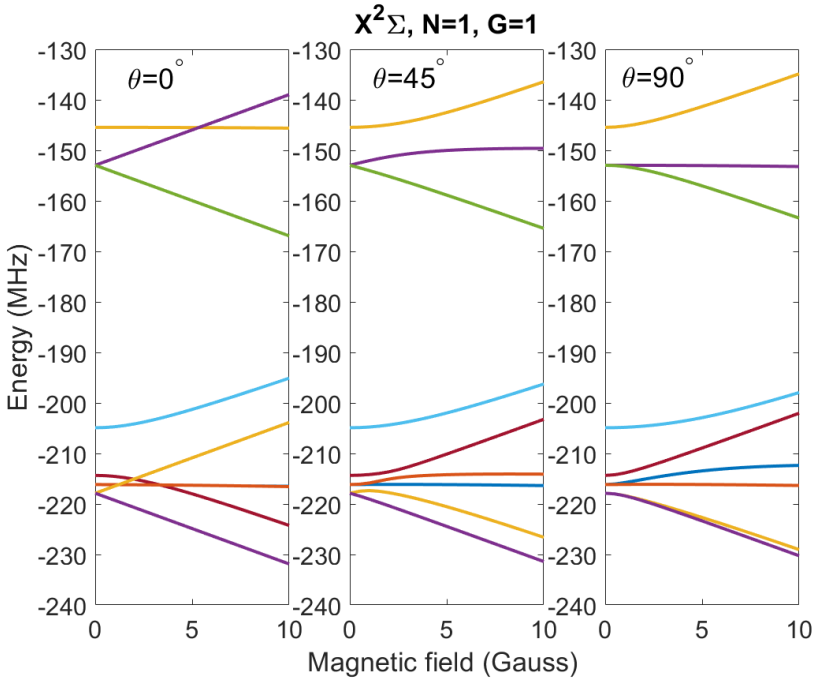

Figure 3.8: The stark-zeeman shift of YO at different θ_{EB}. The applied electric field is 1 kV/cm. Panels (a-c) correspond to θ_{EB} of 0°, 45° and 90°, respectively.

of Hamiltonian are included in the three panels except for the optional dipolar interaction and spin-rotation. It is clear that dipolar interaction is the key to explain the appearance of the magic state. We also attempt to explain the appearance of the magic state with a more intuitive picture.

When there are no external fields applied, the total angular momentum F does not have any favorable orientation in the lab frame. Thus, all the states with the same F become degenerate. However, once the Stark shift is comparable to the strength of the spin-rotation coupling, the nuclear frame of YO will stop rotating and the electric dipole moment will have a certain orientation with respect to the electric field according to its rotational quantum projection m_N. Thus, the spin-rotation coupling breaks down and the quantum basis evolves from $|N(SI)GFm_F\rangle$ to $|N(SI)Gm_Nm_G\rangle$. Since the applied electric field cannot break time reversal symmetry, without a magnetic coupling, the state pairs such as $m_N = 1$,$m_G = -1$ and $m_N = -1$,$m_G = +1$ are still degenerate at zero Gauss as shown in the right panel of Fig. 3.9. However, the existence of the dipolar interaction can satisfy the demand of requiring magnetic coupling to break the degeneracy. In more details, the dipolar interaction can be decomposed into a term proportional to $G^{2+}N^{2-} + G^{2-}N^{2+}$ [48] so as to couple the off-diagonal terms in the basis $|N(SI)GFm_Nm_G\rangle$ and open the avoided crossing. Since the dipolar interaction is an internal interaction between particles, it can only couple the states with identical projection of total angular momentum along the quantization axis, such as the state pair $m_N = +1$, $m_G = -1$ and $m_N = -1$, $m_G = +1$, of which the $m_N = -1$, $m_G = +1$ state is the "magic state" from above. For the state pair $m_N = +1$, $m_G = +1$ and $m_N = -1$, $m_G = -1$, since their total angular momentum projections are not the same, they are still degenerate at zero Gauss as shown in the left or middle panel of Fig. 3.9.

3.2.3.2 Favorability of the Magic State for Trapping

In order to maintain a large density after loading, a reasonably steep trap is required. Table 3.2 shows a comparison of effective trap gradient between Rb in a quadrupole-Ioffe-configuration trap (QUIC trap) [63] and YO in a 3D magnetic quadruple trap. The very similar trap gradient suggests that the magic state is indeed a good trapping state to be able to maintain a large density

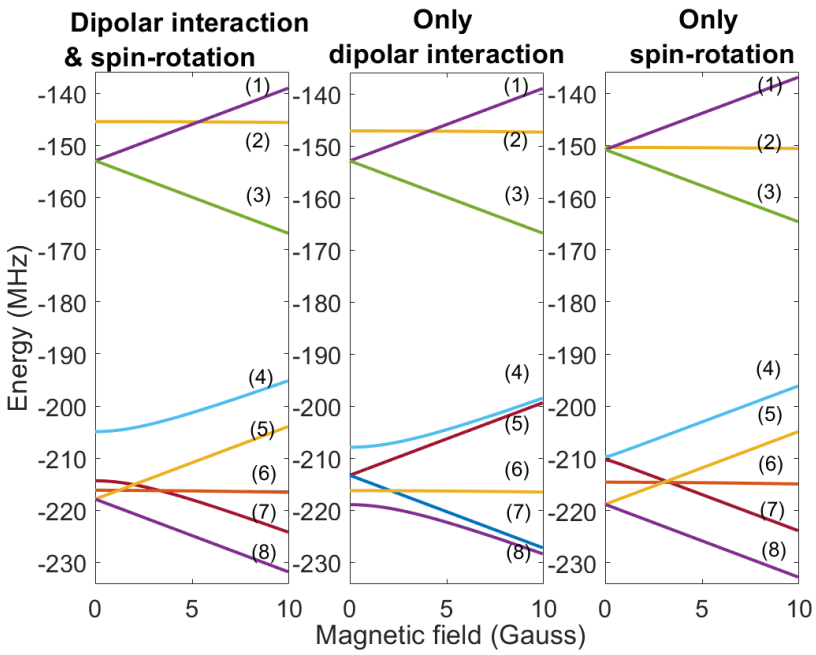

Figure 3.9: The Stark-Zeeman shift with different Hamiltonian terms excluded. For all the panels, all the Hamiltonian terms are contained except for optional spin-rotation coupling and dipolar interaction. The left panels include both spin-rotation coupling and dipolar interaction. The middle panel includes only dipolar interaction; the right panel includes only spin-rotation coupling. 1 kV/cm electric field is applied for all the panels with $\theta_{EB} = 0^\circ$. Different number represents different quantum state: (1) $m_G = 1$, $m_N = 0$; (2) $m_G = 0$, $m_N = 0$; (3) $m_G = -1$, $m_N = 0$; (4) $m_G = 1$, $m_N = -1$; (5) $m_G = 1$, $m_N = 1$; (6) $m_G = 0$, $m_N = \pm 1$; (7) $m_G = -1$, $m_N = -1$; (8) $m_G = -1$, $m_N = 1$;

for further collision studies.

Table 3.2: A comparison of effective trap gradient between YO and Rb.

	YO	Rb
The gradient of magnetic trap	30 G/cm	300 G/cm^2
Magnetic dipole moment	0.4 MHz/G^2	1.4 MHz/G
Effective trap gradient	360 MHz/cm^2	420 MHz/cm^2

3.2.3.3 Loading Molecules into the Magic State

Through adiabatically sweeping electric or magnetic fields in order, there are two possible schemes of loading YO into the magic state after an AC MOT.

Fig. 3.10 shows the first scheme of loading YO into the magic state. Once YO is captured by the AC MOT, the AC magnetic field is turned off adiabatically. Then, a uniform DC electric field of 1 kV/cm is switched on without any bias magnetic field. Next, a 3D quadrupole magnetic trap is activated. Finally, the molecules with initial state $F = 2$, $m_F = 0$ are loaded into the magic state.

Fig. 3.11 shows a second scheme of loading YO into the magic state. Similar to scheme one, the AC magnetic field is first switched off adiabatically. Then, a uniform magnetic field is applied up to 1 Gauss[3] . Next, apply a uniform 1 kV/cm DC electric field. Finally, switch the uniform magnetic field off and turn on a 3D quadrupole magnetic trap and the molecules with initial state $F = 1$, $m_F = 0$ can be loaded into the magic state.

Certainly, the loading efficiency of these two schemes will be not too high without any pre-state preparation, since after AC MOT the population is distributed over all the initial states. However, it has been demonstrated that by combining optical pumping and MW transferring, the population of dipolar molecules (CaF) can be transferred to a specific quantum state with really high efficiency within the ms timescale [64]. Moreover, once the temperature of YO is below 1 mK,

[3] It has been confirmed that once the magnetic field is 1 Gauss or above, the conclusion is same.

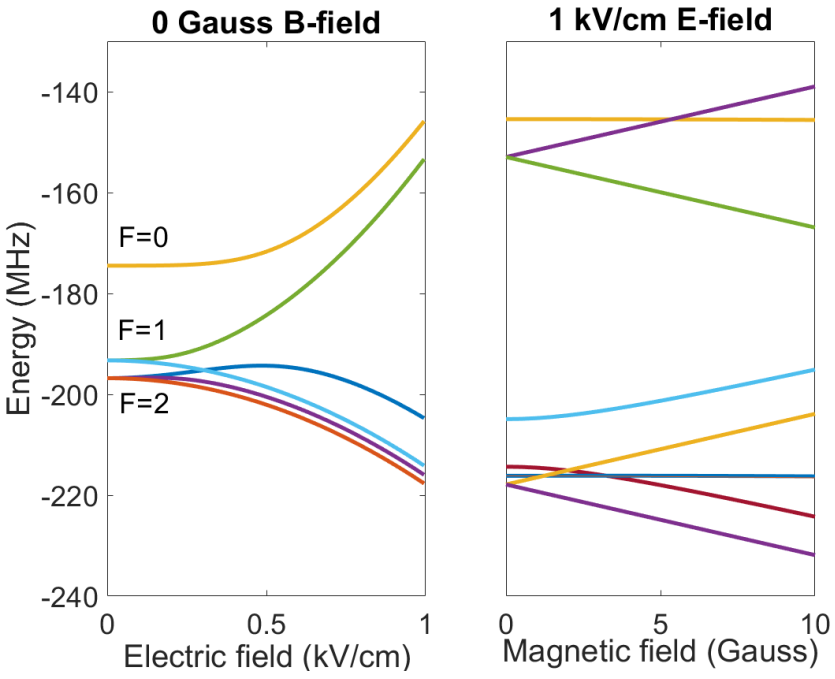

Figure 3.10: The first sequence of loading YO into the magic state after AC MOT. First sweep the electric field up to 1 kV/cm without any bias magnetic field as shown in the left panel. Then, turn on the quadrupole magnetic field with a uniform 1 kV/cm electric field at 0° θ_{EB} as shown in the right panel. The molecules with initial state $F = 2$, $m_F = 0$ can be loaded into the magic state. The adiabatic dynamics are identical for all other θ_{EB}.

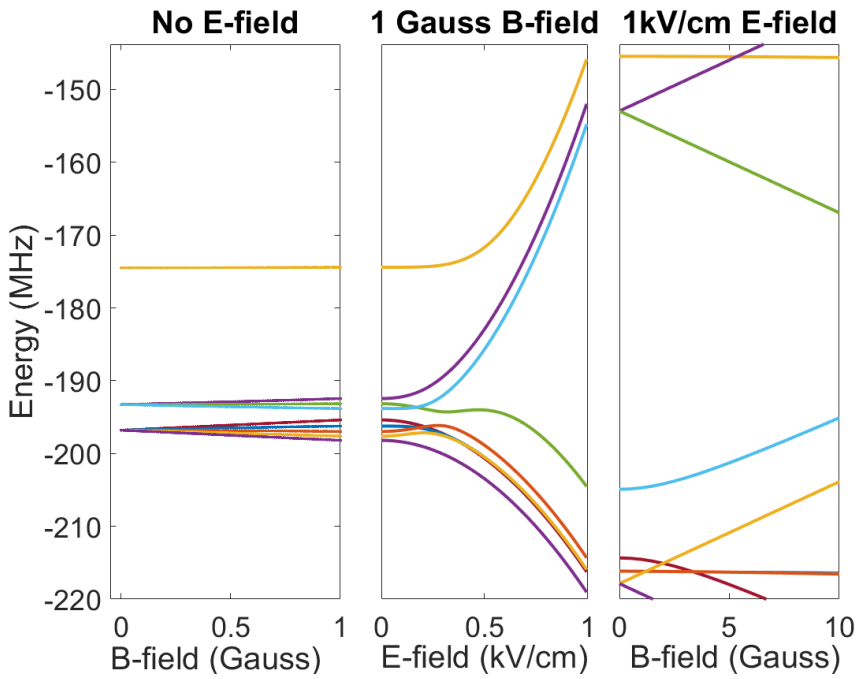

Figure 3.11: The second sequence of loading molecules into the magic state after AC MOT. First sweep the uniform magnetic field up to 1 Gauss without any bias electric field as shown in the left panel. Then, turn on a uniform electric field of 1 kV/cm at 0° θ_{EB} as shown in the middle panel. Lastly, switch the uniform magnetic field to a 3D quadrupole magnetic field with a uniform 1 kV/cm electric field applied as shown in the right panel. The molecules with initial state $F = 1$, $m_F = 0$ can be loaded into the magic state. The adiabatic dynamics are identical for all other θ_{EB}.

the thermal velocity becomes smaller than 1 m/s. Thus, 100 kHz slew rate of sweeping magnetic and electric fields should be small enough to avoid diabatic transition, but fast enough to keep the sample cold. Overall, it seems very promising to load most of YO population into the magic state for further studies.

Chapter 4

OH Density Calibration of Free Flight by H_2 Raman scattering

4.1 Motivation

Absolute density calibration is crucially important in quantifying exact cross sections between colliding partners, determining stimulated emission coefficient of excited states and so on. For our experiment, it is very instructive to know the exact density of OH so as to deduce guiding efficiency of our Stark decelerator and also assign a collision rate for OH evaporation. There have been many ways developed for density measurement, of which the most simple and common way is laser induced fluorescence (LIF). However, in order to figure out the exact density, many measurements and assumptions are required to be made, such as an accurate knowledge of solid angle of an LIF collection system, population distribution within a detection volume, exact values of all the quantum efficiencies and so on. All these complexities make the results of LIF density measurement untrustworthy. Other than LIF, there are other ways based on cavities such as absorption imaging and cavity ring-down. However, there are still no high finesse cavities working for OH UV electronic transition lines. Since mid-IR vibrational transition lines of OH overlap with water absorption lines, it is also hard to find a proper cavity for the OH vibration. Recently, it was demonstrated OH density can be calibrated with Resonance-enhanced multiphoton ionization (REMPI) in a molecular beam or an electrostatic trap[65, 66]. However, there is still some challenge of building a high harmonic optical source for REMPI. Meanwhile, an alternative is H_2 Raman scattering, which relies on comparison with the Q-branch of H_2 spectroscopy, can be used for density calibration [67]. Compared with other methods, the H_2 Raman scattering technique has advantages of very simple

setup and no specific requirement on the laser wavelength or power. Thus, we chose to use H_2 Raman scatttering to do OH density calibration.

4.2 Derivation of Formulas for OH Density Calibration Calculation

In our experiment, OH population is measured by LIF. By keeping an identical laser setup and photon collection system for both OH LIF and H_2 Raman scattering measurement, the values of photon collection efficiency and laser power can be canceled out between these two measurements. Then, without knowing laser power or photon collection efficiency accurately, we can still assign a trustworthy value for OH density.

We begin by building theoretical models for both OH LIF and H_2 Raman scattering so as to know which parameters are required to measure for OH density calibration.

4.2.1 A Theoretical Model for OH LIF

For OH LIF, we ignore fine/hyperfine structures for OH electronic transitions and simplify OH structure to a two-level system. Then, rate equations for the two-level system can be expressed as:

$$\begin{cases} \frac{dN_e}{dt} = -A_{21}N_e + B_{21} \cdot \int \rho(\nu)g(\nu)d\nu \cdot (N_g - N_e) \\ \frac{dN_g}{dt} = +A_{21}N_e - B_{21} \cdot \int \rho(\nu)g(\nu)d\nu \cdot (N_g - N_e) \end{cases} . \tag{4.1}$$

Here A_{21} is Einstein A coefficient for spontaneous emission, B_{21} is Einstein B coefficient for stimulated emission, N_e is population in the excited state, N_g is population in the ground state, $\rho(\nu)$ is energy of laser per volume at certain frequency, and $g(\nu)$ is the lineshape function of OH electronic transition.

Since the linewidth of our pulsed laser ($\propto$ GHz) is much larger than natural linewidth of OH transition ($\propto$ MHz), Eq. 4.1 can be simplified as:

$$\frac{dN_e}{dt} = B_{21} \cdot \int \rho(\nu)g(\nu)d\nu \cdot (N_g - N_e). \tag{4.2}$$

If we assume laser power is set in a linear regime (far from transition saturation) and there is only a small amount of population being excited, Eq. 4.2 can be further simplified as:

$$\begin{aligned}\Delta N_e &= B_{21} \cdot \int \frac{I(t)}{c\Delta\nu} dt \cdot N_g \cdot M \\ &= \frac{B_{21}}{c\Delta\nu} \cdot \int I(t) dt \cdot N_g \cdot M \\ &= \frac{B_{21}}{c\Delta\nu} \cdot \frac{E}{A} \cdot N_g \cdot M \\ &= \frac{B_{21}}{c\Delta\nu} \cdot \frac{E}{A} \cdot n_{OH} \cdot V \cdot M.\end{aligned} \tag{4.3}$$

Here A is area of laser beam, E is laser energy, n_{OH} is OH density, c is speed of light, V is detection volume, and M is a modification factor due to population excitation. If we consider all the quantum efficiency of photon collection, the total detected signal can be expressed as:

$$\begin{aligned}S_{OH} &= \eta_{OH} \frac{\eta \Omega' \Delta N_e}{4\pi} F(\nu = 1 \rightarrow \nu' = 1) \\ &= \frac{\eta B_{21}}{c\Delta\nu} \frac{E}{A} n_{OH} V \eta_{OH} \frac{\Omega'}{4\pi} F(\nu = 1 \rightarrow \nu' = 1) M.\end{aligned} \tag{4.4}$$

Here η_{OH} is transmission of filter arrays at 313 nm, the wavelength of OH emission; η includes all other quantum efficiency of photon collection, which show no discrepancy between 313 nm and 319 nm, the wavelength for Raman scattering; $F(\nu = 1 \rightarrow \nu' = 1)$ is the Franck-Condon coefficient of the OH emission line at 313 nm; and Ω' is the solid angle of the collection system.

4.2.2 A Theoretical Model for H_2 Raman Scattering

We start the derivation from Beer's law. The H_2 Raman scattering signal can be expressed as:

$$S_{H_2} = \eta_{H_2} \frac{\eta E V}{h\nu_{319} A} \frac{\partial\sigma}{\partial\Omega}(90^\circ) n_{H_2} \Omega', \tag{4.5}$$

where η_{H_2} is transmission of filter array at 319 nm, ν_{319} is light frequency at 319 nm, h is Planck's constant, n_{H_2} is the density of hydrogen at a certain pressure, and $\frac{\partial\sigma}{\partial\Omega}(90^\circ)$ is the maximal differential cross section of Raman scattering, which occurs when the polarization of the light is mutually orthogonal to the incoming and scattered radiation.

By combining Eq. 4.4 and Eq. 4.5, the formula of OH density can be expressed as:

$$n_{OH} = \frac{S_{OH}}{S_{H_2}} \frac{\eta_{H_2} 4\pi \frac{\partial \sigma}{\partial \Omega}(90^\circ) n_{H_2} \Delta \nu c}{\eta_{OH} B_{21} h \nu_{319} F(\nu = 1 \rightarrow \nu' = 1) M} \tag{4.6}$$

It is seen that OH density becomes independent of detection volume, solid angle and laser energy. Instead, we only need to measure OH/ Raman scattering signal, transmission of filter arrays and the line-width of laser.

4.3 Schematic of Experimental Setup

Besides the parameters listed above to be measured, there are several key points we need to pay attention to:

(1) Make sure OH density is uniform within a detection volume.

(2) Make sure laser power is set in a linear regime.

(3) Make sure using identical laser power and collection configuration for both LIF and Raman scattering measurement.

(4) Make sure having a clean polarization of incident laser so that it is easy to figure out angle dependent cross section of Raman scattering.

With all the key points in mind, the experimental setup is designed and arranged as shown in Fig. 4.1. The output wavelength of the laser system is set to drive the transition from the ground state $\left|X^2\Pi_{3/2}, J = 3/2, \nu = 0\right\rangle$ to the excited electronic state $\left|A^2\Sigma, N = 1, \nu' = 1\right\rangle$. The laser system consists of a frequency doubled Nd:YAG laser (Quanta Ray) as a pump laser and a tunable dye laser with Rhodamine 6G as a gain medium. Following the dye laser, there is a frequency-doubling cavity to convert the wavelength of the laser from 564 nm to 282 nm. Fig. 4.1 (a) shows a schematic of the experimental setup. In order to have a pure incident polarization, both a PBS (GLB10-UV) crystal and a $\lambda/2$ waveplate are used. The polarization of transmitted light is aligned along the Z-axis with an extinction ratio more than 10,000. The details related to polarization will be

discussed later. The other polarized light is monitored by a fast photodiode (Thorlabs DET10A) for the purpose of power normalization. A 90/10 beamsplitter is inserted into the laser path to pick up some light to measure both beam width and energy of the incident laser [1] . We are able to measure OH LIF signal and H_2 Raman scattering signal by either running a valve to produce an OH pulse or filling the chamber with a known pressure of H_2, respectively.

For our first trial, OH density calibration is done at the exit of a stark decelerator. Fig. 4.1 (b) shows the photon collection system. Two identical lenses (f=30 mm, diameter=25 mm) are used together to collect photon signal onto a PMT (Hamamatsu R3788). The wavelength of OH fluorescence photon is 313 nm and the wavelength of H_2 Raman scattering photon is 319 nm. Both wavelengths are far away from incident wavelength—282 nm. Thus, signal and background scattering can be well separated with a filter array, which is composed of a color filter and an interference filter. The color filter (UG11) is used to block both visible room light and red-shift scattering light from UV. The interference filter (Omega 313BP10) is used to suppress both background scattering photons and Rayleigh scattering from H_2 at 282 nm. As shown in Fig. 4.2, transmission of the filter array are measured from 270 nm to 800 nm by a spectrophotometer (Varian Cary 500, Keck Lab). Transmission at 313 nm–OH LIF transition line is 57%. Unlike LIF, numerous rotational Q branch stokes lines of H_2 Raman scattering are excited and have a total width approaching 50 cm^{-1}. Thanks to a small variation of transmission near 319 nm, 50 cm^{-1} only corresponds to 10% transmission variation. Thus, transmission at H_2 Raman scattering line can be represented by the mean value—29%. Transmission ratio of the filter array between 319 nm and 282 nm is more than 1000, which is large enough to rule out interference from Rayleigh scattering.

There is an adjustable optical slit placed in the imaging plane of the collection system, which is used to constrain the detection volume along the X-axis for optimum comparability between OH and H_2. All the photon signal is collected by a PMT, which is connected to a scope for a signal readout.

[1] The power listed below has been scaled back according to the beamsplitter.

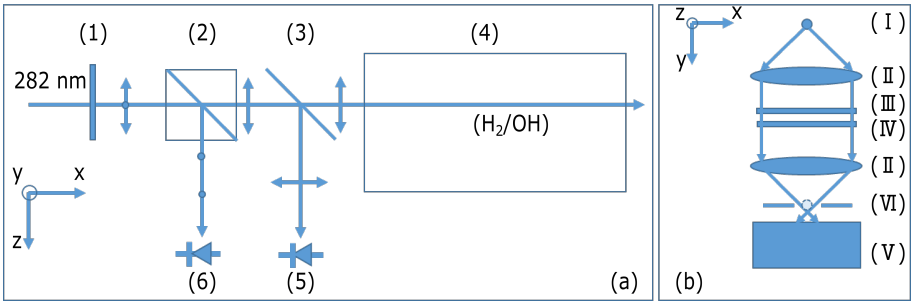

Figure 4.1: Schematics of OH density calibration by H_2 Raman scattering. (a) The diagram of the laser arrangement. (1) half waveplate, (2) polarization beam splitter (GLB10-UV), (3) 90/10 beam splitter, (4) science chamber filled with OH/H_2, (5) a powermeter, (6) a fast photodiode (DET10A). (b) The photon collection system. (i) the illuminated object, (ii) UV lens (f=30 mm, diameter=25 mm), (iii) a color filter (UG11), (iv) an interference filter (Omega 313BP10), (v) a PMT (Hamamatsu R3788), (vi) an adjustable optical slit

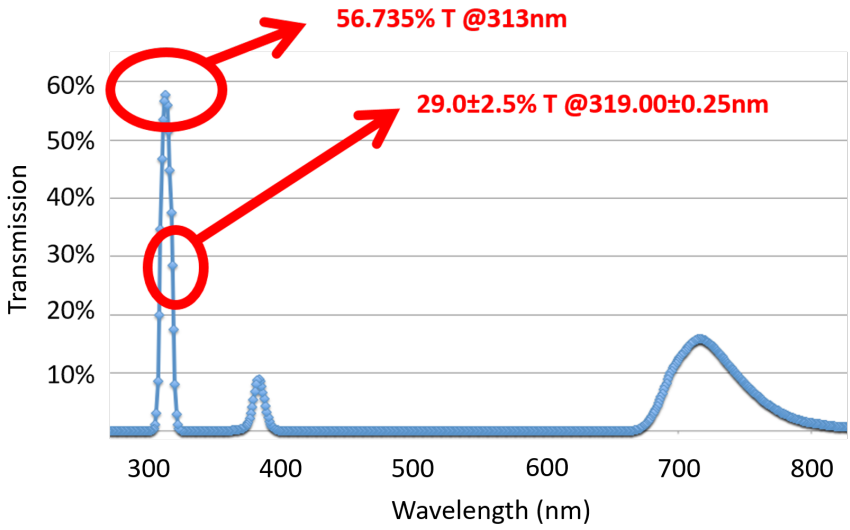

Figure 4.2: Transmission spectrum of the filter array of the collection system as shown in Fig. 4.1 (b).

4.4 LIF Measurement of OH

4.4.1 Relation between Laser Energy and OH LIF

Fig. 4.3 shows a relation between laser energy and OH LIF. The laser energy is controlled by tuning the relative angle between optical axis of the half waveplate and the PBS. By fitting the experimental data with the formula $A\frac{\frac{I}{I_0}}{1+\frac{I}{I_0}}$ [2] , saturation energy I_0 can be extracted and is equals to 38 μJ. 8 μJ is chosen as incident laser energy so as to safely maintain the linear relation between laser energy and OH LIF.

4.4.2 Uniformity of OH Density within the Detection Region

Unlike H_2, which can be uniformly filled inside the chamber with a leak valve, the OH beam has a finite size– 2 mm $\times$ 2 mm $\times$ 100 mm in X-Y-Z three dimensions. Thus, we need to constrain the detection volume small enough to have a nearly uniform OH filling. Since the detection volume is restricted by overlapping volume between spatial profile of laser, slit width in the imaging plane and detection volume of the photon collection system, we need to measure the field of view (FOV) and the depth of field (DOF) of the collection system as well as laser beam size.

4.4.2.1 FOV and DOF of the Collection System

Fig. 4.4 (a) shows the setup used to measure FOV and DOF of the photon collection system. In the setup, 564 nm light is coupled into a fiber and works as a point source. The fiber head is mounted on a 3-dimension translational stage. By translating the point source in each dimension, we can measure photon collection efficiency at each relative position, as shown in (b-d) of Fig. 4.4. DOF (FOV) is defined as the FWHM of the position-dependent collection efficiency. The differences of FOV between Y-axis and Z-axis are due to different length of the PMT area in these two dimensions. The smallest FOV of the photon collection system is 2.5 mm along the Y-axis, which is comparable to the molecular beam size.

[2] I_0 is saturation energy; A is scaling factor.

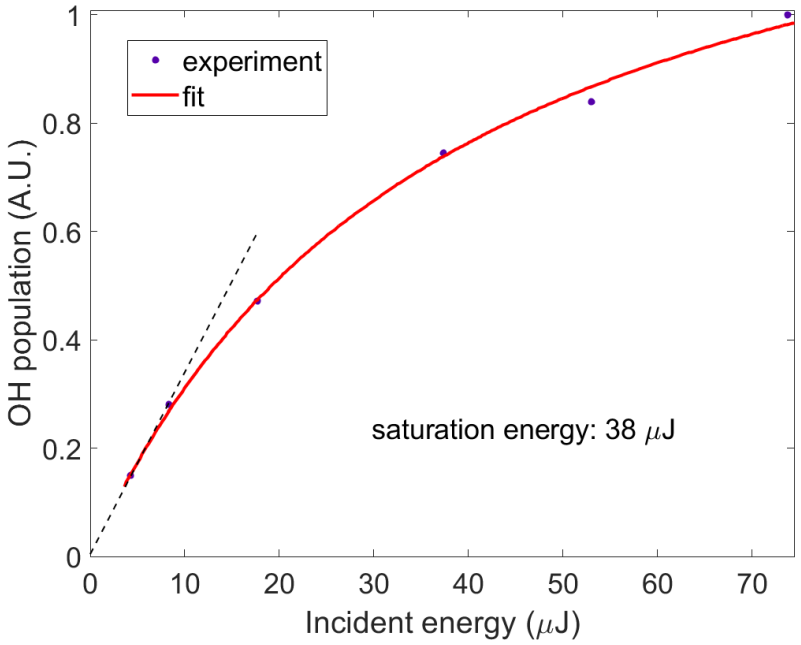

Figure 4.3: Saturation energy measurement of OH. The blue dots are experimental data. The red solid line is theoretical fitting with the formula $A\frac{\frac{I}{I_0}}{1+\frac{I}{I_0}}$. The fitted saturation energy is 38 μJ. 8 μJ is chosen as the incident laser energy so as to maintain the linear relation between laser energy and OH LIF.

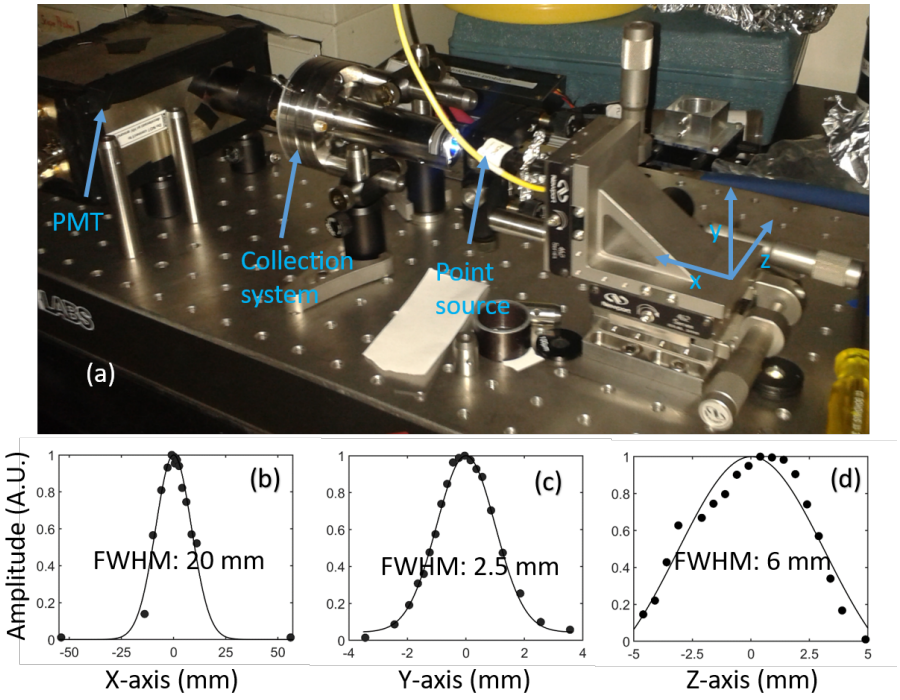

Figure 4.4: Measurement of FOV (field of view) and DOF (depth of field) of the photon collection system. The photon collection system is as same as shown in Fig. 4.1 (b). (a) schematic diagram. DOF (FOV) is defined as FWHM of position-dependent collection effciency (b-d). (b) DOF of the collection system along the X-axis with a 20 mm FWHM. (c) FOV of the collection system along Y-axis with a 2.5 mm FWHM. (d) FOV of the collection system along Z-axis with a 6 mm FWHM. Different FOV between Y-axis and Z-axis is due to different length of the PMT area in these two dimensions.

4.4.2.2 Beam Size of 282 nm Laser

By accurately translating a razor blade orthogonally across the laser beam in front of the power meter, we are able to measure the beam size of the incident laser. As shown in Fig. 4.5, the FWHM of the laser beam size[3] is 0.78 mm by fitting the experimental data with an error function (a*erf((x-b)/c)+d). Since the laser beam size is much smaller than both OH beam width and FOV (DOV) of the collection system, the detection area in the Y-Z plane is constrained by the laser beam profile.

4.4.2.3 Slit Width

An adjustable optical slit is placed in the imaging plane of the collection system to control the uniformity along the X-axis. Fig. 4.6 shows as the slit width keeps increasing, OH LIF transits from linear regime to saturation regime. The slit width is set to 0.75 mm to maintain the uniformity in X-dimension. The dash line is a guide to the eye.

4.4.3 Homogeneity of OH within the Detection Volume

The overall detection volume is constrained by intersection between the 0.78 mm diameter laser beam and the 0.75 mm wide slit in the imaging plane. In order to confirm the homogeneity of density, a second razor blade is placed between the beamsplitter and the PBS. By translating the razor blade across the laser beam along Y-axis, we are able to truncate incident beam so as to control the overlapping area between laser beam and OH beam. If the OH density is uniform, a linear relation should be expected, which is supported by Fig. 4.7. [4] Since the density homogeneity in X-axis has been confirmed by the slit in Fig. 4.6, a uniformly distributed density is achieved within the selected detection region. When the laser is completely unblocked, total OH LIF signal is 13.4 pVs within the constrained detection volume.

[3] Beam widths are same in two dimensions.
[4] We repeat the this procedure for Z-axis, which also shows nice linear relation.

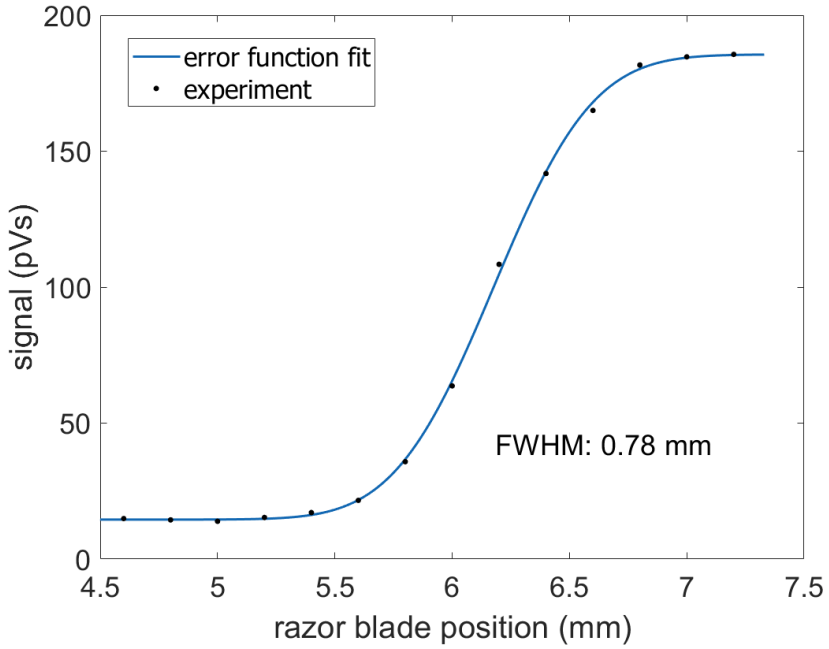

Figure 4.5: Measurement of laser beam size. By translating a razor blade orthogonally across the laser beam in front of the power meter, the laser beam size can be measured. The blue dot is experimental data. The blue solid line is a theoretical error function fit (a*erf((x-b)/c)+d). The FWHM of the measured beam size is 0.78 mm.

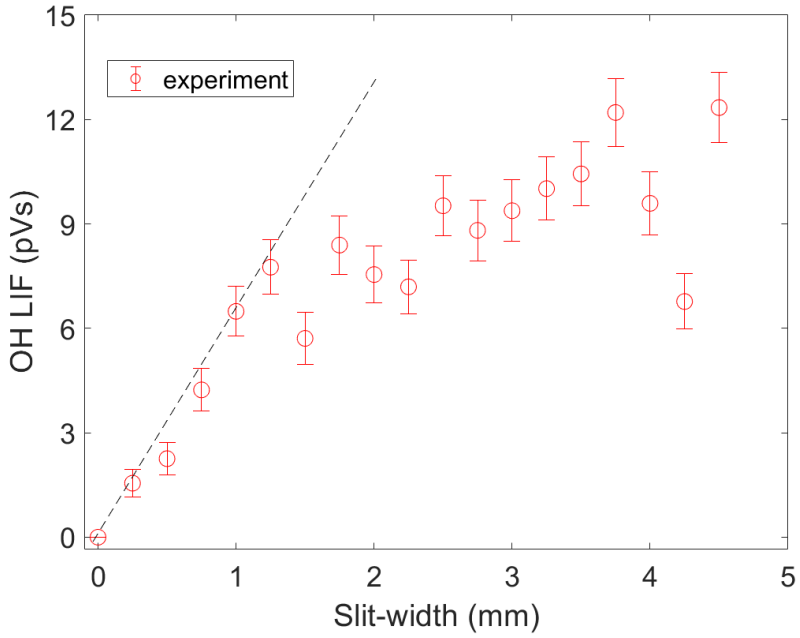

Figure 4.6: The relation between LIF and slit width. The slit width is set to 0.75 mm to maintain a uniform density along X-axis. The dashed line is a guide to the eye.

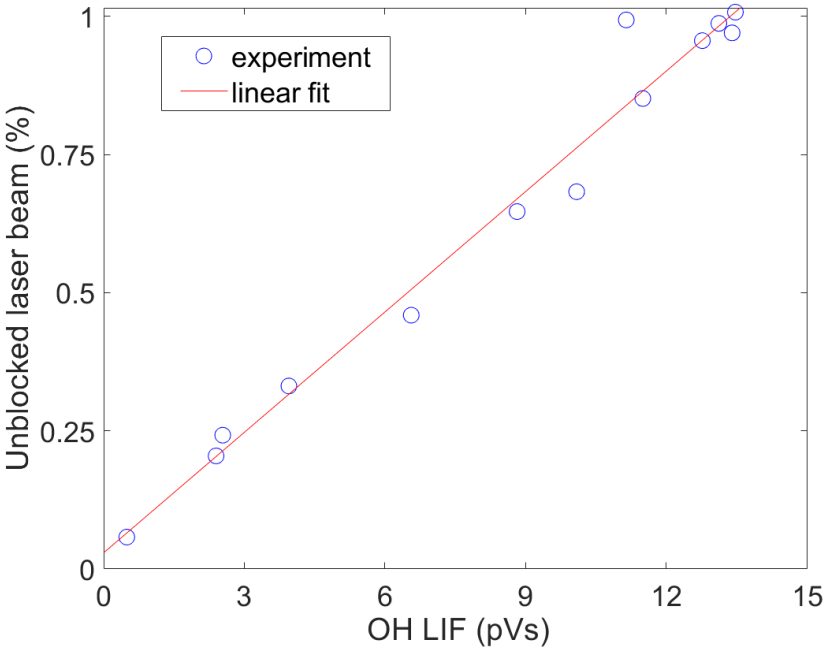

Figure 4.7: A relation between LIF and measured laser energy in the constrained detection region. The detection region is constrained by the crossing volume between the 0.78 mm diameter laser beam and the 0.75 mm wide slit in the imaging plane. The laser energy is tuned by translating a second razor blade across the laser beam. The razor blade is placed between the beamsplitter and the PBS. The linear relation confirms homogeneity of density along this dimension. The measured OH LIF signal is 13.4 pVs within the constrained detection volume.

4.4.4 Pulse Duration and Linewidth of 282 nm laser

Fig. 4.8 shows temporal profile of the laser pulse measured with a fast photodiode (Thorlabs DET10A). The FWHM of the temporal profile is 8.5 ns, which will be used later for simulation.

Fig. 4.9 shows OH absorption spectroscopy in the vicinity of 282 nm. There are two transition lines which are attributed to Q_{21} and Q_1, respectively [57]. Due to small incident power and low transverse speed of the OH beam (less than 0.4 m/s), both power broadening and Doppler broadening (1.4 MHz) can be neglected. By fitting the spectrum with double Gaussian distributions, a laser linewdith of 12 GHz is extracted.

4.4.5 Translation of OH during Photon Collection

Since the OH beam has a large forward velocity (440 m/s with krypton as a carrier gas) along the Z-axis and a long lifetime within the excited electronic state (750 ns), it is likely that some emitted photons will not be collected within the FOV of the collection system, leading to an underestimate of the OH population within the detection volume. Thus, in this subsection we estimate the magnitude of this effect. First, there are several assumptions made:

(1) We assume the laser beam is centered at z=0 mm, so that laser intensity can be expressed as $I_0 e^{-\frac{z^2}{2\sigma^2}}$. Here 2.3σ equals 0.78 mm.

(2) We assume emitted photons can only be collected when its release position is within the FOV of the collection system.

With these assumptions, collectible population at each illuminated position Z can be expressed as:

$$\gamma \propto \int_0^{(z_{view}/2-z)/v} \frac{1}{\tau} e^{-\frac{t}{\tau}} dt, \tag{4.7}$$

where τ is 750 ns, z_{view} is FOV of the collection system, and v=440 m/s.

Since the laser power is set in the linear regime, excited population at each illuminated

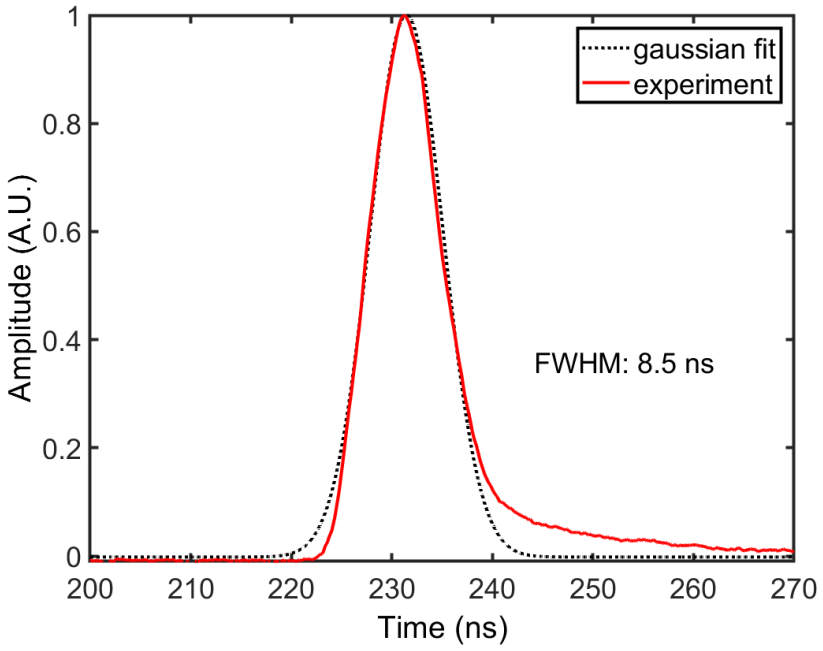

Figure 4.8: The temporal profile of the pulsed laser. The black dashed line is a Gaussian fit. The red solid line is experimental data. The fitted FWHM of the pulse laser is 8.5 ns.

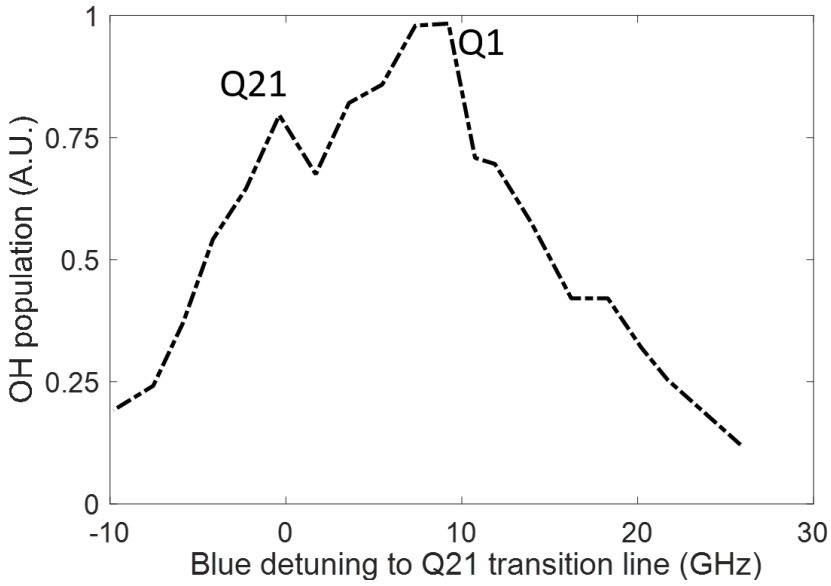

Figure 4.9: OH absorption spectroscopy in the vicinity of 282 nm. There are two transition lines which are attributed to Q_{21} and Q_1. The spectrum can be fit by double Gaussian distributions and the laser linewidth is around 12 GHz.

position z_{mol} can be expressed as :

$$N_{excited}(z_{mol}) \propto e^{-\frac{z_{mol}^2}{2\sigma^2}} \tag{4.8}$$

After combining Eq. 4.7 and Eq. 4.8, overall detectable population within FOV can be expressed as:

$$N_{photon} \propto \int_{-\infty}^{z_{view}/2} e^{-\frac{z^2}{2\sigma^2}} dz \int_{0}^{(z_{view}/2-z)/v} \frac{1}{\tau} e^{-\frac{t}{\tau}} dt \tag{4.9}$$

Fig. 4.10 shows the calculated relation between the FOV and the detectable portion of illuminated population based on Eq. 4.9. Once the FOV is larger than 2.5 mm—the measured value of the FOV, more than 95% of the total fluorescence can be collected. Since the OH velocity is much smaller in the other two dimensions (0.4 m/s), we can conclude that movement of OH beam does not underestimate the photon collection by more than 5%. However, if we switch the carrier gas to neon (800 m/s), we may underestimate the population by 20%.

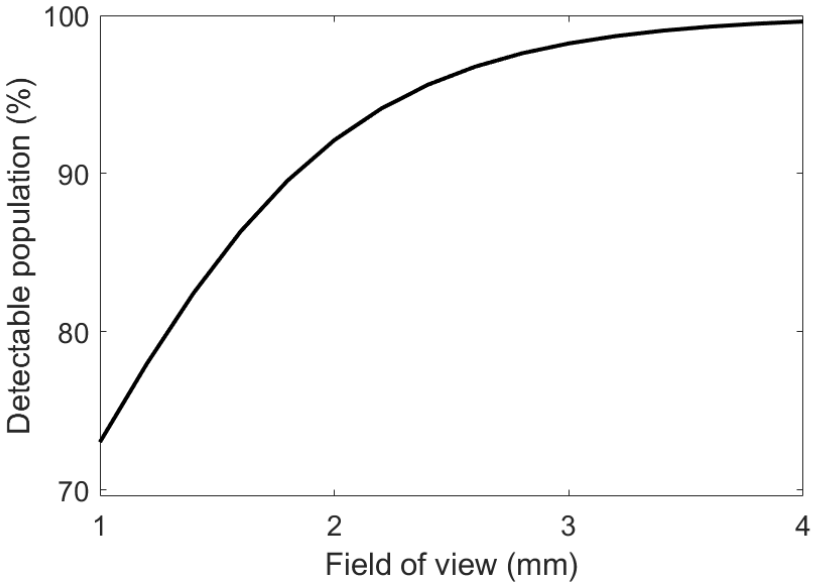

Figure 4.10: The relation between FOV and the detectable portion of illuminated population. Once the FOV is larger than 2.5 mm, more than 95% of total fluorescence can be collected.

4.4.6 Experiment and Simulation of the Rate Equation

Instead of making an approximation for density calibration, we can also numerically solve the rate equations 4.1 to check consistency between experiment and simulation. In the simulation, we do try to consider all the realistic details, such as the temporal profile of the pulsed laser and also averaging effect from a finite laser beam size. Fig. 4.11 shows a good agreement is achieved between experiment and simulation. All the parameters used in the simulation are from the previous measurements. There is only one free parameter for amplitude scaling.

With the well-fitted theoretical model, we are able to use it to check the excitation rate of the total population and figure out the value of the parameter—M in Eq. 4.6. Fig. 4.12 shows time-evolution of population in different states. Only 2% of population is excited, which means M = 0.96.

All the parameters discussed so far related to the OH LIF measurements are collected and summarized in Table 4.1.

Table 4.1: Quantities involved in OH LIF

Symbols	description	Value	Unit
S_{OH}	OH LIF signal	13.4	pVs
B_{21}	Einstein B coefficient for OH	$1.77{\cdot}10^{17}$	$m^3/J/s^2$
E	laser energy	8.3	μJ
V	Detection volume	0.78*0.78*0.75	mm^3
$\rho(\nu)$	spectral density of laser power	N.A.	N.A.
$g(\nu)$	OH line shape function	$\int g(\nu)d\nu = 1$	N.A.
N_g	OH population in the ground state	0.98	N.A.
N_e	OH population in the excited state	0.02	N.A.
$\Delta\nu$	laser linewidth	12	GHz
M	population modification factor	0.96	N.A.
η_{OH}	transmission of filter array at 313 nm	0.57	N.A.
$F(\nu = 1 \rightarrow \nu' = 1)$	Franck-Condon coefficient of OH	0.7	N.A.

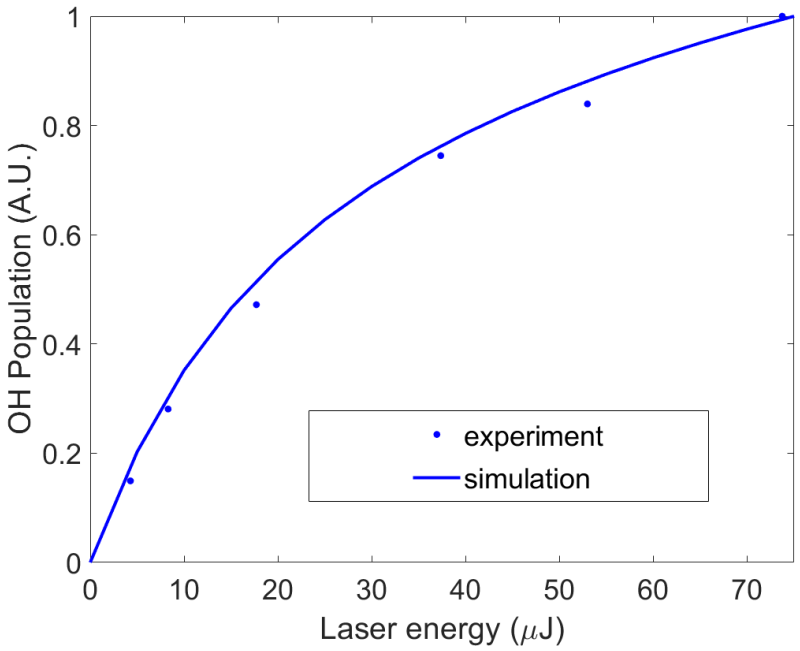

Figure 4.11: A comparison of OH saturation spectrum between experiment and simulation. The circle dots represents experimental data. The blue solid line represents results from simulation. All the parameters used in the simulation are from the previous measurements. There is only one free parameter for amplitude scaling.

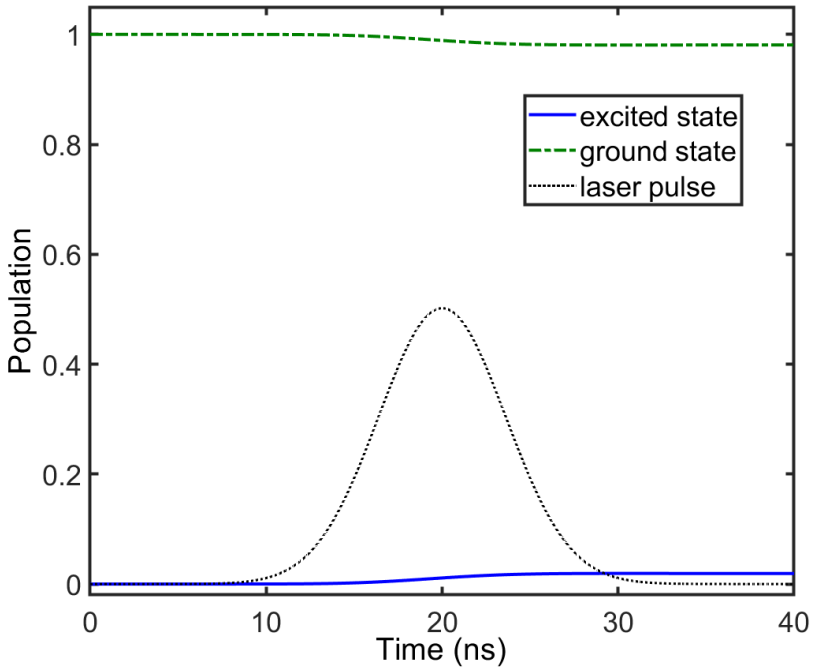

Figure 4.12: Time-evolution of populations in both ground and excited states. The solid line represents population in the excited state. The dot-dash line represents population in the ground state. The dash line represents appearance of laser pulse. About 2% population is excited.

4.5 Raman Scattering with H_2

4.5.1 Angular Dependence of Differential Cross Section of H_2 Raman scattering

Since polarizability induced by H_2 vibration is highly anisotropic, the depolarization ratio [5] of Raman scattering is very small. [68] The small depolarization ratio makes differential cross section of Raman scattering have a strong angle dependence. Before doing Raman scattering measurement, it is important to figure out how Raman scattering signal depends on relative angles. The angles include β_0 (the angle between incident polarization and Y-axis—the center of the collection system) and θ_0 (the angle relates to a certain f-number of the lens). All these angles are labeled in the inset panel of Fig. 4.13 (a).

Based on the formulas in Ref. [67], the normalized cross section can be calculated at different angle pairs. Normalized cross section is defined as a ratio between $\overline{\frac{\partial\sigma}{\partial\mathbf{\Omega}}(\beta_\mathbf{0},\theta_\mathbf{0})}$ and $\frac{\partial\sigma}{\partial\mathbf{\Omega}}(\mathbf{90^\circ},\mathbf{0^\circ})$. Fig. 4.13 (a) shows a calculated relation between normalized Raman differential cross section and θ_0 (f-number of lens) with β_0=90 °. For our experiment, θ_0=0.4 and is represented by a dash line. The corresponding normalized cross section is 96%.

Fig. 4.13 (b) shows a relation between normalized Raman differential cross section and angle β_0. If polarization is maintained within 6° relative to the X-Z plane, normalized differential cross section can be more than 90% of the maximal value as θ_0=0.4. Since extinction ratio of the PBS is more than 10,000, we only need to guarantee orientation accuracy of the PBS is within 6°, which is very easy to do. Thus, it is reasonable to use the maximal cross section to represent the averaged cross section for density calibration calculation.

The differential cross section of H_2 can be calculated from the equation $\frac{\partial\sigma}{\partial\mathbf{\Omega}}(\mathbf{90^\circ}) = \mathbf{A}\frac{\nu_\mathbf{s}^\mathbf{4}}{(\nu_\mathbf{i}^\mathbf{2}-\nu_\mathbf{p}^\mathbf{2})^\mathbf{2}}$ in Ref. [67], of which ν_i is 84800 cm^{-1}, ν_s is 31181 cm^{-1}, ν_p is 35336 cm^{-1} and A=$8.74\cdot10^{-28}$cm^2/sr. The calculated cross section is $2.3\cdot10^{-29}$cm^2/sr.

[5] Depolarization ratio is the intensity ratio between perpendicular component and the parallel component of Raman scattered light.

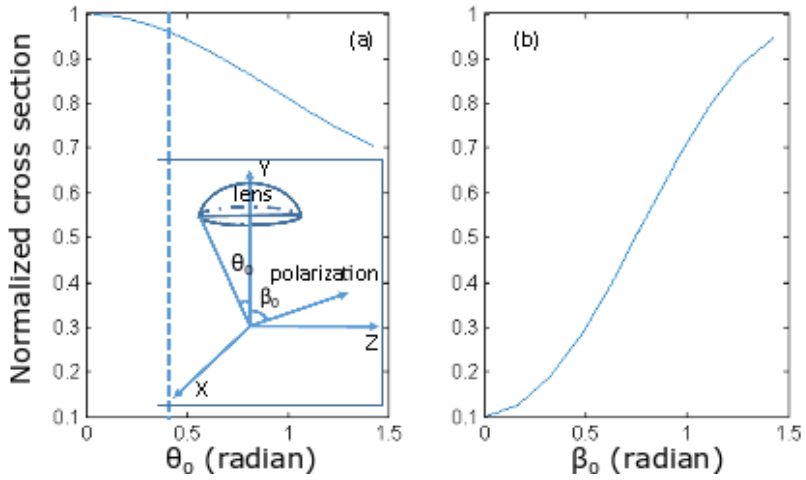

Figure 4.13: Normalized Raman differential cross section under different angle pairs. Normalized differential cross section is defined as the ratio between averaged differential cross section and maximal differential cross section. (a) Relation between normalized differential cross section and angle θ_0 (f-number of lens) as β_0=pi/2. For our experiment, θ_0=0.4 and is represented by a dash line. The corresponding normalized cross section is 96 %. (b) Relation between normalized differential cross section and angle β_0 as θ_0=0.4.

4.5.2 Raman Scattering Measurement

By filling the chamber with varying pressures of H_2, we can figure out a relation between Raman scattering signal and H_2 pressure, as shown in Fig. 4.14. By fitting the experimental data with a linear curve, Raman scattering can be extracted and is 1.2±0.1 pVs/Torr.

All the parameters related to Raman scattering that have been discussed thus far are collected and summarized in Table 4.2.

Table 4.2: Quantities involved in Raman scattering

Symbols	description	Value	Unit
S_{H_2}	H_2 scattering signal	1.2±0.1	pVs
n_{H_2}	density of H_2 per Torr at room temperature	$3.2{\cdot}10^{22}$	m^{-3}
E	laser energy	8.3	μJ
η_{H_2}	filter transmission for 319 nm	0.29	N.A.
$\frac{\partial\sigma}{\partial\Omega}(90°)$	differential cross section of H_2 Raman scattering	$2.3{\cdot}10^{-29}$	cm^2/sr

4.6 Final Calibrated OH Density at the Decelerator Exit

After putting all the related parameters of table 4.1 and table 4.2 into Eq. 4.6, the measured OH density is $1.9{\cdot}10^5 cm^{-3}$ at the end of the Stark decelerator.

4.7 Density Calibration along the Stark Decelerator

We repeat the density calibration at two more positions along the decelerator by exactly following the same procedure. The measured densities are summarized in table. 4.3. Between the trap and 32nd stage, dilution of density can be nicely explained by a beam expansion in three dimensions. However, if we compare the density between "before skimmer" and 32nd stage, density at 32nd stage is one order lower than what it should be, which suggests there is a strong "skimmer-clogging" preventing the highest density beam from going through. In the next chapter, we are going to talk about how to use a skimmer cooing technique to suppress the "skimmer-clogging" and potentially boost the density loaded into the downstream stark decelerator.

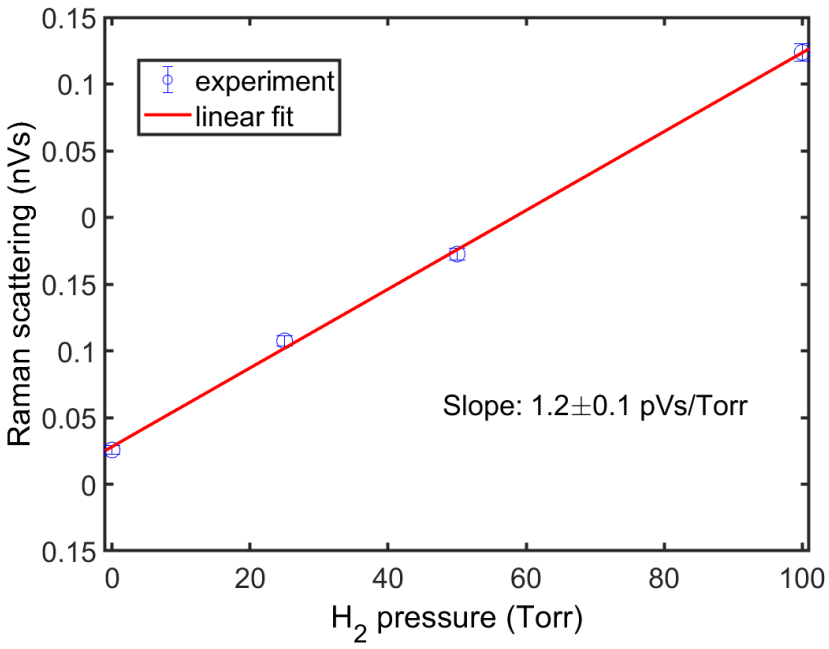

Figure 4.14: Raman scattering signal at different H_2 filling pressures. The blue dots are experimental data. The blue solid line is a linear fit. The slope of the linear fitting correspond to the scattering signal and is 1.2±0.1 pVs/Torr.

Table 4.3: OH density along the decelerator

Position (away from valve in cm)	temporal width (μs)	density (cm^{-3})
Trap (96)	350	$1.9{\cdot}10^5$
@ 32th stage (40)	175	$2.0{\cdot}10^6$
Before skimmer (9)	40	$3.2 \cdot 10^9$

Chapter 5

Enhancing Radical Molecular Beams by Skimmer Cooling

5.1 Motivation

There have been numerous improvements implemented in supersonic beam sources to boost initial densities.[69–72] However, the full performance[73] of a high density beam is limited by the formation of shockwaves near a conical collimating aperture known as a skimmer. Shockwaves are thin nonisentropic layers in a flow, with thicknesses on the order of several local mean free path lengths. The occurrence of shockwaves near a downstream surface is unavoidable in order for the leading edge of a continuum flow to match boundary conditions. Once the bulk of the flow encounters the shockwaves developed inside the skimmer, the beam transmission is greatly reduced. This phenomenon of dramatic beam transmission suppression is named—"skimmer-clogging". In order to mitigate clogging, several key designs to improve the skimmer throughput have been implemented. The optimal angles for cone-shaped skimmers have been demonstrated for Campargue-type beam sources,[74, 75] which operate continuously with relatively high background pressure. For Fenn-type or pulsed sources in the rarefied regime, the clogging is less predictable as a function of cone angles, but still benefits from design optimization. The optimal parameters are determined by a compromise between a small external angle, which can prevent detached shockwaves, and a large internal angle, which minimizes the beam-wall collisions inside the skimmer. Further improvements are possible through more complex slit-skimmers.[76] However, even in these optimized designs, the valve-skimmer distance is still a critical parameter. In most experiments, the valve-skimmer distance has to be at least several hundred nozzle diameters[70] to avoid the formation of shockwaves.

This large separation reduces, in an inverse squared manner, the density that can be loaded into a science chamber located after the skimmer. There is therefore an unavoidable trade-off between density reduction due to a large valve-skimmer distance and beam attenuation induced by clogging. Recently, a new and very general technique "skimmer cooling" has been applied to pulsed beams and shown to significantly suppress skimmer-clogging for well-behaved carrier gases.[77] This can be explained intuitively as follows: once the surface of a skimmer is cold enough to adsorb the carrier gas particles without reflection upon contact, the surface boundary conditions for the flow are effectively removed to infinity, which guarantees that there will not be shockwaves. This cooling technique thus overcomes the density-limiting trade-offs. We go beyond this proof-of-principle work and apply this skimmer cooling approach to discharge-produced radical and metastable beams seeded in a carrier gas. Before jumping into details of skimmer cooling technique, first we want to talk about the characterization of our new pulsed valve—Even-Lavie valve, which is brought into our lab to replace our previous state of the art—PZT valve.[57]

5.2 Characterization of Even-Lavie Valve

The Even-Lavie valve has been widely used in molecular experiments. Once around 20 Amperes pulsed current is applied through solenoid coils, a magnetic stainless steel plunger is attracted so as to open the valve and release several tens μs wide molecular pulse. At rest, a soft spring pushes the plunger against a Kapton gasket for sealing. The maximal repetition rate is 1000 Hz and the maximal stagnation pressure is 1450 PSI. Prior to the exit of the valve, a dielectric barrier discharge (DBD) is installed for discharging to generate radicals and metastable species.

5.2.1 Pre-experimental Test of Even-Lavie Valve

Before characterizing the valve by measuring molecular beams, there are several important points to keep in mind.

(1) Since ammonia can corrode Kapton gaskets and destroy sealing, it is not suggested to run Even-Lavie valve with ammonia.

(2) Use tiny 1/16" pipe to connect the gas inlet line of Even-Lavie valve to a regulator of a gas cylinder to minimize dead volume, which saves a lot of gas because of the very high pressures the valve can be run with.

(3) Once the gas cylinder is connected, set stagnation pressure to 1000 PSI and dip the whole valve body into a vessel full of isopropyl alcohol for leak checking. A good sealing means only one bubble is released every 10 seconds from the front or rear side of the valve. More frequent bubbles means the sealing is inappropriate.

(4) If the sealing is good, mount the valve vertically and fill the trumpet-shaped nozzle of the valve with alcohol. Operate the valve but without the discharge. If the opening time is tuned properly, droplets can be ejected several centimeters high.

5.2.2 A Comparison between Even-Lavie Valve and PZT Valve

With a functioning valve, we can begin to measure the production of OH radicals. OH can be obtained through discharge of water vapor, which is provided by having water-soaked glass fiber filter papers (Whatman) installed inside the valve between the nozzle and a high-pressure neon gas cylinder. To stabilize the performance of the DBD, a tungsten filament is inserted into the source chamber to seed electrons towards the nozzle for discharge. With the extra filament, the OH yield can be improved by a factor of 2 and the stability of the discharge becomes much better. The stability of the discharge can be monitored by measuring glow from discharge. Empirically, by watching the glow directly you can have a good feeling whether there is discharging and how stable it is. One thing you should keep in mind is that UV light can be released during discharging, so that try to avoid staring at the glow for too long, or wear plastic safety glasses which generally absorb UV. In order to optimize the production of OH, there are several things to pay attention to:

(1) The optimal discharge delay, which is relative to a valve firing, highly depends on the mass of carrier gas, stagnation pressure and valve open duration. You should optimize the

discharge delay every time when you switch to a different carrier gas or change any other parameters.

(2) Since plasma initiated by the discharge can corrode the gasket, it is suggested to run the discharge voltage under 1.6 kV for the sake of a long lifetime valve. Moreover, the number of the RF discharge pulses should be controlled under 30 for the same purpose of having a long valve lifetime. In experiment, we find the higher the applied voltage, the more OH production.[1] We may consider to run the valve with a higher RF voltage in case we are eager for more density at some point.

(3) The duration of the valve opening should be controlled under 35 μs. According to our experiences, a longer valve open is not able to improve the molecule yielding and the valve has a larger chance of not being able to close completely. You can figure out the quality of valve closing by monitoring background pressure in the source chamber. If the valve is not able to close completely, you can run the valve open duration above 40 μs for a few seconds to give the plunger a brief momentum kick and overcome any accidental friction. So far all incomplete closing problems have be fixed successfully by this method.

We are able to make a quantitative comparison between an optimized Even-Lavie valve and an optimized PZT valve[57] with an identical detection system. In order to be sensitive only to the OH peak density but not the beam width, the detection volume is restricted to 1 mm^3 by the intersection of a 1.5 mm diameter laser beam and a 0.5 mm wide slit in a focal plane of the fluorescence collection system. The comparison is summarized in Table 5.1. For the PZT valve, OH is generated by DC discharge instead of a DBD. The different discharge mechanism can be the reason why OH yielding of PZT (Ne) is twice as much as that of Even-Lavie (Ne) valve. However, the DBD is able to produce a much colder beam. Overall, if we compare phase space density (PSD) between two valves, the Even-Lavie valve behaves better. In summary, the Even-Lavie valve is demonstrated behaving better than PZT in several aspects:

[1] We have found the OH production at 2.5 kV is twice as much as the production at 1.6 kV.

(1) In our previous experiment, a PZT valve is used for OH production with Kr as a carrier gas. With the new valve and neon as a carrier gas, we are able to increase the PSD by more than an order, which is a real improvement for the future of OH collision studies.

(2) The large speed ratio of the Even-Lavie valve makes it a unique valve for the purpose of studying cold intra-beam collisions below the Kelvin regime.

(3) Since the total flux from the Even-Lavie valve is an order smaller than the PZT valve due to its smaller nozzle diameter and a much shorter pulse duration, the Even-Lavie valve is better for skimmer cooling experiments since it affords a much longer run-time without thermal cycling to remove adsorbed gases.

Table 5.1: A comparison between Even-Lavie valve and PZT valve

	Even-Lavie (Ne)	PZT (Ne)	PZT (Kr)
Peak density (normalized by PZT Kr)	2	4	1
Temperature (K)	0.33	1	1.3
speed ratio(v/σ)	60	30	15
PSD (normalized by PZT Kr)	16	6	1
background pressure (Torr)	$5 \cdot 10^{-6}$	$4 \cdot 10^{-5}$	$4{\cdot}10^{-5}$

5.2.3 Repair of Even-Lavie Valve

After a full year of valve operation, there is a clear reduction of OH production. Thus, we disassemble the valve and try to figure out the causes. Fig. 5.1 shows the details of Even-Lavie valve.[2] The manual [78] has very clear procedures to follow for successfully disassembling and assembling the valve. The only thing I want to emphasize is since there are many small springing pieces inside the valve, try to disassemble the valve in a small and well covered space in order to reduce the chance of losing these small pieces. It is suggested to change two gaskets (2-04-100 and 2-07-01) as shown in Fig. 5.1 every year. After disassembling the valve, we carefully look at the used gasket (2-04-100) under a 50X microscope. The used gasket is shown in the panel (a) of Fig.

[2] The figures are gotten from a manual of Even-Lavie valve.[78]

5.2. Since the gasket (2-04-100) experiences both the corrosion from plasma and also pulsed but frequent punching from the plunger, the edge of the center hole looks really bad compared with a brand new one as shown in panel (b). The non-smooth edge can definitely reduce the efficiency of supersonic expansion and decrease the signals.

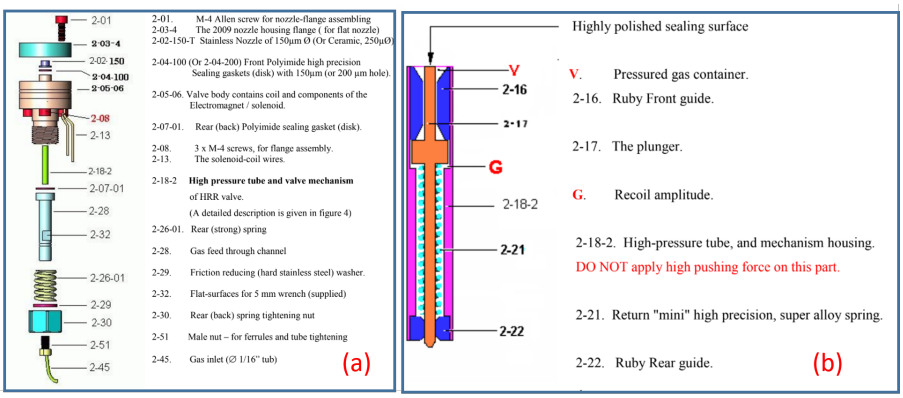

Figure 5.1: Details of Even-Lavie valve. The figures are gotten from a manual of Even-Lavie valve.

We also put the plunger under the 10X microscope. As shown in panel (a) of Fig. 5.3, the strong discharging blackens and scratches the surface of the plunger. The non-polished surface can behave sticky and prevent the valve from opening smoothly. After we polish the surface with a 0.5 μm diamond paste, a smooth surface is recovered as shown in panel (b) of Fig. 5.3.

After reassembling the valve, we still follow the procedures mentioned before to check the valve sealing. Dip the whole valve inside alcohol and count emergence of bubbles. Do not feel surprise, if there is a much smaller amount of bubbles than usual showing up during the first valve operation after assembling. This phenomena is very likely due to the friction from imperfect valve installation. The imperfection can be fixed by increasing the valve open duration above 40 μs. A large and brief momentum kick can help all the small parts of the valve adapt with each other and get rid of the extra friction. After repairing the valve, OH production is completely recovered. Then, we can move on to test the behavior of skimmer cooling for different species.

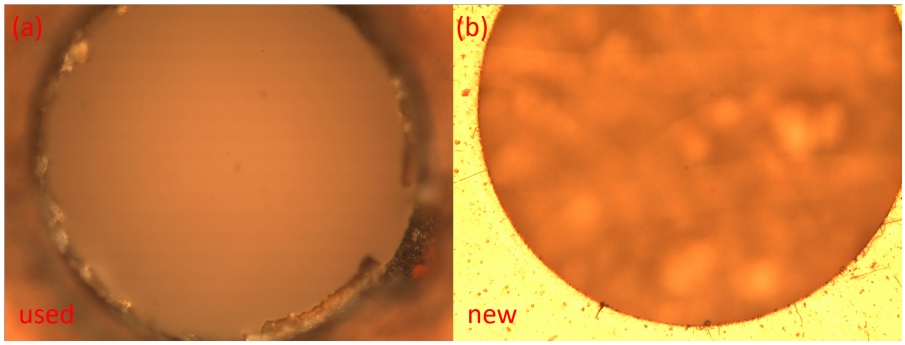

Figure 5.2: A comparison between used and new gasket (2-04-100) under 50X microscope. The diameter of the center hole is 200 μs.

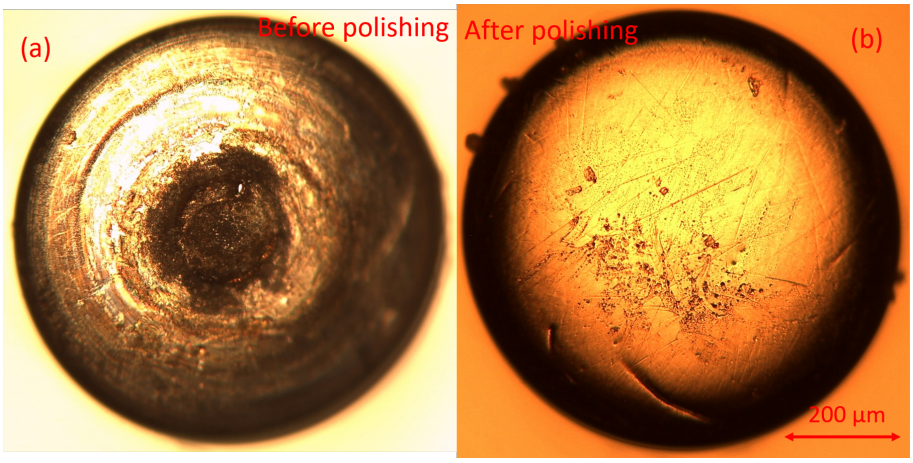

Figure 5.3: A comparison between unpolished and polished plunger under 10X microscope.

5.3 Experimental Apparatus of Skimmer Cooling

Fig. 5.4 shows our experimental setup. The heart of this apparatus is a home-built, cryo-cooled, 3 mm aperture skimmer, which has a 30° external angle and a 25° internal angle. The skimmer is indium-soldered onto a cold finger, which is thermally anchored to the 2nd stage of a 10 K pulse tube cryostat. A silicon temperature diode is installed several centimeters away from the base of the skimmer and a 20 W Nichrome-wire wrapped heater is bolted near the base of the skimmer to adjust the temperature. We have a two-step recipe for producing a low-temperature skimmer. First, both the skimmer and the cold finger are made of annealed 5N copper, which can provide a much higher thermal conductivity than OFHC.[79] Second, the majority of the cold finger is enclosed by a 70 K radiation shielding box made of OFHC copper, which minimizes the radiative heat load on the skimmer and the cold finger. Under this configuration, we are able to cool the skimmer to 8 K, which is confirmed with the temperature diode, even when the experiment is being run. The low temperature limit of 8 K is close to the no-load temperature of our cryostat, and we determine that the heat load to the skimmer is below 1 W and excellent thermal conduction is established. To study the temperature of the skimmer tip in detail, we performed a thermal modeling of the whole skimmer setup. Our results show a temperature difference of only 50 mK between the tip of the skimmer and the location of the temperature diode with a 1 W heat load.[3] Thus, the measured temperature should faithfully represent the real temperature of the skimmer.

Another benefit of skimmer cooling is that the skimmer acts as an efficient cryo-pump for the source chamber, reducing the background pressure by an order of magnitude to 10^{-7} Torr. This must be weighed against a potential drawback of skimmer cooling—the eventual limiting accumulation of ice. We observe no reduction in performance after a full hour of operation with 200 psi stagnation pressure at 10 Hz repetition rate, but this may be different with a larger incident flux.

In our experiment, three different species are studied: neon, metastable neon (Ne*) and

[3] Temperature gradients for our geometry computed with SolidWorks Simulation Professional 2017.

hydroxyl radicals (OH). A pulsed neon beam is produced by the room-temperature Even-Lavie valve in a non-clustering regime.[70] This valve features a 0.2 mm aperture nozzle. Ne* is generated by a dielectric barrier discharge (DBD) prior to a supersonic expansion. OH is produced in the way as mentioned above. We use a variety of techniques to detect the three species under study. Neon traces after the skimmer are recorded by a fast ion gauge (FIG). A Mach-Zehnder (MZ) Interferometer composed of a pair of backside polished mirrors is used to measure the neon time-of-flight trace at the exit of the nozzle with a laser diameter 2 mm, not shown in Fig. 5.4. Based on the neon density induced phase shift in one arm of the interferometer, we are able to measure the neon temporal distribution. [80] Since at the exit of the nozzle the velocity spread is negligible, the measured temporal width (30 μs) of the beam is attributed to the spatial width (24 mm) of neon beam, which is much larger than the laser beam width. Then, the peak population of time-of-flight trace can be considered as the peak density of the beam and used to characterize the cold skimmer behavior later. The MZ interferometer measurement shows neon has a peak density of $2{\cdot}10^{16}$ cm^{-3} with 200 psi stagnation pressure. Ne* is detected by a micro-channel plate detector (MCP). OH is probed with laser induced fluorescence (LIF). A 282 nm pulsed UV laser orthogonal to the molecular beam drives the transition from the ground state $\left|X^2\Pi_{3/2}, J = 3/2, \nu = 0\right\rangle$ to the excited electronic state $\left|A^2\Sigma, N = 1, \nu = 1\right\rangle$, and the resultant 313 nm fluorescence is focused by a pair of UV lenses onto a photomultiplier tube (PMT).

5.4 Characterization of the Cryogenic Skimmer

5.4.1 Neon

We begin with our results for the neon carrier gas, which confirms the efficacy of skimmer cooling as reported in ref. [77]. A factor of 9 peak signal gain is achieved during cooling from 35 K to 8 K. As shown in Fig. 5.5(a), at and above 35 K, only the leading edge of the gas pulse gets transmitted before the formation of shockwaves. In contrast, at 8 K a nearly Gaussian-shaped gas pulse is observed, which indicates clogging mitigation. The peak arrival time at 8 K is consistent

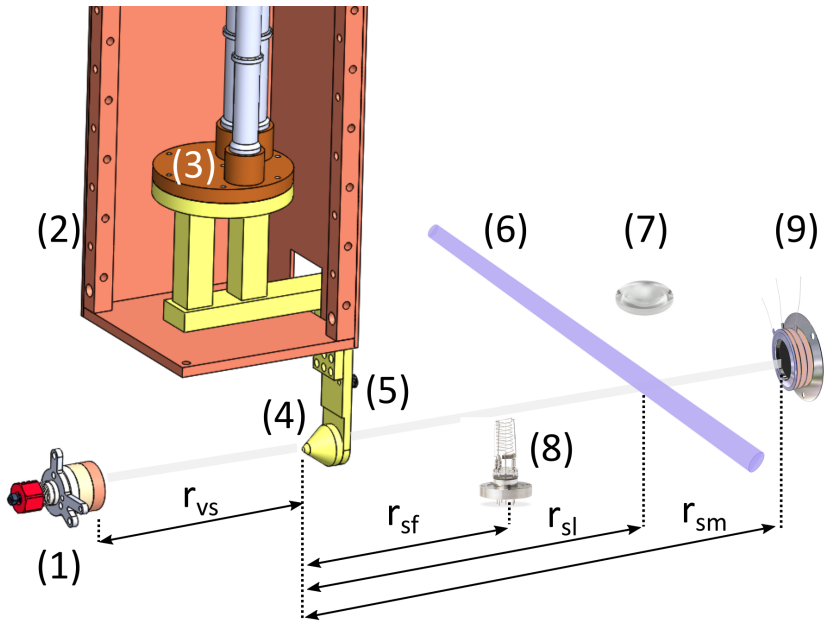

Figure 5.4: Schematic diagram, not to scale. (1) Even-Lavie valve. (2) 70 K radiation shield, of which two side panels are not shown. (3) 2nd stage of Cryomech PT807 10 K cryostat. (4) home-built conical copper skimmer. (5) Lakeshore DT-670 silicon temperature diode used for measuring the skimmer temperature. (6) 282 nm pulsed UV laser. (7) LIF collection lens. (8) Fast ion gauge (FIG). (9) Micro-channel plates (MCP). r_{vs} is the distance between the valve and the skimmer. r_{sf} is the distance between the skimmer and the FIG. r_{sl} is the distance between the skimmer and the laser. r_{sm} is the distance between the skimmer and the MCP.

with a speed of 790 m/s, the expected isenthalpic expansion speed of room temperature neon. The longitudinal temperature in the moving frame is 240 mK ($\pm 10\ m/s$), obtained by deconvolving the initial spatial width measured interferometrically right after the valve from the width of the 8 K time-of-flight trace in Fig. 5.5(a). The resultant neon speed ratio is 80, which is consistent with the unskimmed beam in ref. [[70]] and confirms that the supersonic expansion was complete prior to skimming.

To further understand the extent of clogging mitigation, we investigate two different ways to vary the incident beam flux. When shockwaves are formed inside the skimmer, the clogging effect would worsen with a higher incident flux. One way to achieve a higher incident flux is to increase the stagnation pressure. As shown in Fig. 5.5(b), a ratio of neon before and after the skimmer, which is independent of flux, suggests complete clogging mitigation at 8 K.[4] The other way to vary the incident flux to the skimmer is by changing r_{vs} (the distance between the valve and the skimmer). A continuing rise of the signal at smaller values of r_{vs}, even down to 2 cm, also confirms clogging mitigation (see Fig. 5.5(c)). In the limit of straight-line geometric trajectories for molecules, it is not obvious why the signal at a small, distant detector should grow with reduced r_{vs}. Solid angle increases, but the additional molecules miss the detector. However, when the finite transverse temperature of the beam is considered, some molecules which ought to miss the detector in the limit of straight-line trajectories do not, and vice versa, so that signal can in fact increase. The transverse temperature required to explain our observed gain is large, a few Kelvin. This could relate to the bimodal transverse temperature distribution observed for free jets.[73]

5.4.2 Metastable Neon

In a next step, we investigate the behavior of the cold skimmer using Ne*. For Ne*, we observe an even stronger signal increase by 30-fold during skimmer cooling to 8 K (see Fig. 5.6(a)). Moreover, the results indicate that a lower skimmer temperature could potentially lead to an even

[4] We have observed a nonlinear relationship between stagnation pressure and neon flux from the valve above 400 psi, likely due to the mechanical influence of the stagnation pressure on the valve sealing poppet.

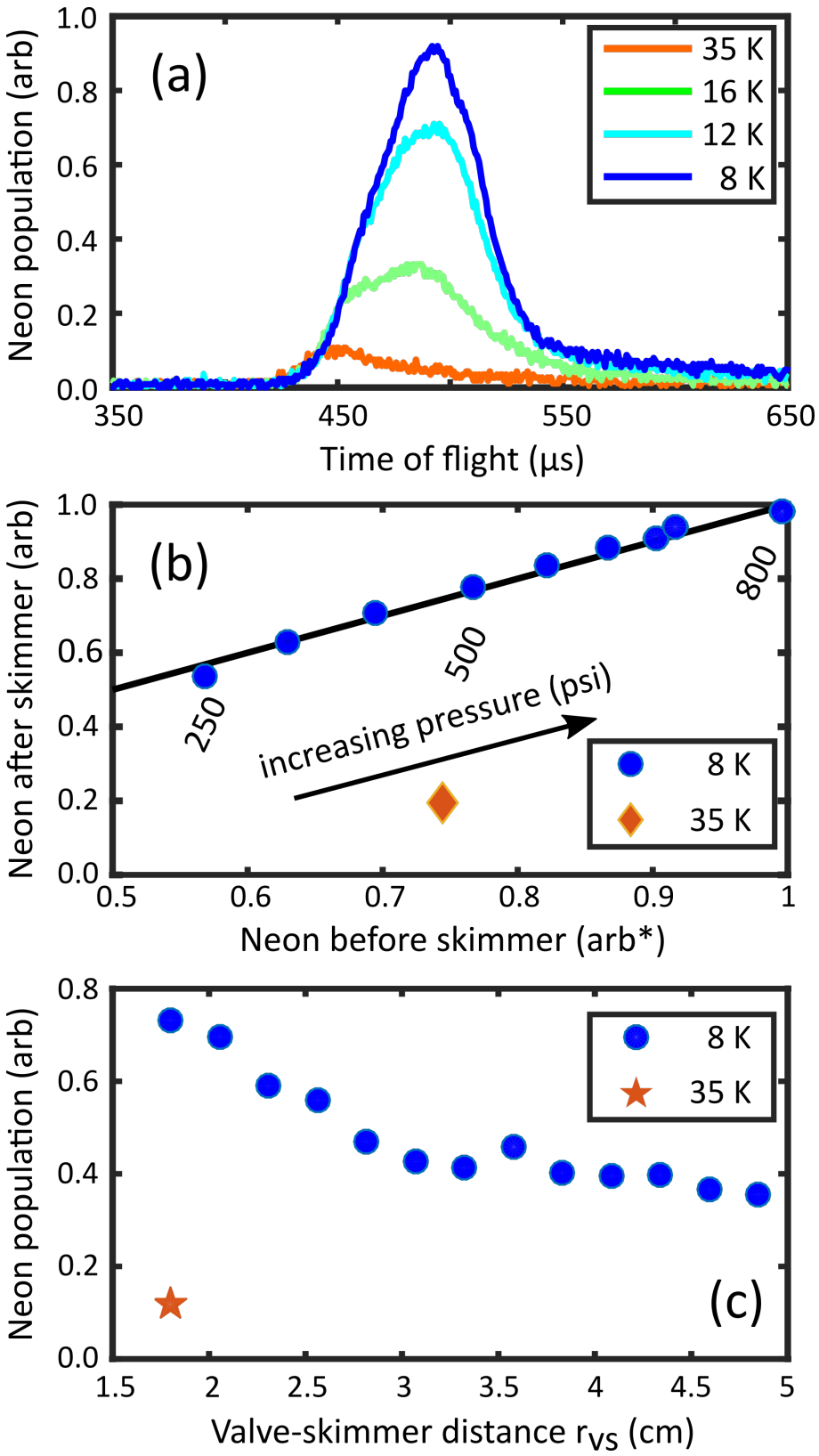

Figure 5.5: (a) Neon throughput for varying values of the conical skimmer temperature. The stagnation pressure is 400 psi for panel (a) and $r_{vs} = 3\ cm$ for panels (a-b). The transmitted Neon is measured at $r_{sf} = 36\ cm$ for panels (a-c). (b) Peak Neon signal before and after the skimmer at various stagnation pressures between 250-800 psi. The black solid line is a linear fit through the origin. A data point taken at 35 K (orange diamond) is included for comparison. (c) Peak Neon signal at different r_{vs} with stagnation pressure 200 psi. A data point taken at 35 K (orange star) is shown for comparison.

larger gain. The extra gain of Ne* relative to neon can be attributed to the variation of optimal discharge timing as a function of temperature (and hence the degree of clogging). To achieve a maximal yield, the discharge timing should coincide with the peak of a carrier gas pulse. However, in the presence of clogging, only the front part of the carrier pulse would be able to go through the skimmer effectively before the skimmer is clogged (see the neon pulse comparison between 35 K and 8 K in Fig. 5.5(a)). Hence, the optimal discharge timing for the clogged beam must be set earlier than that in an unclogged one, to match the clogging-induced effective peak shift (see Fig. 5.6(b)). Only when the clogging is mitigated can we operate the discharge at its optimal timing coinciding with the peak of the carrier pulse. This intuitive picture can be confirmed by examining the location of a discharge-induced depletion under the envelope of the neon carrier gas. We do this by taking FIG time of flight profiles of neon at $r_{sf} = 36\ cm$ with the discharge toggled on or off. Fig. 5.6(c) shows this for the optimal discharge timing of 83 μs, starred in Fig. 5.6(b). It is seen that the Ne* is indeed produced right at the center of the neon packet.

Not only is the highest density achieved by seeding species at the peak of a carrier gas pulse, the most efficient supersonic cooling also occurs at the peak. We confirm this by fitting Gaussian distributions to the flight profiles of Ne* and extracting longitudinal temperatures. It is found that a Ne* beam as cold as 180 mK can be produced with the optimal 83 μs discharge delay. For comparison, the temperature increases by 40% to 260 mK with a smaller delay of 65 μs.

5.4.3 Shockwave and Diffusive Clogging

We now explore clogging mitigation during skimmer cooling in more detail, and uncover a transition between two regimes. Our approach is empirical—we extract information about the nature of the clogging from the shape of the transmitted beam, where shape refers to its time of flight profile at the detector. As a figure of merit, we introduce the beam shape ξ—which compares the time of flight profile $w_T(t)$ at temperature T to the Gaussian-shaped, unclogged profile $w_G(t)$

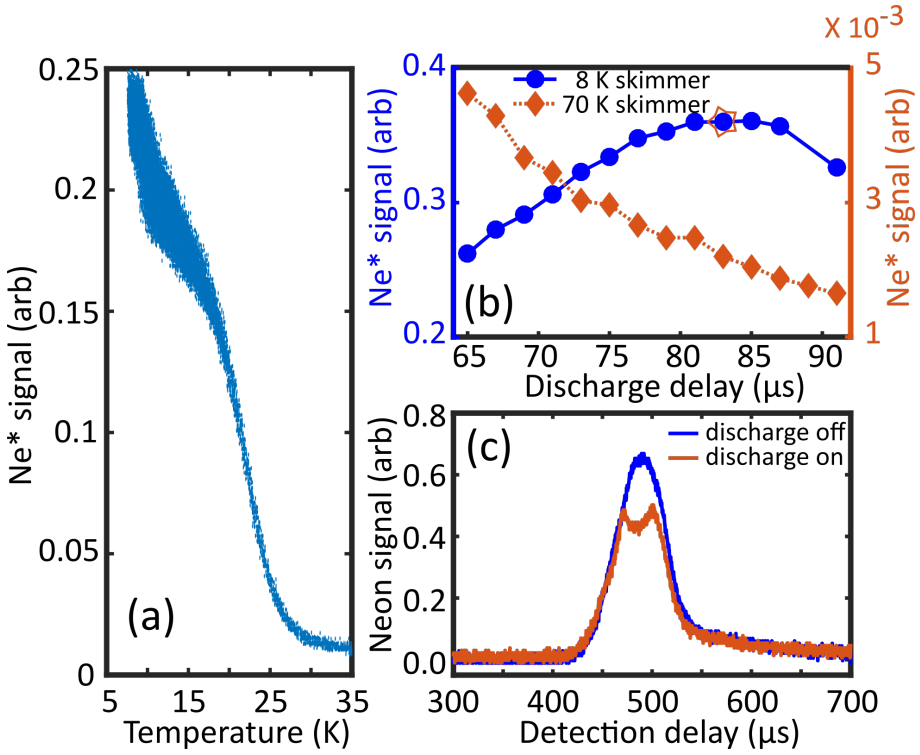

Figure 5.6: (a) Metastable Neon (Ne*) peak signal vs conical skimmer temperature. The stagnation pressure is 200 psi. $r_{vs} = 1.8\ cm$ for panels (a-c). The discharge delay is fixed at 83 μs. Each shot of experiment is reflected as a point in the plot. (b) Transmitted Ne* population vs. the discharge delay under two different temperatures. Ne* is seeded in the beam via dielectric barrier discharge (DBD) and detected at $r_{sm} = 160\ cm$. The DBD is composed of 17 cycles at 800 kHz. The stagnation pressure is 350 psi for panels (b-c). The delays here are measured relative to the valve firing for panels (b-c). (c) Neon pulses measured by FIG at $r_{sf} = 36\ cm$ with the discharge on or off at 8 K. The discharge has an 83 μs delay relative to the valve firing, starred in panel (b). This optimum Ne* discharge timing occurs at the center of the neon beam, as evidenced by the clear depletion right at the peak position.

observed at 8 K:

$$\xi(T) = \frac{\int w_T(t) w_G(t) dt}{\sqrt{\int w_T^2(t) dt \int w_G^2(t) dt}} \tag{5.1}$$

When $\xi = 1$, w_T and w_G are identical up to a linear scaling; any difference in their shapes reduces the values of ξ below unity. As shown in Fig. 5.7(a), for neon observed by FIG we find $\xi(35\ K) = 0.6$, corresponding to a vastly different profile, while $\xi(12\ K)$ is nearly unity. We can also use ξ to study the beam shape observed by MCP for Ne* at different skimmer temperatures, see Fig. 5.7(a). The time-of-flight profiles of Ne* require additional interpretation related to the double peak structure shown in the inset. We associate the pre-peak with Rydberg neon species that are field ionized and accelerated into the detector ahead of the Ne*. We confirm this by increasing the voltage of the front plate of the MCP—which dramatically enhances the pre-peak and leaves the second unaffected. To calculate ξ for Ne*, we first use double Gaussian functions to fit the beam profile, and then we exclude the first Gaussian profile attributed to the Rydberg species.

Having established ξ, we now evaluate it for Ne* across all measured profiles during skimmer cooling from 35–8 K. The results are representative of those for neon and OH as well. As shown in Fig. 5.7(a), ξ increases dramatically from 35–20 K but then levels off near unity well before the gains of transmitted Ne* population cease, see Fig. 5.6(a). This can be understood further by plotting ξ directly against Ne* population as in Fig. 5.7(b). The concave shape suggests the existence of two distinct clogging processes as the skimmer is cooled down—during the first process the beam shape increases but without significant signal gain, and during the second process the signal continues to gain after the beam shape has mostly stabilized.

We can interpret the two processes as follows: the first process is the suppression of dispersive shockwaves. These shockwaves are an inevitable phenomenon when a continuum supersonic flow interacts with boundaries such as the skimmer tip. They extend across the beam and cause significant heating and beam shape deviation. As noted and directly imaged in ref. [[77]], skimmer cooling reduces the influence of these shockwaves primarily by adsorbing molecules that would have

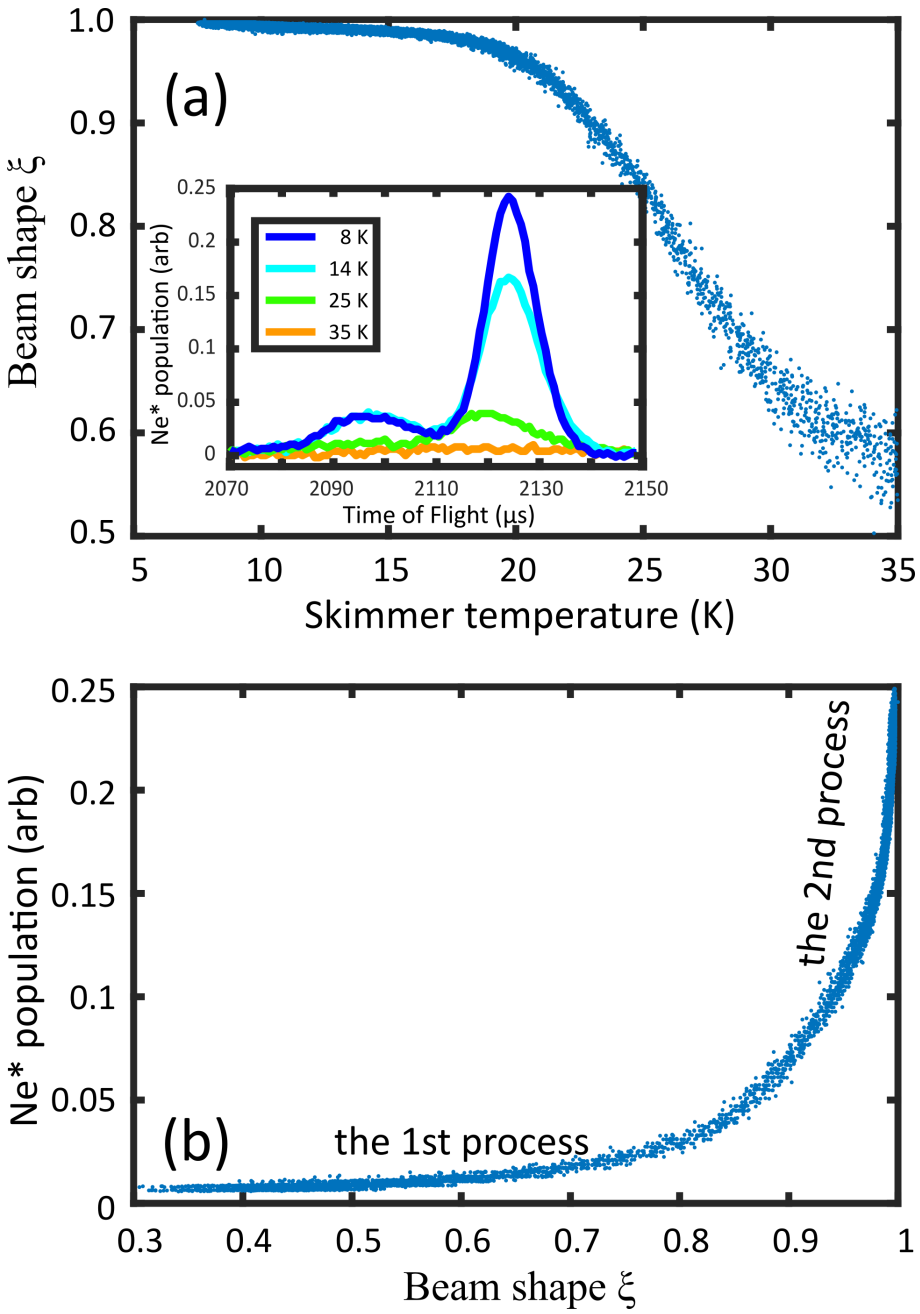

Figure 5.7: (a) The beam shape of Ne* vs conical skimmer temperature. Beam shape ξ is defined as how close the time of flight profile at a certain temperature is to the unclogged and nearly Gaussian profile observed at 8 K. The inset panel shows transmitted Ne* beams at different skimmer temperatures. The double peak structure is related to minority species generated during the discharge, see the main text. (b) The Ne* peak signal vs ξ. From the bottom left to the top right, the temperature varies from 35 K to 8 K. The stagnation pressure is 200 psi and r_{vs}= 1.8 cm for panels (a-b). Each shot of experiment is reflected as a point in the plot.

otherwise participated in the formation of shockwaves. The adsorption relaxes the mass flow continuity constraints for shockwave formation and reduces their influence until they are completely suppressed. This is evidenced by the lack of heating or beam shape deviation measured by our near-unity ξ parameter below about 20 K.

The additional two-fold signal gain below 20 K is associated with the rarefied equivalent of a shockwave—particles that reflect from the skimmer and interfere with the beam but are nonetheless too rarefied to form shockwaves. We refer to this as diffusive clogging, and further interpret it as follows: When molecules that reflect off of the skimmer pass through the beam with few enough collisions, shockwaves no longer form. These reflected molecules, even when fully accommodated to the cryo-cooled but stationary skimmer, have hundreds of Kelvin worth of collision energy relative to the fast, supersonically cooled beam. Therefore, collisions between reflected molecules and beam molecules result in pairs that are still very hot relative to the beam. In the shockwave regime, these pairs collide further until all of their energy is dissipated into the beam, leading to the beam heating discussed above; but in the diffusive regime, they stop colliding while still hot. Thereafter, they rapidly diffuse relative to the cold centerline beam and are not detected. In this manner, the beam retains its cold temperature and near-unity ξ parameter despite population loss. The transition between these regimes should correspond with the expected number of collisions approaching unity. Specifically, the mean free path λ of beam molecules into reflected molecules (or their daughter pairs) is comparable to the length-scale L of the skimmer tip region relevant to shockwave formation. Throughput across this region should then follow Beer's law– with the fraction passing unperturbed given by $e^{-L/\lambda} \propto 1/e$. This leaves a factor of e to be gained by further suppression of diffusive clogging.

Therefore, this simple model–shockwave suppression due to rarefaction when the mean-free path ratio reaches unity– explains both the observed beam shape behavior and the large gain remaining in the diffusive clogging regime. An additional corollary to this continued diffusive clogging is that without perfect adsorption, skimmer shape still plays a role, since a small external angle and a sharp tip reduce the ability of molecules to interfere in the diffusive clogging manner. In

preliminary experiments with a thicker, 70° external angle skimmer, we found less optimal results than with the 30° skimmer used for all data reported here.

5.4.4 OH Density

It is now clear that skimmer cooling can mitigate both shockwaves and diffusive clogging, but a key question is whether this method really represents an absolute improvement relative to the previous state of the art. To address this, we perform an OH density comparison between two optimized skimmers—a 300 K commercial skimmer and an 8 K skimmer (see Fig. 5.8). The LIF laser is located reasonably close to the skimmer ($r_{sl} = 6.6\ cm$). Our results show a factor of 30 gain achieved by skimmer cooling. In this region, we expect two types of gain. The first would be the geometric gain resulting from a reduced valve-detector distance. This gain can be further separated into transverse and longitudinal contributions. Assuming that the transverse density expansion follows $1/r^2$ position dependence in the free flight regime, the expected transverse contribution is a factor of $(20.9\ cm/8.4\ cm)^2 = 6.2$. The longitudinal expansion contributes to another factor of $8.9\ \mu s/7.5\ \mu s = 1.2$, according to the FWHM of Gaussian fittings in Fig. 5.8. The second gain would be from actual clogging mitigation. This gain can be estimated by moving the laser and detection system to be far behind the skimmer ($r_{sl} = 70$ cm), where the geometrical gain is negligible, and repeating the OH comparison between two skimmers. A population gain of 3.2 between 8 K and 300 K skimmers is found. Overall, the total expected gain is thus 6.2 x 1.2 x 3.2 = 24, which reasonably agrees with the measured factor of 30. The aforementioned measurement far behind the skimmer also enables us to find the temperature of the OH beam. With either skimmer, we find 350 mK (±13 m/s, speed ratio 60) in the beam frame, suggesting a reasonable equilibration with the 240 mK carrier. OH is generated 83 μs later than the valve firing, which is confirmed by measuring the UV light from discharging. Subtracting this and accounting for distance gives the expected speed of 810 m/s for both skimmers.

To ensure that the commercial skimmer is actually well optimized, we see that the beam shape after the commercial skimmer is also near unity, confirming that there are no shockwaves

developing. The skimmer position of $r_{vs} = 12\ cm$ is experimentally selected for the optimum density and consistent with the recommended distance in ref. [70]. As has been discussed, we do expect to find an optimum that involves a trade-off between clogging and geometric density reduction.

5.5 A Cryogenic Hexapole

Notably, a factor of 30 gain in the OH density is achieved with an 8 K skimmer by combination of clogging mitigation and a smaller valve-skimmer distance. The main question left is whether OH beam brightness by the skimmer cooling can benefit a downstream stark decelerator in the sense of loading efficiency.[5] When we first time integrate the cryogenic skimmer together with the decelerator, it is a little disappointing to notice there is no gain of OH loading efficiency for the decelerator. Instead of a skimmer-clogging, there is a strong clogging behavior from the room-temperature decelerator. To avoid the decelerator-clogging, we have to maintain a large separation between the valve and the decelerator. To compensate a transverse loss due to the separation, a new cryogenic apparatus—cryogenic hexapole is designed and tested to some extent. The hexapole works as molecular lens and is able to image the molecular beam from the valve onto the entrance of a downstream decelerator. Moreover, the cryogenic hexapole can be installed really close to the valve without a clogging. so far, we have demonstrated compared with only the optimized commercial skimmer we are able to double the OH signal loaded into the decelerator with a cryogenic hexapole. There are still several challenges to be addressed to have a fully functioned hexapole. [6] . However, there is no doubt that both a cryogenic skimmer and a cryogenic hexapole will have an important impact on the large variety of experiments that rely on high molecular densities.

[5] Our next generation Stark decelerator will be talked about in the next section.

[6] A much more detailed description of cryogenic hexapole can be found in Dave Reens' thesis.

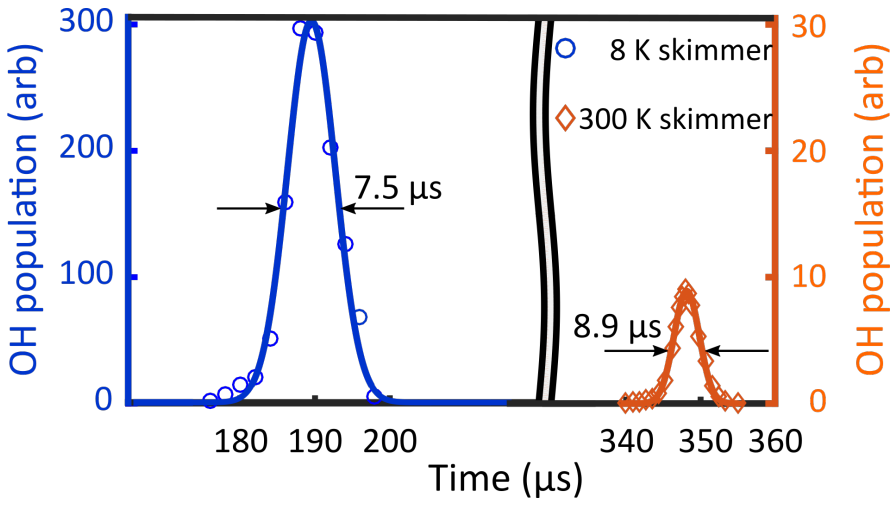

Figure 5.8: A direct comparison between a 300 K commercial skimmer and an 8 K home-made skimmer for use with a hydroxyl radical (OH) beam. The OH density is measured at a fixed position behind the skimmer ($r_{sl} = 6.6\ cm$) suitable for a molecular guide. The blue circle data is taken with an 8 K skimmer and a valve-laser distance of 8.4 cm and the orange diamond data is taken with a 300 K skimmer (Beam Dynamics model: 50.8) and a valve-laser distance of 20.9 cm. The solid lines are Gaussian fits for extracting the relative beam widths. The arbitrary scales for the left and right axes are in the same units. The speed ratio of OH radicals for the two skimmers is identical as expected. Time is recorded relative to valve firing and OH is generated with the same discharge time delay (83 μs) used for Ne*.

5.6 Outlook

We have demonstrated how skimmer cooling can lead to large gains for discharge-produced radicals and metastable species. Our results indicate that this technique can also be applied to many other species and production techniques. As far as other carrier gases are concerned, skimmer cooling could still be a general and feasible technique within a reasonable temperature range. It has been demonstrated that a skimmer temperature on the order of 10 K is sufficient for carrier gas heavier than neon due to their relatively high cryo-condensation temperature.[77] Since lighter carrier gases, such as helium, can provide higher densities and more efficient cooling, it would be very important if this technique could also be extended to them. The challenge is that helium hardly condenses onto a copper surface above 1 K.[81] Nevertheless, skimmer cooling could still become feasible for helium in the 4 K regime with proper sorbents attached to the skimmer surface. It has been shown that with a μm-scale thickness pre-condensed Argon frost layer, the adsorption rate of helium/hydrogen can increase dramatically.[82] Also, simple porous sorbents such as activated charcoals[81] could lead to sufficient adsorption and hence unlock further unprecedented gains in density for future molecular beams.

Chapter 6

A Third-generation Stark Decelerator

6.1 Motivation

During the past 10 years of operation of the second-generation stark decelerator [83], the pre-breakdown current during DC current conditioning had kept increasing, which limited the maximal voltages applied to electrodes. Accompanied with the bad condition of the electrodes, the number of slowing molecules had also reduced by more than factor two. [1] Thus, it is time for us to open the chamber and explore in more details on the surface quality of the electrodes.

6.1.1 Degradation of Electrodes of the Second-generation Decelerator

Fig. 6.1 shows the pictures of the exit side of the malfunctioned second-generation stark decelerator. As shown in Fig. 6.1(a), there are serious black spiral traces on the surface of the last several electrode pins, caused by the electron bombarding. The existence of a strong magnetic field [2] can guide the electrons colliding onto the electrode pins and accelerate the degradation. For the electrode pins exposed to a weaker magnetic field, the surface quality does look much better.

In addition, the decelerator rods also experience serious damage, as shown in Fig. 6.1(b). The damaged parts happen to be the place covered by a magnetic trap mount. These serious burnt marks indicate strong arcing had happened between the rods and the trap mount sleeves. Thus, for the first trial of recovering the decelerator, we decide to ignore the installation of the magnetic

[1] The slowing signal is more sensitive to the degradation of the decelerator than bunching signal.

[2] The field is caused by a quadrupole magnetic trap, which is 10 mm away from the exit of the decelerator and not shown here.

trap.

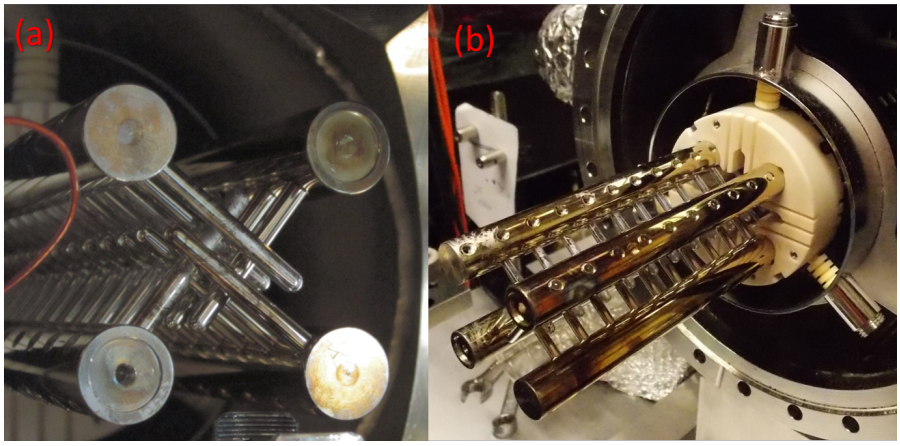

Figure 6.1: The pictures of the exit side of the malfunctioned second-generation stark decelerator.

We exchange the last 40 easily accessible pairs of pins to highly polished ones. We also repolish the end of decelerator rods with 2000 and 4000 grits sandpaper in-situ. Moreover, a viewport is installed at the exit side of the decelerator so as to have an optical access to the surface quality of pins without breaking the vacuum. However, after all the efforts, the deceleration efficiency does not come back to normal [3] and it is limited by a new discovered problem—a surface flashover [4] of insulation mount made of Macor.

6.1.2 Surface Flashover of Macor

Compared with the bulk of insulators, the surface is easier to be ionized and can sustain surface flashover at relatively lower fields. The surface flashover can limit the maximal voltage applied to the electrodes. In order to prevent the surface flashover, our previous rule of thumb is intentionally making several deep grooves onto the insulator so as to increase the surface path between different polarities, as shown in Fig. 6.2. The elongated virtual surface path should reduce the electric field between nearby decelerator rods below 5 kV/cm, which is too small to initiate the surface current. However, the discovery of surface flashover of Macor during a DC current

[3] The population ratio between slowing and bunching is still lower than expected value.
[4] High voltage breakdown along the surface of an insulator.

conditioning (± 12 kV) [83] contradicts our understanding completely. Instead of propagating closely on the top of the insulator, the surface current can hop across the groove and continues propagating from the negative electrode to the closest grounded electrode, as shown in Fig. 6.2. The puzzle bothers us for a while until we realize the appearance of surface flashover is due to the occurrence of triple junction [5] .

The local electric field near a triple junction can be enhanced far more than the value calculated from voltage divided by distance. A simulation in Ref [84] gives a good explanation. Fig. 6.3 shows the field distribution near the triple junction. If the dielectric material (e.g. the Macor) is partially filled between electrodes, there will be a triple junction formed and the equipotential field lines can be squeezed into the free space so as to enhance the field strength near the metal surface. The larger dielectric strength of the insulator, the more enhanced electric field will occur.

For our decelerator, since the surface of Macor is not completely flat, there will be unavoidable triple junction formed between the decelerator rods and the Macor, as labeled in Fig. 6.2. The enhanced field strength near the triple junction can cause the emission of electrons. Since the electric field between decelerator rods is parallel with the Macor surface, the ejected electrons will be pulled along the surface of Macor. Moreover, the enhanced electric field inside the grooves can assist electrons to hop across the gap to continue propagating. Thus, finally there is a complete flashover formed between decelerator rods.

With the better understanding of the high voltage insulation mechanism, we have new rule of thumb for the future high voltage design.

(1) Try to avoid partially filling an insulator between electrodes of different polarities.

(2) Try to separate the electrodes of different polarities as far as possible.

(3) There are many other ways which can be utilized to suppress the field enhancing effect near the triple junction, such as recessing the electrodes, adding guard rings and so on [84].

[5] Triple junction occurs where vacuum, metal and insulator meet with each other.

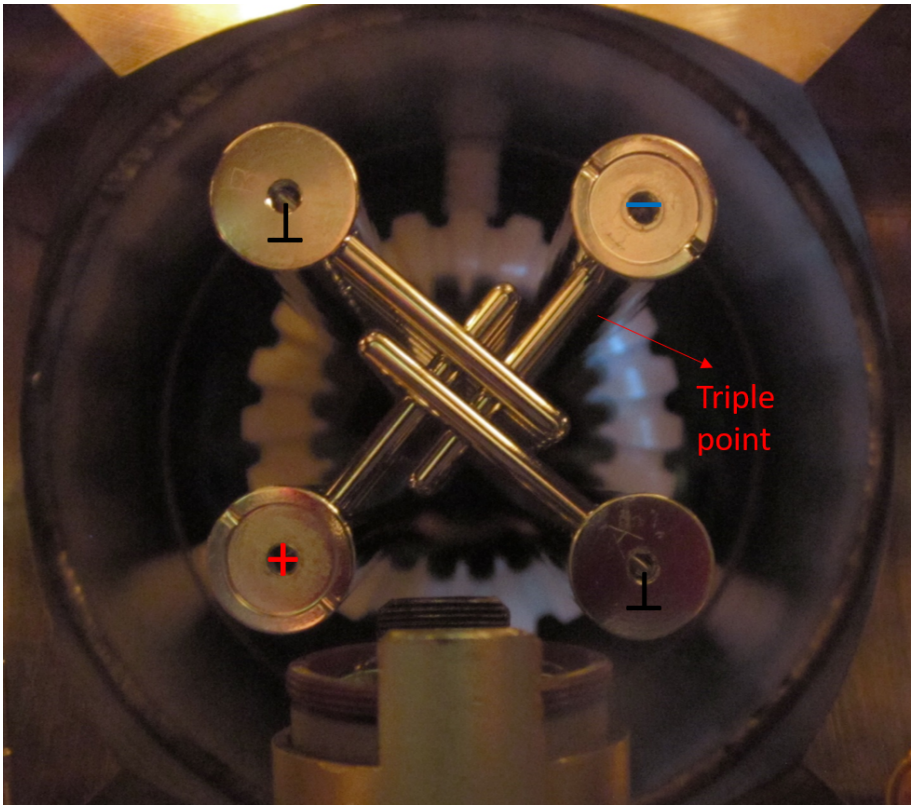

Figure 6.2: A picture of current surface flashover of an insulation mount made of Macor. The blue light is caused by the surface flashover. (+) means the electrode is connected to a positive polarity; (−) means the electrode is connected to a negative polarity; (⊥) means the electrode is grounded. Triple junction occurs where vacuum, metal and insulator meet with each other.

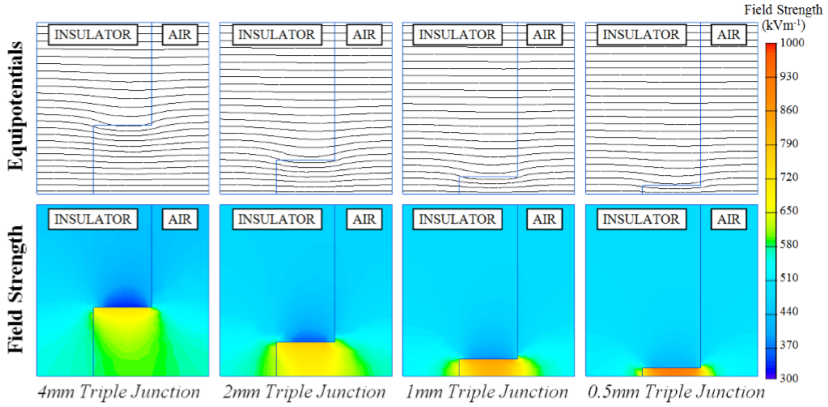

Figure 6.3: A simulated electric field distribution near a triple junction. The figure is taken from Ref.[84]

6.1.3 Aiming for a Larger Slowing Signal

At the same time of repairing the decelerator, we are also looking for a way to increase the number of slowing molecules. It is known lighter noble gas after supersonic expansion can experience less clustering and the supersonic cooling should be more efficient. Since only $3 \cdot 10^{-23}$ Joules energy can be removed at each stage of the decelerator ($\pm$ 12 kV), without cryogenically cooling the pulsed valve, the 140-stages second-generation decelerator can only load the molecules carried by krypton or even lighter noble gas into the magnetic trap. In order to use neon as a carrier gas (800 m/s velocity after supersonic expansion), we need a new decelerator with at least 300 stages.

With the goals of having a fully functioned decelerator and more slowing signal, we decide to build a third-generation stark decelerator.

6.2 Design and Construction of a Third-generation Stark Decelerator

6.2.1 General Information

The main idea of the third generation decelerator is identical with that of the second generation, which still relies on alternatively charging a pair of electrode pins to convert the kinetic energy into Stark energy and decelerate molecules. However, we do combine our new knowledge of high voltage insulation and redesign the insulation mount in order to avoid the surface flashover.

Fig. 6.4 shows the different views of the third-generation decelerator. There are 333 stages in total so that neon can be used as a carrier gas. Within each stage, the pin pair is separated by 2 mm. The nearby stage is separated by 5 mm from center to center. The total length of the decelerator is 1.7 m. In order to save the total weight for such a long setup, the main body frame is made of aluminum, which has been treated for vacuum.

All the parts being applied with high voltage are made of 316 stainless steel, including the clamps, decelerator rods and decelerator pins. One end of the decelerator pin is designed in a hemispherical shape to avoid surface arcing from any sharp edges. The other end has a tapered feature so that the pin can be directly inserted into the corresponding rod without the need of any

side screw. The idea of using tapered parts does save us lots of money and time during machining and installation. Before installation, all the surfaces of the electrodes have to be polished extremely carefully.

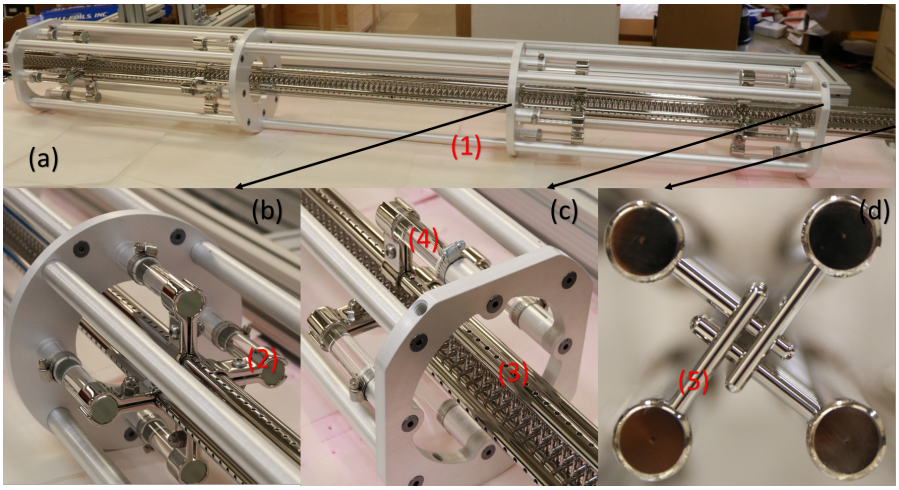

Figure 6.4: Different views of the third-generation stark decelerator. (1) The body frame made of aluminum. (2) The clamps made of 316 SS. (3) The decelerator rods made of 316 SS. (4) The high voltage insulator made of Pyrex glass. (5) The decelerator pins made of 316 stainless steel (SS).

6.2.2 Different Methods of Polishing

Since the decelerator pins experience the strongest electric field [6] during operation, they need especially careful treatment. Fig. 6.5 shows surface quality of decelerator pins under different ways of treatment. The first way we have tried is polishing the pins with 4000-grit sandpaper. By installing the pin into a plastic collet and onto a lathe, we are able to polish the pin with sandpaper at 1500 RPM. Compared with the non-treatment surface quality shown in Fig. 6.5(a), Fig. 6.5(c) confirms that several-minutes sanpaper polishing does produce a better-looking surface quality. The scratches left after grinding become lighter, but still visible. The surface quality can become even better with a longer time of polishing. However, this process is really time-consuming for 666 pieces.

[6] When ±12 kV is applied, the electric field strength is 120 kV/cm.

We have also tried polishing the pins by tumbling [7] . Fig. 6.5(d) shows the surface quality after several hours of tumbling. Compared with both Fig. 6.5(a) and (c), the scratches are almost completely removed and replaced by smaller size of dots, which is the signature of tumbling. It seems the tumbling can yield a much better surface quality than sandpaper does. Especially, about 50 pins can be tumbled at the same time so that the total time cost and labor work are reasonable.

The third way we have tried is called "eletro-polishing". The surface quality after three-minutes electro-polishing is shown in Fig. 6.5(b). The surface of the pin looks shiny and the overall quality is the closest to near-mirror-finish among all three methods. However, on the top of the mirror-finish surface, there are new holes appearing probably due to the fact that electrolyte used for electro-polishing can react with defects inside the stainless steel pin and corrode the materials away. In addition, since large amount of material can be removed during eletro-polishing, this method is not suitable for the tapered pins. Thus, we choose the tumbling as the procedure of polishing.

6.2.3 Insulator

We choose Pyrex as the high voltage insulator (shown in Fig. 6.4), since the Pyrex has a comparable dielectric strength as Macor and the surface can become much smoother. One end of the Pyrex bar is grabbed by the high voltage clamps and the other end is held inside a grounded holder. The distance between two ends is kept more than 5 cm, which reduces the electric field strength along the insulator surface below 3 kV/cm. To further reduce the field enhancement near the triple junction, we also recess the electrodes as suggested in Fig.20 of [84].

6.2.4 Gas Conditioning

No matter how good you can polish the surface of electrodes, there are always some field emission sites left which can cause the prebreakdown current during high voltage operation, such as sharp tips of the electrode, unintentional contamination, even the adsorbed gas inside the electrode.

[7] The tumbling is done by a local company named "Trigon".

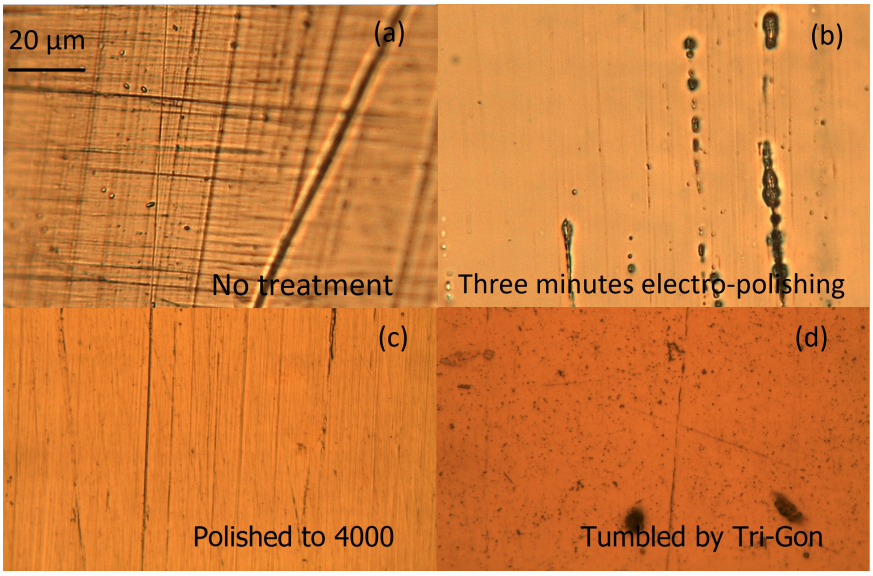

Figure 6.5: Surface quality of decelerator pins under different ways of polishing. Panel (a-d) share the identical scale. Each picture shown here is selected from a bunch of pictures taken at different locations of the same pin and roughly represents the averaged surface quality. All the pictures are taken under 50X microscope. (a) The surface quality of a decelerator pin after grinding without any extra treatment. There are three grinded pins ready for three other treatment. (b) The surface quality of a decelerator pin after three-minutes electro-polishing. (c) The surface quality of a decelerator pin after several-minutes 4000 grit sandpaper. (d) The surface quality of a decelerator pin after after several-hours tumbling.

In order to quench as many as possible of the sources of field emission, DC current conditioning is commonly utilized before operating the installed decelerator at full voltage. However, sometimes DC current conditioning behaves too aggressive and can damage the electrodes. Gas conditioning works as another way of eliminating the field emission. It relies on both ion implantation to improve the work function and electron bombarding to blunt sharp tips [85, 86].

In order to do the gas conditioning, first fill the chamber with 10^{-5} Torr of certain gas. Then, apply a small voltage to the electrodes. In order to protect the electrodes from avalanche arcing effects, a 100 MΩ resistor is placed in series with the electrodes. With 20 minutes of conditioning at each voltage and kV as an increasing step, finally run the power supply up to ±15 kV, which is 20% higher than the operation voltage of the decelerator.

The optimal species of gas used for conditioning really depends on the applied voltage, geometry of the electrodes and so on [87]. Thus, during the experiment we have tested several different gas and list their prebreakdown current at ± 15 kV applied voltage in Table 6.1.

Table 6.1: The prebreakdown current of different gas conditioning at ± 15 kV

Gas	prebreakdown current (μA)
No gas	50
He	27
N_2	8
O_2	2

The gas conditioning does help suppress the prebreakdown current, compared with DC current conditioning. Moreover, we find heavier gas such as O_2, works more efficiently for the voltage we are interested in. Our observation is also consistent with the results listed in Ref [87], which also gives an explanation: since the implantation depth of light gas (such as He) is very deep for a large applied voltage, then the concentration of ions at the surface of the electrode will become small and the ion implantation effect will also become weaker. Thus, we use O_2 to repeat the gas conditioning for several times.

After gas conditioning, we also pump away the gas and switch back to ± 15 kV DC current conditioning to check the post-current. There is a noticeable increasing of prebreakdown current

within minutes time-scale, which means the effects of gas conditioning can be reversed due to the depletion of implanted ions by large applied voltage. Empirically, we find if the voltage of DC current conditioning is kept 20% lower than the applied voltage for gas conditioning, the prebreakdown current can be maintained at a low level without a noticeable increasing within hours.

6.3 Characterization of the Stark Decelerator

With a well conditioned stark decelerator, the first thing to do is to fully optimize the coupling between a pulsed valve and time-varying deceleration sequence, which includes both transverse spatial coupling and longitudinal temporal coupling. DC guiding works as a procedure of optimizing transverse spatial coupling between the valve and decelerator and it is often used in our experiment.

6.3.1 A New Mode of DC Guiding

The DC guiding mode can be operated with the electrodes connected in a stationary configuration, such as the figures in the left column of Fig. 6.6. In the DC guiding mode, there will be no velocity variation in the Z-dimension, but only with a transverse confinement. Since OH moves much faster in the Z-dimension than the other two dimensions, it is reasonable to assume OH is confined inside a 2D trap, which is acquired by averaging the Stark energy along the Z-axis over one full period of the decelerator at each X-Y position. The $+-+-$ mode has been operated in our lab for the past years until recently a new mode called "$++--$" is discovered. The right column of Fig. 6.6 shows the effective 2D trap experienced by OH at different guiding modes. With the identical applied voltage, the $++--$ has almost factor two of the effective trap depth compared with $+-+-$ mode.

Fig. 6.7 shows the experimental measurement of OH time of flight (ToF) at two different guiding modes. Compared with $+-+-$ mode, $++--$ mode shows factor five more signal, which can improve the signal to noise dramatically so as to accelerate the decelerator optimization. Moreover, the new guiding mode can be used to study the intra-beam collision between neon and OH, which

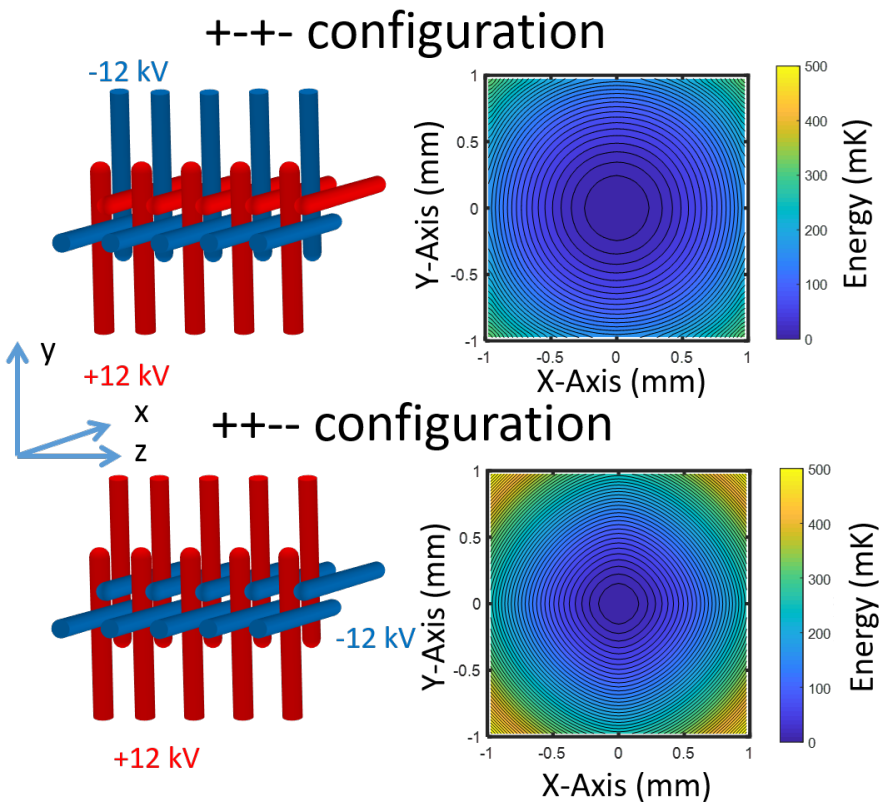

Figure 6.6: The comparisons between two different DC guiding modes. The left column shows the voltage configuration at different guiding modes. The right column shows the effective 2D trap experienced by OH in the X-Y plane. The effective 2D trap is acquired by averaging the Stark energy over one full period of the decelerator along Z-axis at each X-Y position. The energy contour is separated by 10 mK.

will be discussed in Chapter 7.

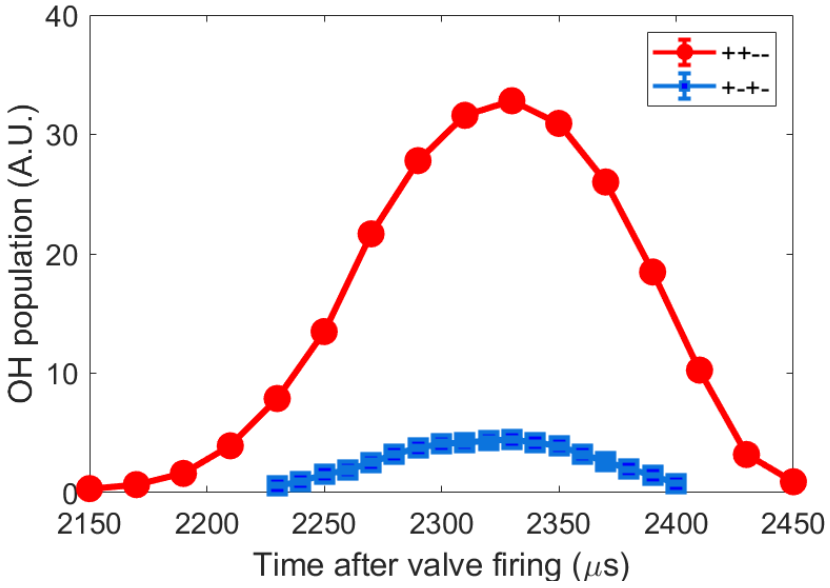

Figure 6.7: Experimental data of ToF at different guiding mode. The decelerator runs at ± 6 kV.The red circles represent the OH ToF signal at $++--$ guiding mode. The blue square represent the OH ToF signal at $+-+-$ guiding mode.

The conventional S=1 decelerator has disadvantages of low transverse trap depth and large parametric amplification [83]. In contrast, $++--$ guiding mode behaves much better for both problems. The advantages of new guiding mode trigger us to combine it into the conventional deceleration sequence and then figure out a new way of running the stark decelerator. The new sequence is able to improve the slowing signal by almost an order compared with S1 mode. Its slowing efficiency is even comparable to the efficiency of ultimate version of decelerator—traveling-wave decelerator. The details of the new sequence will be discussed in Dave Reens's thesis.

6.3.2 The OH ToF of an Optimized Stark Decelerator

Fig. 6.8 shows the OH ToF of an optimized stark decelerator for different final velocities. The good matching between a simulation and the experimental data suggests the high voltage system of the third-decelerator performs in an expected condition. With an identical photon collection

system as the one used for the second generation, it is demonstrated that the slowing signal has been completely recovered. With the long enough decelerator, we are also able to switch to different carrier gas and search the species dependent guiding efficiency. However, we find the number of guided molecules is independent of the species of carrier gas. Nevertheless, this decelerator can become a platform to pursuit the intra-beam collision between neon and OH, which will be discussed in the next chapter.

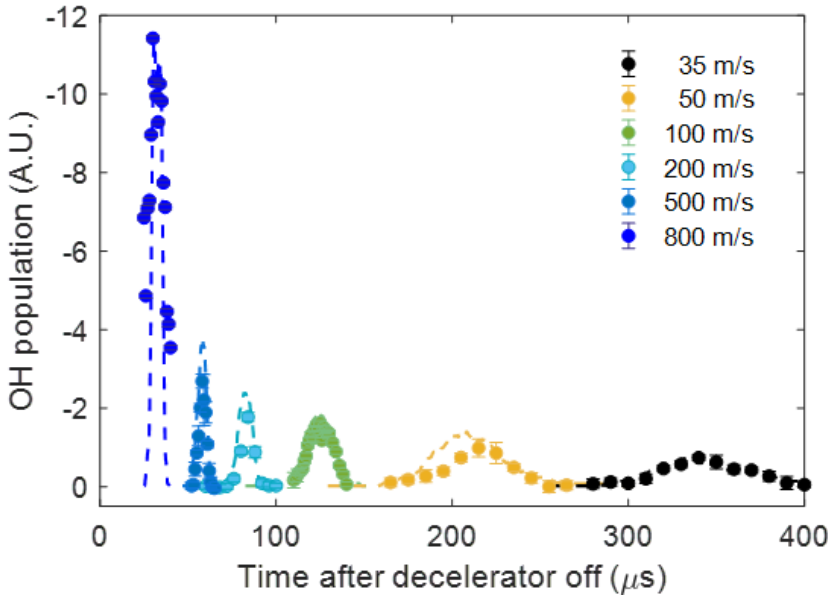

Figure 6.8: The OH ToF of an optimized stark decelerator for different final velocities. The dots represent the experimental data and the solid line represent the results from simulation.

Chapter 7

Cold Collisions between OH and Neon in an Intra-Beam

7.1 Motivation

It has been a dream for both physicists and chemists to use either radiation or static electromagnetic fields to realize quantum-controlled chemistry [14]. Since the maximal strength of static magnetic and electric fields (up to several Tesla and hundreds of kV/cm) can only shift the molecular levels by several Kelvin, in order to observe clear field-controlled effects, it is necessary to keep the collisional energy within Kelvin regime. Another benefit of sub-Kelvin-regime collision is that only a few number of partial waves get involved in the intermolecular interactions and the averaging effects from different reaction paths can be suppressed. In addition to a low collisional energy, it is also requisite to do quantum state preparation beforehand, since different states can follow different inelastic selection rule and form distinct products.

There have been many ways developed to do quantum state preparation, such as supersonic expansion, electrostatic quadrupole guides [88, 89], Stark-induced adiabatic Raman passage (SARP) [90], and so on. However, compared with state selection, it is much more challenging to keep the collisional energy below kelvin as well as maintaining high enough densities, since most of the slowing techniques are phase space density conservative [28, 30].

Until recently, several new ideas are implemented, which open the door of studying cold collisions to new perspectives. Instead of studying collisional effects after slowing or trapping [17], the cold collisions can also be pursued inside a single co-propagating beam. It is known that the supersonic expansion can provide a cold beam (the temperature of supersonic beam is around

Kelvin in the molecular frame), but also a large mean forward velocity in the lab frame, which limits the lowest achievable collisional energy in crossed beam scattering experiments [91]. The collisional energy can be varied by tuning the relative angle between two crossed beams. However, up to now the lowest collisional energy achieved in the crossed beam experiment is still above kelvin regime [92], which is limited by the finite spatial volumes of two crossed beam sources. To pass beyond this limit, it is suggested if one of the beam can be bended and merged with the other one in the same direction, by tuning the relative velocity between two beams close to zero, kelvin regime collisions become feasible [93–95]. Narevicius group [96] first demonstrates this idea. By using a curved magnetic quadrupole guide, two separate supersonic beams can be merged together and a penning ionization reaction down to 10 mK is observed between He* and H_2. Different from the merged beam experiment, which requires a complex apparatus, Zare group [97] is able to study the sub-kelvin stereodynamics interaction between HD and D_2 in a simpler way, by seeding two species into the coexpanded supersonic beam.

There have been not many electric field controlled collision experiments realized [98, 99] due to the strict requirement of a low collisional energy. Encouraged by the intra-beam collision experiment, we decide to study electric field controlled cold collisions between OH and neon. Neon is chosen for several reasons:

First, according to Ref. [70], a lighter noble gas can start with a smaller thermal energy in the molecular frame after supersonic expansion. Also, our measurements in Chapter 5 show the thermal temperatures of both neon and OH can be as low as 300 mK, which should be sufficient for the field controlled collision experiment.

Second, in principle, helium can offer even smaller thermal energy. However, the fluid velocity slip effect caused by the different masses between OH and helium can still induce a large collisional energy unless there is some acceleration applied to OH beam. The similar masses between OH and neon makes the fluid velocity slip effect much less significant.

Third, it is predicted by theorists that electric field can have a large impact on the inelastic cross section between OH and neon. Fig.7.1 shows inelastic cross section between OH upper

stretched state $|f, m_j = 3/2\rangle$ and neon at different applied electric field [100]. The inelastic cross section includes the contributions from all the possible final states—$|f, m_j = -3/2\rangle$, $|f, m_j = \pm 1/2\rangle$, $|e, m_j = \pm 1/2\rangle$ and $|e, m_j = \pm 3/2\rangle$. For each final state, a series of partial waves corresponding to the relevant collisional energy are also taken into account for both incoming and outgoing channels.

The inelastic cross section between OH and neon can be tuned by electric field in two mechanisms. First, due to the presence of electric field, opposite parity states can be coupled together and more partial waves can get involved in inelastic collisions [101]. The shape resonances can emerge once the collisional energy matches the energy levels of the quasi-bound states formed between short-range potential and centrifugal barrier of the partial waves, leading to a enhanced cross section, such as the cross section peak in either trace of Fig. 7.1, which is a sum of several shape resonance peaks. Second, in the collision experiment, tuning collisional energy can tweak the relative energetic difference between the incoming beam and the energy levels of quasi-bound states for the appearance of resonances. Electric field induced Stark shift can serve a similar purpose. As shown in Fig. 7.1, the blue and orange traces represent the cross section at collision energy 140 mK and 420 mK, respectively. From 140 mK to 420 mK, the collisional energy increases by 280 mK, which exactly matches the 10 kV/cm Stark shift energy from correspondent resonance peak displacement.

Fourth, the energy levels of quasi-bound states are very sensitive to the details of potential energy surface (PES) between OH and neon. Even the most advanced ab initio calculation can only guarantee 1% accuracy of PES, which corresponds to kelvin. The experimental data will be very valuable for the development of computational chemistry. All the points mentioned above make the electric field controlled cold collisions between OH and neon worth investigating.

7.2 Experimental Setup

In order to measure OH and neon intra-beam collisions, there are several technical issues which need be addressed in advance.

(1) How to generate electric field?

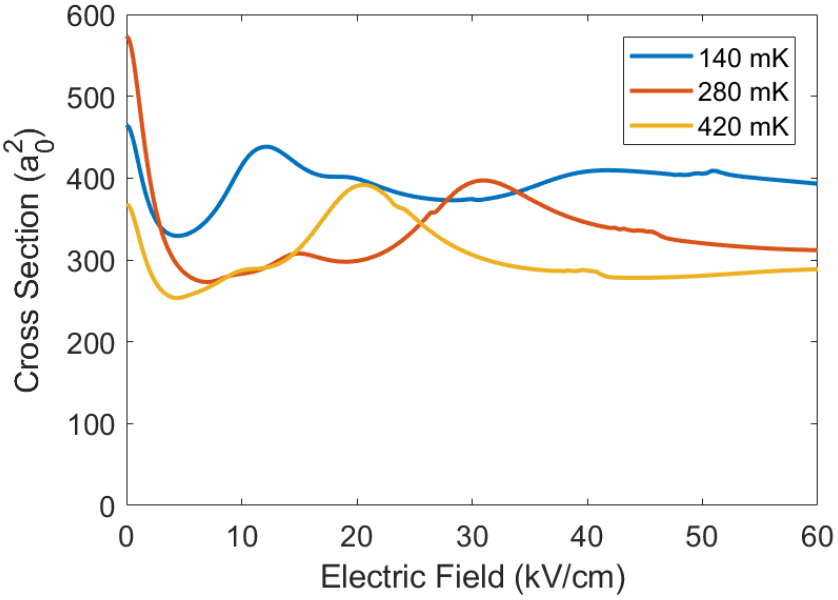

Figure 7.1: Inelastic cross section between $|f, m_j = 3/2\rangle$ state of OH and neon at different electric field strength. Different color represents different collisional energy.

The new-built stark decelerator introduced in Chapter 6 can be used to apply electric field and study cold collisions inside the molecular guide. Fig. 7.2 shows the electric field distribution experienced by OH along the decelerator when the decelerator operates at $++--$ configuration (± 1 kV). The distribution is calculated by running a Monte Carlo simulation and counting how much percentage of time spent on each electric field during propagation. There is a pronounced peak corresponding to the dominant electric field contribution, which is 5.5 kV/cm for $\pm$ 1 kV applied voltages. In order to calculate the averaged loss rate, we need weight all the electric field dependent loss rate based on its distribution.

(2) How to detect neon population?

There are two general ways of measuring atomic and molecular population– laser-based techniques and ion-based techniques. Since all the wavelengths related to optical transitions of ground state neon are near 100 nm, laser-based techniques are hard to be applied to neon measurement. Fast ion gauge works as a common ion-based tool and is used in our experiment to measure neon and characterize the cryogenic skimmer. However, since the gap between decelerator pins are too small to fit a fast ion gauge, the gauge has to be installed at the exit of the decelerator, where the neon density becomes too dilute to be measured by the fast ion gauge. Fortunately, a residual gas analyzer (SRS RGA300), which previously only served a purpose of measuring long-term background pressure, is demonstrated to be capable of measuring ToF of a short pulse. The RGA is composed of three components– a filament to do the ionization, a quadrupole mass spectrometer to do certain mass selection, an electron multiplier to amplify the signals. A transimpedance amplifier is used to bridge the Ion-counting-output port of RGA and a scope for signal readout [1] .

(3) How to tune the neon density?

[1] We are told by a SRS technician that the RGA is fast enough to measure μs wide pulse. We will calibrate the RGA with a fast ion gauge in the source chamber in future.

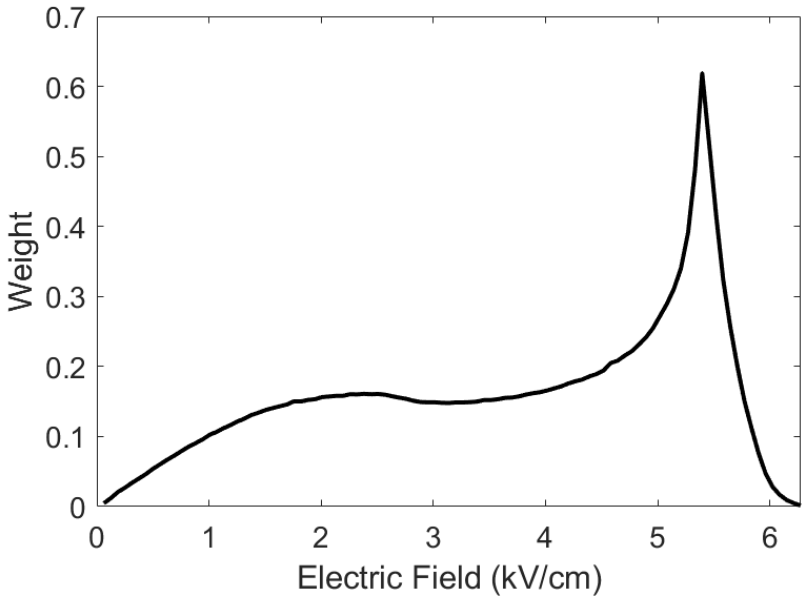

Figure 7.2: The electric field distribution experienced by OH along the decelerator when the decelerator operates in $++--$ configuration ($\pm$ 1 kV). The distribution is calculated by running a Monte Carlo simulation and counting how much percentage of time spent on each electric field during propagation. The total area underneath the curve is normalized to 1. There is a pronounced peak corresponding to the dominant electric field contribution, which is 5.5 kV/cm for $\pm$ 1 kV applied voltages.

There are many other loss mechanisms besides the collision-induced loss, such as the one-body loss due to imperfect DC guiding efficiency. In order to rule out the impact from such kind of loss, we need figure out a way to tune neon density and check density-dependent loss.

As introduced in Chapter 5, by driving the solenoid coils of the Even-Lavie valve with a pulsed current, the electromagnetic force can attract a magnetic plunger and release a pulsed beam. The valve is able to produce neon beams of different densities based on different amplitudes of driven current. However, it turns out to be almost impossible to only tune neon densities without affecting OH beam, since they are released from the same valve. Thus, we have to take some compromise between neon density detuning and relevant beam heating. Fig. 7.5(b) shows the neon ToF traces measured by RGA at different driven current. The density variation is maintained within factor two so that temperature increasing for both OH and neon are controlled within 20% of the original values. In addition to the beam heating, the OH initial population also depends on the valve operation, which makes the OH signal detected at the exit of decelerator not only rely on neon carrier density, but also depends on different valve operation. In order to overcome this problem, we can also measure the OH population at the entrance of the collisional region for OH signal normalization so that we are able to measure neon density dependent fractional loss.

(4) How to guarantee a good overlapping between OH and neon?

In order to have a good beam overlapping between OH and neon, first, we reduce the duration of RF discharging below 7 μs, which is much smaller than the initial beam width of neon (FWHM: 60 μs). Second, we seed OH to the peak of the neon carrier envelope by tuning the discharging delay as introduced in Chapter 5.

With all above problems addressed, we build up the experimental apparatus, as shown in Fig. 7.3, which includes two main technical improvements—cryogenic skimmer and $++--$ DC guiding in-

troduced in chapter 5 and 6, respectively. Compared with a commercial skimmer, the cryogenic skimmer can bring the valve 10 cm closer to the decelerator and provide higher neon density for collisions. ++−− DC guiding can provide much larger OH signal compared with +−+− configuration.

OH is still detected by laser induced fluorescence (LIF). There are two independent LIF collection systems installed at 40th and 333rd stage of the decelerator, respectively. The first 40 stages of decelerator are assigned to do state selection—removing populations from e-state and $|f, m_j = \pm 1/2\rangle$ state of OH as well as ionized and metastable species of neon. The stages from 40 to 333 are assigned as a collisional region. The RGA is installed at the exit of the decelerator for neon measurement.

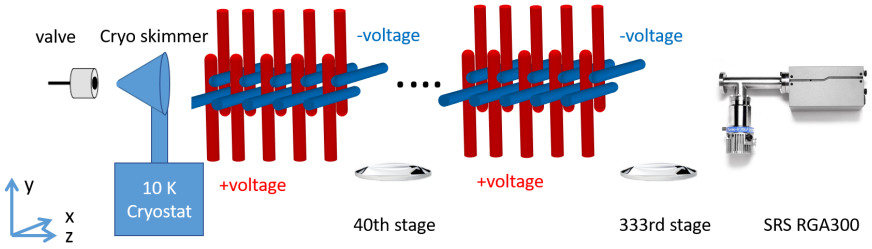

Figure 7.3: Experimental setup for OH-Neon intra-beam collisions. The stark decelerator operates at ++−− configuration as introduced in Chapter 6. There are two sets of LIF collection system installed at the 40th stage and 333rd stage of the decelerator, respectively. A RGA (SRS 300) is installed at the exit of the decelerator. The first 40 stages of the decelerator are used to do state preparation. The stages from 40 to 333 are used as a collisional region. A cryogenic skimmer is installed between the valve and the decelerator so as to increase the neon throughput for collisions.

7.3 Experimental Results and Analysis

7.3.1 Thermal Energy and Collisional Energy between OH and Ne

By accurately translating the valve to different skimmer-valve distances along the Z-axis, a series of OH ToF can be recorded by the LIF collection system installed at 40th stage of the decelerator. By fitting the ToF data with a Gaussian function, both the peak arrival time and

beam width can be acquired. The peak arrival times at different skimmer-valve distances are summarized in Fig. 7.4(a). The slope of the linear fit corresponds to the mean forward velocity, which is 803±1 m/s. In order to obtain the thermal energy of OH, it is necessary to measure the OH ToF far away from the valve so that the width of ToF can be attributed to velocity spread. The inset figure shows the OH ToF measured at 333rd stage with a 80 μs FWHM beam width. The velocity spread of OH can be calculated by formula $\sigma_v(OH) = v(OH)\sigma_t(OH)/t(OH)$, where $v(OH)$ is OH forward velocity (803 m/s); $\sigma_t(OH)$ is temporal spread of OH ToF beam (80 μs/2.3); $t(OH)$ is the peak arrival time of OH beam (2.61 ms). The measured velocity spread of OH equals to 10.7 m/s.

Fig. 7.4(b) shows the measurement of neon speed based on the same methods used for OH. However, the slope fitting shows much larger uncertainty compared with the fit slope realized in Fig. 7.4(a), which suggests that neon population experiences some nonlinear behavior against skimmer-valve distance. Instead of calculating the mean velocity from all the points, the velocity can also be calculated from nearby two points. The speed calculated from nearby two points are labeled in Fig. 7.4(b). A smaller skimmer-valve distance results in a lower calculated neon velocity, which can be explained by the appearance of skimmer clogging [2] . Our method of measuring velocity depends on the accuracy of peak arrival time. However, the presence of clogging can truncate away the falling edge of the beam and shift the effective peak earlier, which can lead to a "smaller" velocity. In order to suppress the skimmer clogging effect to the lowest level, we only use the two largest skimmer-valve distances in the plot to extract the neon speed, which shows 793 m/s. The result is consistent with the neon speed claimed by Even-Lavie valve [3] . The inset figure shows the ToF of neon measured at the largest skimmer-valve distance. The velocity spread of neon can be acquired with the same formula used for OH. The neon forward velocity is 793 m/s; The temporal spread of neon ToF is 147 μs/2.3; The neon peak arrival time is 3.1 ms. Thus, neon velocity spread $\sigma_v(Ne)$ equals to 16.3 m/s.

[2] We are using a commercial skimmer to do the velocity measurement.

[3] We can not move the valve even further to confirm the clogging has been completely removed, but we will revisit it in future with even larger translation capability.

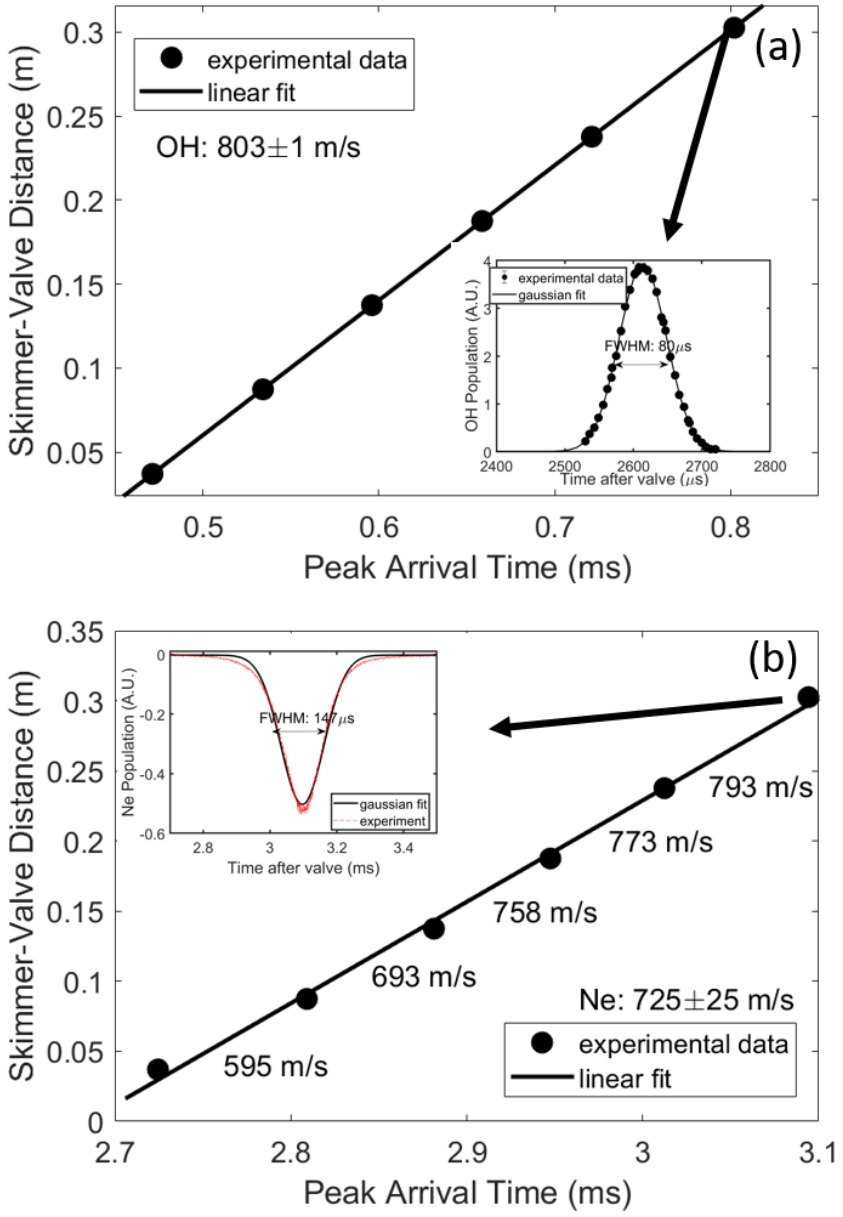

Figure 7.4: The measurement of mean velocity and velocity spread for both OH and neon. By accurately translating the valve to different skimmer-valve distances along the Z-axis, a series of ToF can be recorded so that both the peak arrival time and velocity spread can be extracted by fitting the ToF with a Gaussian function. (a)The measurement of OH. The linear fit shows the speed of OH is 803±1 m/s. The FWHM of the OH ToF at the exit of decelerator is 80 μs, corresponding to 10.7 m/s velocity spread. (b) The measurement of neon. Due to appearance of skimmer clogging, the global fit does not represent the authentic velocity. The neon velocities are also calculated by nearby two points and labeled in the plot. The FWHM of the neon ToF at the exit of decelerator is 147 μs, corresponding to 16.3 m/s velocity spread.

Even though we do not have any tools to measure the transverse velocities for both OH and neon, we can assign upper bounds for both species. For OH, since the $++--$ configuration offers a 2D trap, the maximal OH velocity should adapt to the trap depth. According to Fig.6.6, the maximal transverse OH velocity is 5 m/s when ± 2 kV are applied. For neon, since it does not experience any transverse confinement, the free expansion will make $v_{x,y}(Ne)$ smaller than 1.5 m/s at the entrance of the collisional region.

7.3.2 Collisional Energy between OH and Neon

As discussed in Ref. [102], the phase space rotation of a pulsed beam can cause geometric cooling and consequently improve the thermal resolution beyond the thermal energy limits. A narrower initial spatial distribution of the incident beam can cause a higher thermal resolution. According to Eq. (2.3) in Ref. [102], since the initial width of OH is only 7 μs, it can experience a significant geometric cooling. The velocity spread ($\sigma_v(OH)$) decreases from the measured value 10.7 m/s to 4.4 m/s in the Z-dimension. In contrast, neon hardly experiences any cooling due to its significant initial width of neon (60 μs).

The thermal resolution between OH and neon can be expressed as [102]:

$$\Delta E = \frac{m}{2}\sqrt{\sum_{i=x,y,z}[4(v_i(OH)-v_i(Ne))^2(\sigma_{v,i}^2(OH)+\sigma_{v,i}^2(Ne))+2(\sigma_{v,i}^2(OH)+\sigma_{v,i}^2(Ne))^2]} \tag{7.1}$$

, where m is the reduced mass between neon and OH; $v_i(OH)$ and $v_i(Ne)$ are the mean velocities of OH and neon in each dimension, respectively; $\sigma_{v,i}(OH)$ and $\sigma_{v,i}(Ne)$ are the velocity spreads of OH and neon in each dimension, respectively.

The collisional energy between OH and neon can be expressed as [102]:

$$\langle E\rangle = \frac{m}{2}\sum_{i=x,y,z}[(v_i(OH)-v_i(Ne))^2+\sigma_{v,i}^2(OH)+\sigma_{v,i}^2(Ne)] \tag{7.2}$$

Substituting all the parameters deduced above into Eq. 7.1 and Eq. 7.2, we obtain 240 mK of collisional energy and 300 mK of thermal energy. Both of these values are low enough to observe electric field controlled colllision. Table 7.1 summarizes all the energy related parameters.

Table 7.1: The Summary of OH and Neon speed.

	OH	Ne
Longitudinal speed	803 m/s	793 m/s
Transverse speed	5 m/s@±2 kV	1.5 m/s
Longitudinal velocity spread	10.7 m/s	16.3 m/s
Longitudinal velocity spread with geometric cooling	4.4 m/s	16.0 m/s
Transverse velocity spread	5 m/s@±2 kV	1.5 m/s
Collisional energy	240 mK	
Thermal energy	300 mK	

7.3.3 Electric Field Dependent Loss Rate

Fig. 7.5 demonstrates the choice of data and its corresponding data analysis for the extraction of the loss rate of OH and neon collision. OH ToF measured at 40th and 333rd stages of the decelerator are shown in Fig. 7.5(a). The decelerator operates at ± 6 kV and the density of neon is set to maximum. OH population at each stage can be acquired by fitting the ToF with a Gaussian function and integrating the area underneath the fitting curve.

Fig. 7.5(b) shows neon ToF measured at various valve driven current, corresponding to different neon densities. Given that spatial widths of neon packets are almost the same at different valve conditions, neon density scales proportionally with neon population calculated by integrating the area underneath the packets.

Fig. 7.5(c), which shows the relation between normalized OH signal and neon density. The normalized OH signal is calculated by dividing the total OH population measured at 333rd stage by the total OH population measured at 40th stage. By fitting the experimental data with exponential function $Ae^{-\beta n_{Ne}}$, the loss rate β can be extracted, which excludes other density independent losses, e.g. one body dynamic loss from DC guiding.

Fig. 7.6 shows a summary of OH loss rate at different applied voltages. It is noted that the data acquisition takes about three months. It is desirable to improve the efficiency in future. It is extremely difficult to measure the loss rate below ± 1 kV due to the poor signal to noise ratio. The black dots represent the experimental data taken with a cryogenic skimmer, which

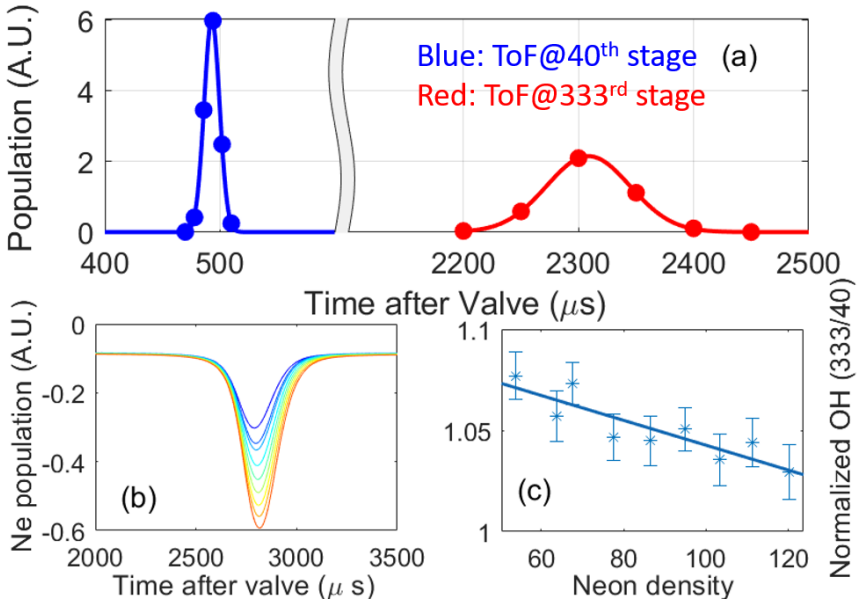

Figure 7.5: The summary of data analysis procedure at ± 6 kV. (a) OH ToF measured at 40th and 333rd stage of the decelerator with certain neon density. The dots represent experimental data. The solid line represent a Gaussian fit. The OH population is calculated by integrating the area underneath the fit. (b) Neon ToF at different valve conditions, corresponding to different neon densities. (c) The relation between normalized OH population and neon density. The normalized OH signal is calculated by dividing the total OH population measured at 333rd stage with the total OH population measured at 40th stage [103]. The data can be fitted by exponential function: $Ae^{-\beta n_{Ne}}$, of which β is the loss rate.

shows a clear enhanced loss peak at ± 2 kV. In order to check whether the peak is caused by any systematic effects, we switch back to a commercial skimmer and repeat the data acquisition with same experimental parameters. The only difference between these two setups is that the valve is placed 10 cm further away from the decelerator to avoid skimmer clogging for the commercial skimmer. The data taken with a commercial skimmer is represented by red square. It can be seen that there is no electric field dependency, even though the neon density dependent loss still exists.

7.4 Puzzles and Outlook

We are still trying to understand the experimental discrepancies between two different skimmers. Here, I list out some of the speculations that we have come out related to the puzzles.

First, as is clear from our measurements, the collisional/thermal energy under two different skimmers are nearly identical in the Z-dimension. Due to the fact that we do not have a good way of measuring the transverse temperature of OH and neon, there is a chance that the transverse temperature under two different skimmers are completely different. However, our previous estimations of the transverse temperature of both OH and neon already set a upper bound, which is much smaller compared with the thermal and collisional energy in the Z-axis. Thus, we believe the different values of energy is not a possible explanation for the discrepancies.

Second, we suspect the LIF collection system at 40th stage may undercount the OH population, since both the imperfect alignment of the LIF collection system and a small solid angle due to the narrow decelerator-pin spacing make it possible that the collection system has a very "'small" field of view and is only sensitive to a portion of the OH packet in the transverse dimension. As mentioned before, different skimmer choices correspond to different skimmer-valve distances, which can lead to different OH oscillating phases in the transverse dimension at 40th stage [4] and cause OH to appear at different transverse positions.

In order to check this "conspiracy theory", we can try to deliberately misalign the LIF collection system at 40th stage and repeat the loss rate measurement with the cryogenic skimmer.

[4] The details related to oscillation will be discussed in Dave Reens' thesis

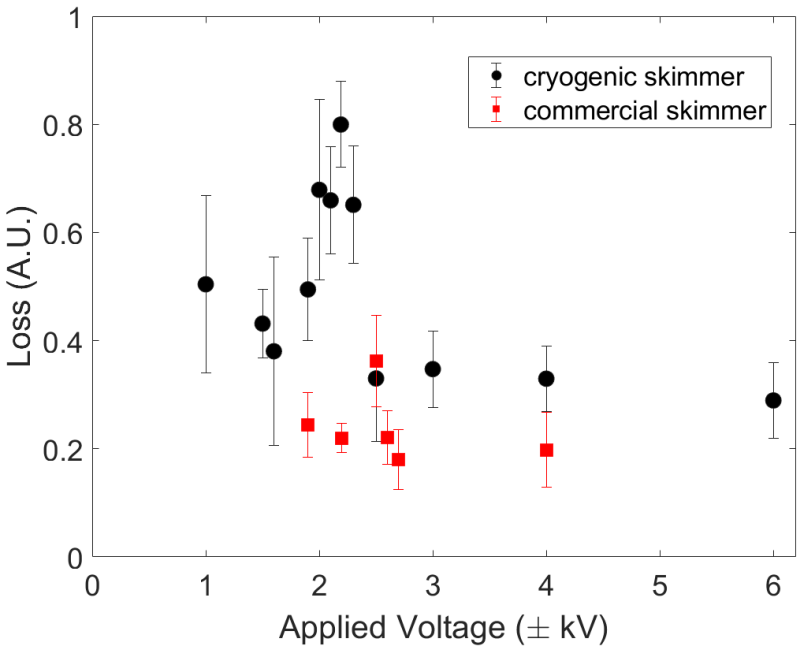

Figure 7.6: Summary of OH loss rate at different applied voltage. The black circle represents the data is taken with a cryogenic skimmer. The red square represents the data taken with a commercial skimmer.

If the field of view of the collection system does not have transverse position dependence, the potential loss rate should be remain the same.

Third, if the collection system does not undercount the OH signal, it indicates the discrepancies are possibly due to some sensitive parameters related to collisions. Besides the collisional energy, the purities of the states can also affect the inelastic scattering. The first 40 stages are assigned to remove both e-states and $|f, m_j = \pm 1/2\rangle$ prior to the collisional region. However, we are not able to confirm the state purities after 40 stages. If OH travels exactly along the centerline of the decelerator without any transverse velocity, even high-field-seeking states can not be removed since they will not experience any transverse force. In general, it is harder to remove the molecules with a smaller transverse velocity. For the commercial skimmer, OH beam enters the decelerator with a smaller transverse velocity compared with the beam entering the cryogenic skimmer as the valve is installed much further away from the decelerator. It is possible that the state depletion is much less efficient and the inelastic scattering is suppressed, which is consistent with our observation.

In order to confirm this speculation, we can measure and compare the e-state population at 40th stage under two different skimmers. We can also measure the OH loss rate under the cryogenic skimmer but with the largest skimmer-valve distance to check whether the loss rate depends on the skimmer-valve distance.

If the systematic between different skimmers can be figured out, the intra-beam collisions inside a decelerator can become a promising way to search for field control dipolar interactions, such as OH and CO, OH and NH_3, and so on.

Bibliography

[1] L. D. Carr, D. DeMille, R. V. Krems, and J. Ye, New Journal of Physics **11**, 055049 (2009).

[2] B. C. Regan, E. D. Commins, C. J. Schmidt, and D. DeMille, Phys. Rev. Lett. **88**, 071805 (2002).

[3] T. E. Chupp, P. Fierlinger, M. J. Ramsey-Musolf, and J. T. Singh, Rev. Mod. Phys. **91**, 015001 (2019).

[4] W. D. Phillips, Rev. Mod. Phys. **70**, 721 (1998).

[5] M. R. Tarbutt, Contemporary Physics **0**, 1 (2019).

[6] C. Chin, R. Grimm, P. Julienne, and E. Tiesinga, Rev. Mod. Phys. **82**, 1225 (2010).

[7] M. A. Baranov, M. Dalmonte, G. Pupillo, and P. Zoller, Chemical Reviews **112**, 5012 (2012).

[8] J. J. Hudson, D. M. Kara, I. J. Smallman, B. E. Sauer, M. R. Tarbutt, and E. A. Hinds, Nature **473**, 493 (2011).

[9] V. Andreev, D. G. Ang, D. DeMille, J. M. Doyle, G. Gabrielse, J. Haefner, N. R. Hutzler, Z. Lasner, C. Meisenhelder, B. R. O'Leary, C. D. Panda, A. D. West, E. P. West, X. Wu, and A. C. M. E. Collaboration, Nature **562**, 355 (2018).

[10] W. B. Cairncross, D. N. Gresh, M. Grau, K. C. Cossel, T. S. Roussy, Y. Ni, Y. Zhou, J. Ye, and E. A. Cornell, Phys. Rev. Lett. **119**, 153001 (2017).

[11] H. Loh, K. C. Cossel, M. C. Grau, K.-K. Ni, E. R. Meyer, J. L. Bohn, J. Ye, and E. A. Cornell, Science **342**, 1220 (2013).

[12] P. Jansen, H. L. Bethlem, and W. Ubachs, The Journal of Chemical Physics **140**, 010901 (2014).

[13] V. V. Flambaum and M. G. Kozlov, Phys. Rev. Lett. **99**, 150801 (2007).

[14] R. V. Krems, Physical Chemistry Chemical Physics **10**, 4079 (2008).

[15] G. Quéméner and P. S. Julienne, Chemical Reviews **112**, 4949 (2012).

[16] E. Herbst and J. T. Yates, Chemical Reviews **113**, 8707 (2013).

[17] B. C. Sawyer, B. K. Stuhl, M. Yeo, T. V. Tscherbul, M. T. Hummon, Y. Xia, K. Jacek, D. Patterson, J. M. Doyle, and J. Ye, Physical Chemistry Chemical Physics **13**, 19059 (2011).

[18] X. Wu, T. Gantner, M. Koller, M. Zeppenfeld, S. Chervenkov, and G. Rempe, Science **358**, 645 (2017).

[19] H. P. Büchler, E. Demler, M. Lukin, A. Micheli, N. Prokof'ev, G. Pupillo, and P. Zoller, Phys. Rev. Lett. **98**, 060404 (2007).

[20] N. Y. Yao, A. V. Gorshkov, C. R. Laumann, A. M. Läuchli, J. Ye, and M. D. Lukin, Phys. Rev. Lett. **110**, 185302 (2013).

[21] E. R. Hudson and W. C. Campbell, Phys. Rev. A **98**, 040302 (2018).

[22] J. W. Park, Z. Z. Yan, H. Loh, S. A. Will, and M. W. Zwierlein, Science **357**, 372 (2017).

[23] N. R. Hutzler, H.-I. Lu, and J. M. Doyle, Chemical Reviews **112**, 4803 (2012).

[24] J. F. Barry, D. J. McCarron, E. B. Norrgard, M. H. Steinecker, and D. DeMille, Nature **512**, 286 (2014).

[25] A. L. Collopy, S. Ding, Y. Wu, I. A. Finneran, L. Anderegg, B. L. Augenbraun, J. M. Doyle, and J. Ye, Phys. Rev. Lett. **121**, 213201 (2018).

[26] S. Truppe, H. J. Williams, M. Hambach, L. Caldwell, N. J. Fitch, E. A. Hinds, B. E. Sauer, and M. R. Tarbutt, Nature Physics **13**, 1173 (2017).

[27] S. Chervenkov, X. Wu, J. Bayerl, A. Rohlfes, T. Gantner, M. Zeppenfeld, and G. Rempe, Phys. Rev. Lett. **112**, 013001 (2014).

[28] S. Y. T. van de Meerakker, H. L. Bethlem, N. Vanhaecke, and G. Meijer, Chemical Reviews **112**, 4828 (2012).

[29] J. R. Bochinski, E. R. Hudson, H. J. Lewandowski, G. Meijer, and J. Ye, Phys. Rev. Lett. **91**, 243001 (2003).

[30] E. Narevicius and M. G. Raizen, Chemical Reviews **112**, 4879 (2012).

[31] S. D. Hogan, M. Motsch, and F. Merkt, Physical Chemistry Chemical Physics **13**, 18705 (2011).

[32] M. Kirste, X. Wang, H. C. Schewe, G. Meijer, K. Liu, A. van der Avoird, L. M. C. Janssen, K. B. Gubbels, G. C. Groenenboom, and S. Y. T. van de Meerakker, Science **338**, 1060 (2012).

[33] E. S. Shuman, J. F. Barry, and D. DeMille, Nature **467**, 820 (2010).

[34] M. T. Hummon, M. Yeo, B. K. Stuhl, A. L. Collopy, Y. Xia, and J. Ye, Phys. Rev. Lett. **110**, 143001 (2013).

[35] J. F. Barry, E. S. Shuman, E. B. Norrgard, and D. DeMille, Phys. Rev. Lett. **108**, 103002 (2012).

[36] V. Zhelyazkova, A. Cournol, T. E. Wall, A. Matsushima, J. J. Hudson, E. A. Hinds, M. R. Tarbutt, and B. E. Sauer, Phys. Rev. A **89**, 053416 (2014).

[37] M. Yeo, M. T. Hummon, A. L. Collopy, B. Yan, B. Hemmerling, E. Chae, J. M. Doyle, and J. Ye, Phys. Rev. Lett. **114**, 223003 (2015).

[38] L. W. Cheuk, L. Anderegg, B. L. Augenbraun, Y. Bao, S. Burchesky, W. Ketterle, and J. M. Doyle, Phys. Rev. Lett. **121**, 083201 (2018).

[39] L. Caldwell, J. A. Devlin, H. J. Williams, N. J. Fitch, E. A. Hinds, B. E. Sauer, and M. R. Tarbutt, arXiv:1812.07926 (2018).

[40] L. Anderegg, L. W. Cheuk, Y. Bao, S. Burchesky, W. Ketterle, K.-k. Ni, and J. M. Doyle, arXiv:1902.00497 (2019).

[41] L. De Marco, G. Valtolina, K. Matsuda, W. G. Tobias, J. P. Covey, and J. Ye, Science **363**, 853 (2019).

[42] P. K. Molony, P. D. Gregory, Z. Ji, B. Lu, M. P. Köppinger, C. R. Le Sueur, C. L. Blackley, J. M. Hutson, and S. L. Cornish, Phys. Rev. Lett. **113**, 255301 (2014).

[43] C.-H. Wu, J. W. Park, P. Ahmadi, S. Will, and M. W. Zwierlein, Phys. Rev. Lett. **109**, 085301 (2012).

[44] T. M. Rvachov, H. Son, A. T. Sommer, S. Ebadi, J. J. Park, M. W. Zwierlein, W. Ketterle, and A. O. Jamison, Phys. Rev. Lett. **119**, 143001 (2017).

[45] M. Guo, B. Zhu, B. Lu, X. Ye, F. Wang, R. Vexiau, N. Bouloufa-Maafa, G. Quéméner, O. Dulieu, and D. Wang, Phys. Rev. Lett. **116**, 205303 (2016).

[46] L. R. Liu, J. D. Hood, Y. Yu, J. T. Zhang, N. R. Hutzler, T. Rosenband, and K.-K. Ni, Science **360**, 900 (2018).

[47] M. S. Safronova, D. Budker, D. DeMille, D. F. J. Kimball, A. Derevianko, and C. W. Clark, Rev. Mod. Phys. **90**, 025008 (2018).

[48] J. Brown and A. Carrington, Rotational Spectroscopy of Diatomic Molecules, Cambridge Molecular Science (Cambridge University Press, 2003).

[49] B. K. Stuhl, M. T. Hummon, M. Yeo, G. Quéméner, J. L. Bohn, and J. Ye, Nature **492**, 396 (2012).

[50] H. E. Radford, Phys. Rev. **122**, 114 (1961).

[51] K. Maeda, M. L. Wall, and L. D. Carr, New Journal of Physics **17**, 045014 (2015).

[52] D. Reens, H. Wu, T. Langen, and J. Ye, Physical Review A **96**, 063420 (2017).

[53] J. Luque and D. R. Crosley, LIFbase: Database and Spectral Simulation (1999).

[54] B. K. Stuhl, M. Yeo, B. C. Sawyer, M. T. Hummon, and J. Ye, Phys. Rev. A **85**, 033427 (2012).

[55] M. Yeo, The Laser Cooling and Magneto-Optical Trapping of the YO Molecule, Ph.D. thesis, University of Colorado at Boulder (2015).

[56] W. Petrich, M. H. Anderson, J. R. Ensher, and E. A. Cornell, Phys. Rev. Lett. **74**, 3352 (1995).

[57] B. Sawyer, Cold polar molecules for novel collision experiments at low energies, Ph.D. thesis, University of Colorado at Boulder (2010).

[58] B. K. Stuhl, M. Yeo, M. T. Hummon, and J. Ye, Molecular Physics **111**, 1798 (2013).

[59] J. L. Bohn and G. Quéméner, Molecular Physics **111**, 1931 (2013).

[60] G. Bird, The DSMC Method (CreateSpace Independent Publishing Platform, 2013).

[61] G. Quéméner and J. L. Bohn, Phys. Rev. A **93**, 012704 (2016).

[62] L. Anderegg, B. L. Augenbraun, Y. Bao, S. Burchesky, L. W. Cheuk, W. Ketterle, and J. M. Doyle, Nature Physics **14**, 890 (2018).

[63] T. Esslinger, I. Bloch, and T. W. Hänsch, Physical Review A **58**, R2664 (1998).

[64] H. J. Williams, L. Caldwell, N. J. Fitch, S. Truppe, J. Rodewald, E. A. Hinds, B. E. Sauer, and M. R. Tarbutt, Phys. Rev. Lett. **120**, 163201 (2018).

[65] J. M. Beames, F. Liu, M. I. Lester, and C. Murray, The Journal of Chemical Physics **134**, 241102 (2011).

[66] J. M. Gray, J. A. Bossert, Y. Shyur, and H. J. Lewandowski, Phys. Rev. A **96**, 023416 (2017).

[67] W. K. Bischel, D. J. Bamford, and L. E. Jusinski, Appl. Opt. **25**, 1215 (1986).

[68] T. M. James, M. Schlösser, S. Fischer, M. Sturm, B. Bornschein, R. J. Lewis, and H. H. Telle, Journal of Raman Spectroscopy **44**, 857 (2013).

[69] S. N. Vogels, Z. Gao, and S. Y. van de Meerakker, EPJ Techniques and Instrumentation **2**, 12 (2015).

[70] U. Even, Advances in Chemistry **2014**, 636042 (2014).

[71] L. Ploenes, D. Haas, D. Zhang, S. Y. T. van de Meerakker, and S. Willitsch, Review of Scientific Instruments **87**, 053305 (2016).

[72] D. Irimia, D. Dobrikov, R. Kortekaas, H. Voet, D. A. van den Ende, W. A. Groen, and M. H. M. Janssen, Review of Scientific Instruments **80**, 113303 (2009).

[73] H. Beijerinck and N. Verster, Physica B+C **111**, 327 (1981).

[74] R. Campargue, The Journal of Physical Chemistry **88**, 4466 (1984).

[75] U. Bossel, Entropie **42**, 12 (1971).

[76] R. Subramanian and M. Sulkes, Review of Scientific Instruments **79**, 016101 (2008).

[77] Y. Segev, N. Bibelnik, N. Akerman, Y. Shagam, A. Luski, M. Karpov, J. Narevicius, and E. Narevicius, Science Advances **3** (2017).

[78] N. L. Uzi Even, Type E-L-5-2015-HRR operating manual (2015).

[79] J. W. Ekin, Experimental Techniques for Low-Temperature Measurements (Oxford Univ. Press, Oxford, 2006).

[80] J. Ju and B. Cros, Journal of Applied Physics **112**, 113102 (2012).

[81] C. Day, Basics and Applications of Cryopumps, CERN Accelerator School Proceedings on Vacuum in Accelerators (CERN Accelerator School Proceedings on Vacuum in Accelerators, 2006).

[82] M. M. Menon, G. J. Laughon, R. Maingi, M. R. Wade, D. L. Hillis, and M. A. Mahdavi, Journal of Vacuum Science Technology A: Vacuum, Surfaces, and Films **13**, 551 (1995).

[83] E. Hudson, Experiments on Cold Molecules Produced via Stark Deceleration, Ph.D. thesis, University of Colorado at Boulder (2006).

[84] D. Faircloth, Technological Aspects: High Voltage (2014) pp. 381–419.

[85] S. Bajic and R. V. Latham, Journal of Physics D: Applied Physics **21**, 943 (1988).

[86] M. BastaniNejad, A. Elmustafa, E. Forman, J. Clark, S. Covert, J. Grames, J. Hansknecht, C. Hernandez-Garcia, M. Poelker, and R. Suleiman, Nuclear Instruments and Methods in Physics Research Section A: Accelerators, Spectrometers, Detectors and Associated Equipment **762**, 135 (2014).

[87] R. V. Latham, ed., High voltage vacuum insulation:Basic concepts and technological practice (1995).

[88] T. Rieger, T. Junglen, S. A. Rangwala, G. Rempe, P. W. H. Pinkse, and J. Bulthuis, Phys. Rev. A **73**, 061402 (2006).

[89] T. Junglen, T. Rieger, S. A. Rangwala, P. W. H. Pinkse, and G. Rempe, The European Physical Journal D - Atomic, Molecular, Optical and Plasma Physics **31**, 365 (2004).

[90] N. Mukherjee and R. N. Zare, The Journal of Chemical Physics **135**, 024201 (2011).

[91] L. Scharfenberg, S. Y. T. van de Meerakker, and G. Meijer, Phys. Chem. Chem. Phys. **13**, 8448 (2011).

[92] C. Berteloite, M. Lara, A. Bergeat, S. D. Le Picard, F. Dayou, K. M. Hickson, A. Canosa, C. Naulin, J.-M. Launay, I. R. Sims, and M. Costes, Phys. Rev. Lett. **105**, 203201 (2010).

[93] S. Y. T. van de Meerakker and G. Meijer, Faraday Discuss. **142**, 113 (2009).

[94] M. Gupta and D. Herschbach, The Journal of Physical Chemistry A **105**, 1626 (2001).

[95] Q. Wei, I. Lyuksyutov, and D. Herschbach, The Journal of Chemical Physics **137**, 054202 (2012).

[96] A. B. Henson, S. Gersten, Y. Shagam, J. Narevicius, and E. Narevicius, Science **338**, 234 (2012).

[97] W. E. Perreault, N. Mukherjee, and R. N. Zare, Science **358**, 356 (2017).

[98] K.-K. Ni, S. Ospelkaus, D. Wang, G. Quéméner, B. Neyenhuis, M. H. G. de Miranda, J. L. Bohn, J. Ye, and D. S. Jin, Nature **464**, 1324 (2010).

[99] L. P. Parazzoli, N. J. Fitch, P. S. Żuchowski, J. M. Hutson, and H. J. Lewandowski, Phys. Rev. Lett. **106**, 193201 (2011).

[100] T. V. Tscherbul, Personal communication.

[101] Z. Pavlovic, T. V. Tscherbul, H. R. Sadeghpour, G. C. Groenenboom, and A. Dalgarno, The Journal of Physical Chemistry A **113**, 14670 (2009).

[102] Y. Shagam and E. Narevicius, The Journal of Physical Chemistry C **117**, 22454 (2013).

[103] The ratio is larger than one is due to the fact that the LIF collection efficiency at the 333rd is higher than that of 40th stage.